Fabrication of submicrometer 3D structures by one-photon absorption direct laser writing and applications

Mai Trang Do

Fabrication of submicrometer 3D structures by one-photon absorption direct laser writing and applications

A dissertation presented

by

Mai Trang Do

to

Laroratoire de Photonique Quantique et Moléculaire

in partial fulfillment of the requirements for the degree of

Doctor of Philosophy

in the subject of

Physics

Examining committee :

M.	BECHE Bruno	Univ. de Rennes 1	Reviewer
Mme.	MARRIS-MORINI Delphine	Univ. de Paris-Sud	Reviewer
M.	GIRARD Sylvain	Univ. de Cean	Examinator
M.	BRASSELET Etienne	Univ. de Bordeaux	Examinator
Mme.	LEDOUX-RAK Isabelle	ENS de Cachan	Examinator
M.	LAI Ngoc Diep	ENS de Cachan	Supervisor

ECOLE NORMALE SUPERIEURE DE CACHAN

19 January 2015

Abstract

This work deals with a novel microscopy technique based on the ultra-low one-photon absorption (LOPA) mechanism of photosensitive materials for fabrication of arbitrary two- and three-dimensional (2D, 3D) submicrometer structures.

First, we theoretically investigated the intensity distribution at focusing region of a high numerical aperture objective lens as a function of various working conditions, such as propagation of light through mismatched refractive index and/or absorbing media. We demonstrated that when working with refractive index mismatch-free and very low absorption conditions, the light could be focused deeply inside the material, allowing a 3D optical manipulation.

We then demonstrated experimentally the use of this simple technique for fabrication of desired structures. Different 2D and 3D structures, with a feature size as small as 150 nm, have been created in SU-8 photoresist by using a low power and continuous-wave laser emitting at 532 nm. Furthermore, we demonstrated that it is possible to fabricate a polymer-based photonic structure containing a single nanoparticle, by using a double-step method. Indeed, the LOPA microscopy allowed us first to accurately determine the location of a single gold nanoparticle and then to embed it as desired into an arbitrary SU-8 photonic structure. The coupling of a gold NP and a polymer-based photonic structure was theoretically and experimentally investigated showing a six-fold photons collection enhancement as compared to that of a NP in unpatterned film.

Résumé

Ce travail porte sur l'étude d'une nouvelle technique de microscopie basée sur le phénomène d'absorption linéaire ultra-faible (LOPA) de matériaux photosensibles pour la fabrication des structures submicrométriques à deux et à trois dimensions (2D, 3D). Premièrement, nous avons étudié théoriquement la distribution de l'intensité lumineuse dans la région focale d'un objectif de microscope de grande ouverture numérique en fonction des différentes conditions de travail, telles que la propagation de la lumière dans un milieu absorbant avec une variation d'indice de refraction. Nous avons démontré que lorsque l'on travaille avec un matériau quasi homogène ayant de très faible absorption à la longueur d'onde du faisceau d'excitation, le faisceau laser peut être focalisé en profondeur à l'intérieur du matériau, ce qui permet de manipuler optiquement des objets en 3D. Nous avons ensuite démontré expérimentalement l'utilisation de cette technique pour fabriquer des structures désirées. Différentes structures 2D et 3D submicrométriques ont été crées en résine SU-8, en utilisant un laser continue à 532 nm de faible puissance. Ces résultats sont similaires à ceux obtenus par la méthode d'absorption à deux photons, mais le coût de fabrication a été énormément réduit. De plus, nous avons démontré qu'il est possible de fabriquer des structures photoniques à base de polymère contenant une seule nanoparticule (NP), en utilisant un procédé à deux étapes. En effet, nous avons d'abord déterminé avec précision la position d'une seule NP d'or, en utilisant une puissance d'excitation très faible, puis l'intégré à volonté dans une structure photonique par une puissance d'excitation plus élevée. Le couplage d'une NP d'or et une structure photonique à base de polymère a été ensuite étudié théoriquement et expérimentalement montrant une amélioration importante de la collection des photons émis par la NP.

Contents

List of publications

Parts of the thesis have been published in:

- **Do, M. T.**, Nguyen, D. T. T., Ngo, H. M., Ledoux-Rak, I., and Lai, N. D., *Controlled coupling of a single nanoparticle in polymeric microstructure by LOPA-based direct laser writing technique,* Nanotechnology (accepted 2015).

- Nguyen, T. T. N, Luong, M. H., **Do, M. T.**, Kieu, D. M., Q. Li, Nguyen, D. T. T., Tong, Q. C., Ledoux-Rak, I., and Lai, N. D., *Micro and nanostructuration of polymer materials and applications,* **Invited Paper**, proc. SPIE **9171**, Nanobiosystems: Processing, Characterization, and Applications VII, 91710O (August 2014).

- Li, Q., **Do, M. T.**, Ledoux-Rak, I., and Lai, N. D., *Three-dimensional optical addressing by ultra low one-photon absorption microscopy,* proc. SPIE **9131**, Optical Modeling and Design III, 91310Q (May 2014).

- **Do, M. T.**, Li, Q., Ledoux-Rak, I., and Lai, N. D., *Optimization of LOPA-based direct laser writing technique for fabrication of submicrometric polymer two- and three-dimensional structures,* proc. SPIE **9127**, Optical Modelling and Design III, 91310Q (May 2014).

- **Do, M. T.**, Nguyen, T. T. N., Li, Q., Benisty, H., Ledoux-Rak, I., and Lai, N. D., *High aspect ratio submicrometer two-dimensional structures fabricated by one-photon absorption direct laser writing,* Microsystem Technologies **20(2)**, 1432–1858 (2014).

- **Do, M. T.**, Li, Q., Nguyen, T. T. N., Benisty, H., Ledoux-Rak, I., and Lai, N. D., *Submicrometer 3D structures fabrication enabled by one-photon absorption direct laser writing,* Opt. Express **21**, 20964–20973 (2013).

- Li, Q., **Do, M. T.**, Ledoux-Rak, I., and Lai, N. D., *Concept for three-dimensional optical addressing by ultralow one-photon absorption method,* Opt. Lett. **38**, 4640–4643 (2013).

Conferences attended and contributions

- Nguyen, T. T. N, Luong, M. H., **Do, M. T.**, Kieu, D. M., Q. Li, Nguyen, D. T. T., Tong, Q. C., Ledoux-Rak, I., and Lai, N. D., *Micro and nanostructuration of polymer materials and applications,* **Invited Talk**, SPIE **9171**, Nanobiosystems: Processing, Characterization, and Applications VII, 91710O, California, United States (August 2014).

- **Do, M. T.**, Li, Q., Ledoux-Rak, I., and Lai, N. D., *Optimization of LOPA-based direct laser writing technique for fabrication of submicrometric polymer three-dimensional structures,* **Oral**, SPIE Photonic Europe, Brussels, Belgium (May 2014).

- Li, Q., **Do, M. T.**, Ledoux-Rak, I., and Lai, N. D., *Three-dimensional optical addressing by ultra low one-photon absorption microscopy,* **Oral**, SPIE Photonic Europe, Brussels, Belgium (May 2014).

- **Do, M. T.**, Li, Q., Nguyen, T. T. N., Benisty, H., Ledoux-Rak, I., and Lai, N. D., *One-photon absorption direct laser writing: a novel approach for fabrication of three-dimensional sub-micrometric structures,* **Oral**, CE-9.5, The European Conference on Lasers and Electro-Optics and the International Quantum Electronics Conference (CLEO®/Europe-IQEC), Munich, Germany (May 2013).

- Li, Q., **Do, M. T.**, Benisty, H., Ledoux-Rak, I., and Lai, N. D., *3D imaging by low one-photon absorption technique,* **Poster**, The European Conference on Lasers and Electro-Optics and the International Quantum Electronics Conference (CLEO®/Europe-IQEC), Munich, Germany (May 2013).

- **Do, M. T.**, Li, Q., Nguyen, T. T. N., Benisty, H., Ledoux-Rak, I., and Lai, N. D., *Fabrication of sub-micrometer 3D structures by one-photon absorption direct laser writing,* **Poster**, NMD-P70, The 6th International Workshop on Advanced Materials Science and Nanotechnology (IWAMSN2012), Ha Long, Vietnam (November 2012).

- **Do, M. T.**, Li, Q., Nguyen, T. T. N., Benisty, H., Ledoux-Rak, I., and Lai, N. D., *Ultra low one-photon absorption (LOPA) microscopy and applications,* **Invited Talk**, MEP1-O1, The 6th International Workshop on Advanced Materials Science and Nanotechnology (IWAMSN2012), Ha Long, Vietnam (November 2012).

- **Do, M. T.**, Li, Q., Nguyen, T. T. N., Benisty, H., Ledoux-Rak, I., and Lai, N. D., *Fabrication of sub-micrometer 3D structures by LOPA direct laser writing,* **Poster**, P43, The 1st AVSE Annual Doctoral Workshop, Paris, France (September 2012).

- **Do, M. T.**, Li, Q., Nguyen, T. T. N., Benisty, H., Ledoux-Rak, I., and Lai, N. D., *Generation of sharper focal spot for super-resolution imaging and nanofabrication,* **Poster**, P34, The French Japanese Workshop - The Nanotech Revolution from Science to Society, Cachan, France (December 2011).

Acknowledgments

I am deeply grateful to my supervisor Ngoc Diep Lai. His vast knowledge and experience have been invaluable. He patiently answered hundreds of questions even if those were stupidest. His guidance is to keep me staying away from distraction. I have been stimulated and excited by his constant flow of good ideas.

I am extremely indebted and privileged to have had the support and advice of professor Isabelle Ledoux-Rak who has spent a lot of her valuable time to read my thesis line-by-line then gave back to me with many red marks and corrections.

I would like to express my gratitude to all my colleagues at LPQM for creating a nice working environment. Many thanks to all my friends who with increasing frequency have manifested their interest in my research by asking: "Will you finish soon?".

Finally, I reserve my deepest gratitude to mom, my sisters and my brother for their support, encouragement and unconditional love. My deepest gratitude from bottom of my heart is dedicated to my wife and to my daughter who have lived and breathed the thesis with me since I started. This thesis is dedicated to them.

List of Figures

Figure **Page**

Chapter 1

Introduction

Many of the true breakthroughs in our technology have resulted from a deeper understanding of the interaction of light with matter. Light-matter interaction is of fundamental importance in physics because of the possibility to manipulate light by matter and of matter by light. Many efforts have been made by many research groups all over the world leading to numerous scientific advances. The investigated light-matter principles have been continuously applied for the development of various optical devices. Among them, lasers, fiber optics, DVDs, and the entire field of photonics are the most attractive achievements. In photonic devices, photonic crystal (PC), a special kind of a sophisticated structural submicrostructure, is widely investigated by numerous researchers.

In what follows we will firstly outline some specific features and optical properties of PCs. We also introduce some important applications of PCs and focus on the current fabrication techniques of such structures. Among them, direct laser writing (DLW) is one of the most used techniques, in particular for three-dimensional (3D) PCs. We introduce the concept of the DLW technique and the typical experimental setup for DLW based on two-photon polymerization mechanism. We point out that, two-photon absorption-based DLW (TPA-DLW), although convenient for fabrication of arbitrary microstructures, is rather expensive in comparison with some common techniques based on one-photon polymerization mechanism. Finally, we introduce the motivation of thesis's work and present the plan of the thesis.

1.1 Photonic crystals

1.1.1 Color in nature

The structural control of light manifests in stone, animal and mineral worlds [1]. Birds, butterflies, squids and other creatures often sport intense or changing colors that are not formed by pigments but by highly organized nanostructures. Indeed, the organized structures are arrays of tiny structures that are just a few hundred nanometers wide [2, 3]. The color productions of these structures are related entirely to coherent scattering processes that underpin the interaction of light with materials having periodic variations of their refractive index. The intense colors of bird plumages, butterfly wings and the bodies of squid are often produced, depending on the size and spacing of these structures. Some particular wavelengths from the full spectrum of sunlight are picked out when shining on these structures. The iridescence and colors change in a way that depends on the angle at which we see the animal. And because these colors are produced just by reflecting rather than absorbing light, as pigments do, they can be more brilliant. The best-known example is opal [5] (Fig.1.1-(a_1)), a sedimentary gem offering the highly prized variety showing diffraction of visible light, called play-of-color opal. Unlike other mineral gems, opal does not have a crystalline structure. It is made of tiny spheres of silica packed together (Fig.1.1-(a_2)). Because they are spherical, there are tiny gaps remaining between the spheres. In these gaps between the stacked spheres, a water and silica in aqueous solutions remain. Spheres in an opal are not only remarkably uniform in size but are also packed, in gem quality opal, in a very regular array. These tiny spheres and gaps hold the secret of the opal's color. When white light waves enter the top of an opal, they refract and bounce around inside the opal through all the microscopic spheres and the gaps between the spheres. As light passes through spheres and gaps, it is diffracted. Like a prism, the opal splits the white light into all the colors of the spectrum, and the light eventually bounces back out the top of the stone, at which point we get an eyeful of beautiful opal colors. Opal is the only known gemstone that is able to naturally diffract light in this way. The diffraction of light through this arrangement produces a characteristic play of colors, the nature of which is determined by the size of the spheres and the

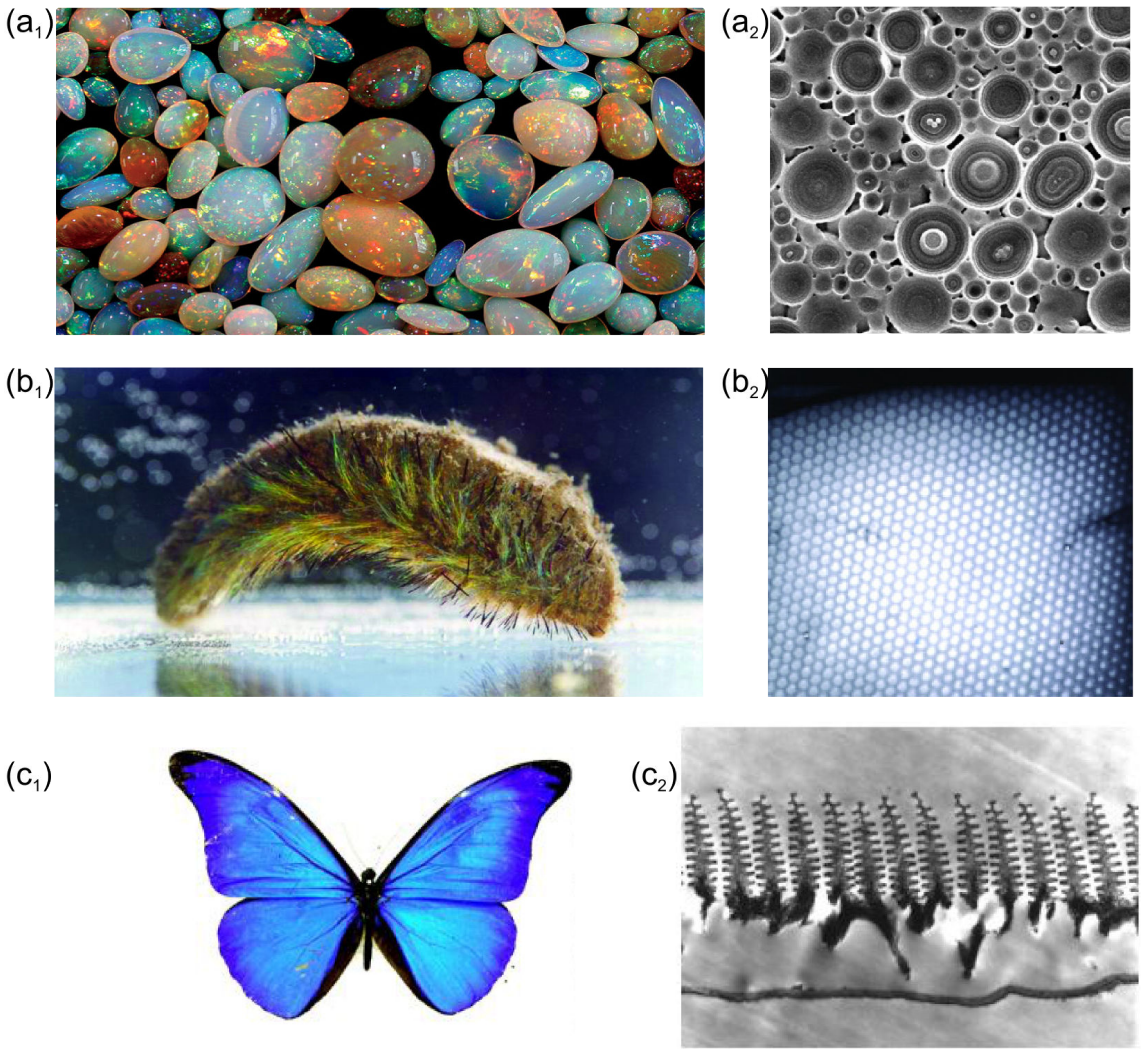

Figure 1.1: Colors in nature: (a_1) Volcanic play-of-color opals mined at Wegel Tena, Ethiopia, are mostly white, translucent to opaque, and show vivid play-of-color. (a_2) Micrograph of a common opal-A from Slovakia. Spheres have different sizes, and are made of nanograins arranged in a concentric way [4]. (b_1) A sea mouse from South Australia, (b_2) SEM cross-section of a spine reveling nanostructures. Photo from `http://www.physics.usyd.edu.au/nicolae/seamouse.html`. (c_1) The butterfly Morpho didius obtains its dazzling blue color from delicate "Christmas Tree" light-scattering structures. (c_2) "Christmas Tree" light-scattering structures made from chitin, that sprout within the wing scales. Photos (c_1) from Peter Vukusic and (c_2) from Vukusic & Sambles, Exeter University.

regularity of the periodic structure. Researchers have drawn inspiration from these gems to build artificial opals by sedimentation of spheres for commercial purposes as well as to mimic the structures for the fabrication of 3D PC [6–8].

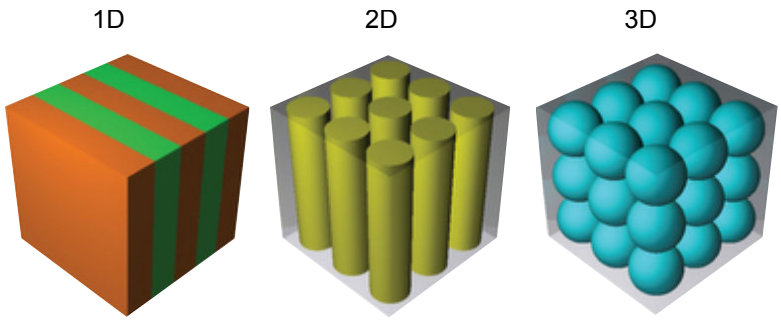

Figure 1.2: Basically, PCs can be classified in three groups: One-dimensional (1D), two-dimensional (2D), and three-dimensional (3D); depending on how many spatial coordinates are structured in a periodic manner.

Besides, a research group at the University of Sydney, Australia, has discovered that iridescence is also present in the animal world [1], specifically in the sea mouse (see Fig.1.1-(b_1)), a marine worm found in moderately deep water. The sea mouse is partly covered with long, felt-like threads that produce a brilliant iridescence, a range of colors that changes with the direction of the incident light and the direction of observation. It is also characterized by iridescent spines. A scanning electron microscope (SEM) image of a cross-section of a thread or of a spine reveals a periodic microstructured pattern with hexagonal symmetry as shown in Fig. 1.1-(b_2). Numerical studies have shown that these two-dimentional (2D) PCs possess a partial bandgap (*i.e.*, for some directions of propagation of light), which is the physical explanation of their iridescence.

Let's consider the butterfly, a species in which color is generally produced in both of the ways described above (Fig.1.1-(c_1)). For some butterflies, such as the Morpho rhetenor, one way of producing color predominates. The dazzling blue color obtained is not from simple multilayer's but from more complex nanostructures in the wing scales: arrays of ornate chitin "Christmas Trees" that sprout at the surface [9] (Fig.1.1-(c_2)). Each tree-like geometry presents a stack of disk-like layers to the incoming light, which acts as another kind of diffraction grating. These arrays may reflect up to 80 percent of the incident blue light. And because they are not flat, they can reflect a single color over a range of viewing angles, somewhat reducing the iridescence (organisms don't always want to change color or get dimmer when seen from different directions).

Opal, sea mouse, butterfly from three examples above as well as many other

creatures in nature possess a common important feature, with that the capability of producing colors and being iridescence is defined, that is the periodicity of material in space at optical wavelength scales.

1.1.2 Photonic crystals

In the late 1980s the modern field of photonic structures was born. The development was principally boosted by two milestone papers of John [10] and of Yablonovitch [11], 100 ans after the first experiment with periodic multilayer dielectric stacks made by Lord Rayleigh [12]. A periodic array of materials with different refractive indices is called PC. The attribute "photonic" indicates that the structural periodicity is on the scale of the wavelength of the radiation field. The development relied on an analogy between electrons propagating through solid matter with a periodic potential and photons propagating through a periodic dielectric structure. A crystal, by definition, is a periodic arrangement of atoms or molecules. The pattern with which the atoms or molecules are repeated in space is the crystal lattice. The crystal presents a periodic potential to an electron propagating through it, and both the constituents of the crystal and the geometry of the lattice dictate the conduction properties of the crystal. The theory of quantum mechanics in a periodic potential explains what was once a great mystery of physics: in a conducting crystal, electrons propagate as waves, and waves that meet certain criteria can travel through a periodic potential without scattering. Importantly, however, the lattice can also prohibit the propagation of certain waves. There may be gaps in the energy band structure of the crystal, meaning that electrons are forbidden to propagate with certain energies in a particular directions. If the lattice potential is strong enough, the gap can extend to cover all possible propagation directions, resulting in a complete band gap, *i.e.*, a gap between the valence and conduction energy bands.

The optical analogue is the PC, in which atoms or molecules are replaced by macroscopic media with different dielectric constants, and the periodic potential is replaced by a periodic dielectric function (or, equivalently, a periodic index of refraction). If the dielectric constants of the materials in the crystal are sufficiently different, and if the absorption of light by the materials is minimal, then the refractions and reflections

of light from all of the various interfaces can produce the same phenomena for photons (light modes) as those the atomic potential produces for electrons.

Photonic bangap

In order to gain more understanding on how light in a PC can be manipulated, one must derive the eigenvalue problem of the Maxwell's equation for electromagnetic wave in a generalized periodic dielectric medium. The study of wave propagation in three-dimensionally periodic media was pioneered by Bloch in 1928 [13], unknowingly extending an 1883 theorem valid in one dimension by Floquet [14]. Bloch proved that waves in such a medium can propagate without scattering, their behavior governed by a periodic envelope function multiplied by a planewave. Although Bloch studied quantum mechanics, leading to the surprising result that electrons in a conductor scatter only from imperfections and not from the periodic ions, the same techniques can be applied to electromagnetism by casting Maxwell's equations as an eigenproblem in analogy with Schrödinger's equation. By combining the source-free Faraday's and Ampere's laws at a fixed frequency ω, i.e. time dependence $e^{-i\omega t}$, one can obtain an equation for the magnetic field (also for electric field) in a modulated medium $\mathbf{H}(\mathbf{r})$:

$$\nabla \times \frac{1}{\epsilon(\mathbf{r})} \nabla \times \mathbf{H}(\mathbf{r}) = \left(\frac{\omega}{c}\right)^2 \mathbf{H}(\mathbf{r}), \tag{1.1}$$

where $\mathbf{H}(\mathbf{r})$ is the magnetic field of photon, ω is frequency, c is the speed of light and $\epsilon(\mathbf{r})$ is the macroscopic dielectric function. This is an eigenvalue equation with eigenvalue $(\omega/c)^2$ and an eigen-operator $\nabla \times \frac{1}{\epsilon(\mathbf{r})} \nabla \times$. The solutions $\mathbf{H}(\mathbf{r})$ and ω are determined completely by the strength and symmetricity of $\epsilon(\mathbf{r})$. If $\epsilon(\mathbf{r})$ is perfectly periodic, as in a perfect PC, the solutions are characterized by a wavevector $\mathbf{k}$ and a band index n. The region of all allowed wavevectors is called a Brillouin zone and the collection of all solutions is termed a band structure. A complete photonic band gap (PBG) is a range of ω in the band structure in which there are no propagating solutions of Maxwell's equations for any $\mathbf{k}$, surrounded by propagating states above and below the gap. There are also incomplete PBG, which only exist for a subset of all possible wavevectors, polarizations, and/or symmetries. The photonic band structure related to simple one-dimensional (1D) multilayers can be considered using basic ideas of interference. For example, Fig. 1.3-(a) shows the dispersive diagram

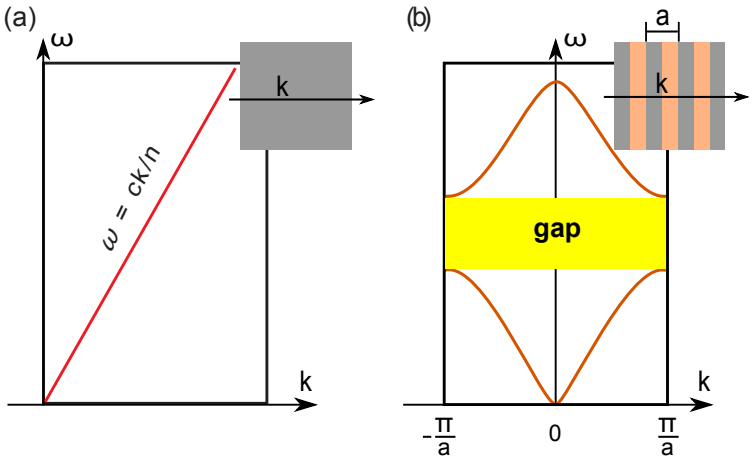

Figure 1.3: (a) Dispersion relation (band diagram) of light, frequency ω versus wavenumber k, in conventional materials; (b) Schematic effect on the bands of a physical periodic dielectric variation (inset), where a gap has been opened by splitting the degeneracy at the $k = \pm\pi/a$, Brillouin-zone boundaries.

of light in uniform media, which is given approximately by $\omega = ck/n$. When the dielectric function of media is perturbed, suppose that we perturb ϵ so that it is nontrivially periodic with period a. An example of a 1D PC shown in the inset of Fig. 1.3-(b). In this case, the band is split at the $k = \pm\pi/a$, a small gap is therefore obtained. Generally, it follows that any periodic dielectric variation in one dimension will lead to a band gap, albeit a small gap for a small variation. A perturbation of ϵ dielectric function in 2D and 3D configurations is rather complicated, but obeys the same mechanism.

As a practical example, a 3D structure as shown in Fig.1.4-(a) is formed by an alternating hole-slab/rod-slab sequence in an ABCABC stacking of bilayers-equivalently. This structure is a face-centered cubic (fcc) lattice of air cylinders in dielectric, stacked and oriented in the <111> direction, where each overlapping layer of cylinders forms a rod/hole bilayer simultaneously. Its band diagram is shown in Fig.1.4-(b) along the boundaries of its irreducible Brillouin zone (from a truncated octahedron, inset), and this structure has a complete gap of 21% ($\Delta\omega$ as a fraction of mid-gap frequency) for $\epsilon = 12/1$, forbidding light propagation for all wavevectors (directions) and all polarizations [15]. Its fabrication, of course, is more complex than that of PC slabs (with a minimum ϵ contrast of 4/1), but this and other 3D PC structures have been

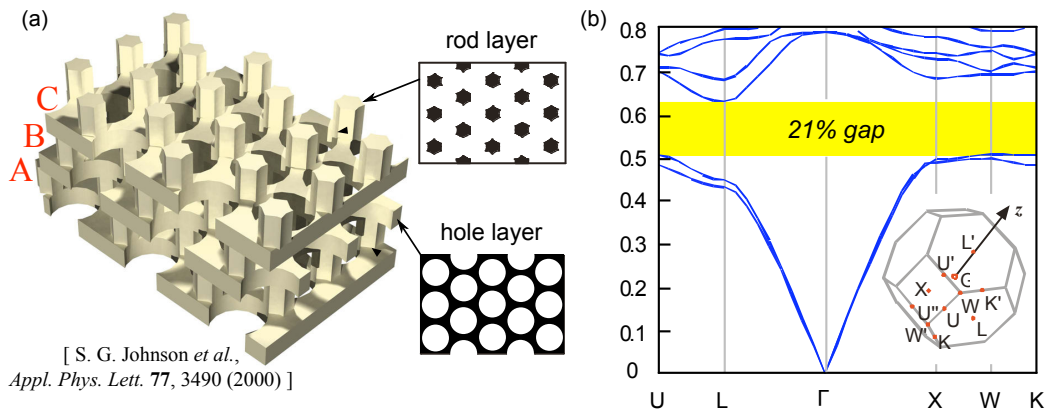

Figure 1.4: Band diagram (right) for a 3D-periodic PC (left) consisting of an alternating stack of rod and hole 2D-periodic slabs, with the corners of the irreducible Brillouin zone labeled in the inset. This structure exhibits a 21% omnidirectional band gap [15].

constructed even at micron (infrared) length scales [16, 17].

Thanks to many specific optical properties, PCs have been found in many applications for photonic devices that we will briefly overview as following.

1.2 Applications of photonic crystals

1.2.1 Role of defects in photonic crystal applications

Once we have a PC with a PBG we can introduce a defect to attempt to trap or localize light. If we use a line defect (see an example of line defect in Fig.1.5-(a)), we can guide light from one location to another. The basic idea is to carve a waveguide out of an otherwise-perfect PC. Indeed, light that propagates in the waveguide with a frequency within the ban gap of the crystal is confined to, and can be directed along, the waveguide. This is a truly novel mechanism for guiding of light with great advantages. Actually, light can be guided with very low losses within dielectric waveguides such as fiber optics cables, which currently rely exclusively on total internal reflection. But, if a fiber optic cable carved tightly, the incidence angle is too large for total internal reflection to occur, so light escapes at the corners and is lost. Differently, in PC, the propagation light continues to be confined even around tight corners with extremely low loss. This feature results in a great advantage for photonic microdevices.

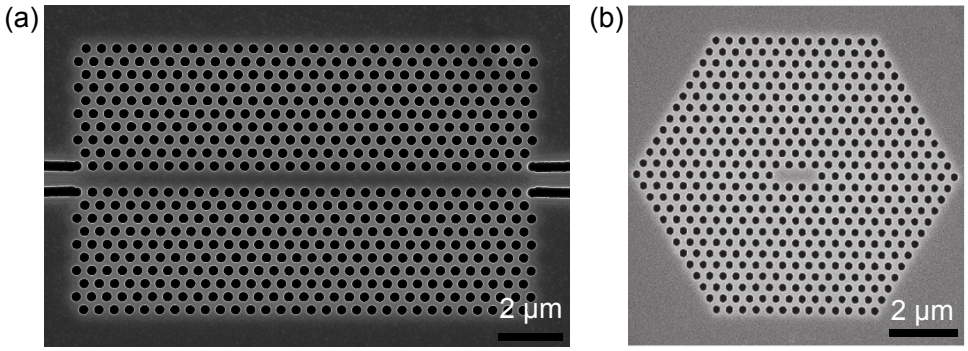

Figure 1.5: Waveguide and cavity defects in PC. (a) SEM image of a waveguide structure [image from Ref. [18]]. (b) Single point defect on a 2D PC slap, [image from Ref. [19]].

Besides, one can also create imperfection to trap light in a point within the crystal. One class of imperfection of this type involves a change of the dielectric medium in some local region of the crystal, deep within the bulk. As a simple example, consider making a change to a single 'dielectric atom' by modifying its dielectric constant, or its size, or simply removing it from the crystal. Figure 1.5-(b) shows a SEM image of a 2D PC point defect , which consists of three missing holes in a central line. The holes are designed as regular hexagons with side length of 100 nm and the periodicity of 300 nm. This device was designed for enhancing light emission from emitters embedded in an optical cavity.

A defect designed in PC is a very important feature for many applications because of its capability to trap and localize light. The manipulation of light by such a way has been found applicable in a broad band of applications, for example fiber optics, ultra-low threshold laser, nonlinear optics devices and single photon source.

1.2.2 Photonic crystal fiber

An intriguing aspect of PC waveguides is that they provide a mean to guide tractably and efficiently light through a narrow channel. Figure 1.6 shows some fused-silica optical fibers that have a regular pattern of voids, or air holes, that run parallel to its axis fiber. Unlike traditional fibers where both core and cladding are made from a dense material, the presence of the voids in PC fiber is the main factor for rising

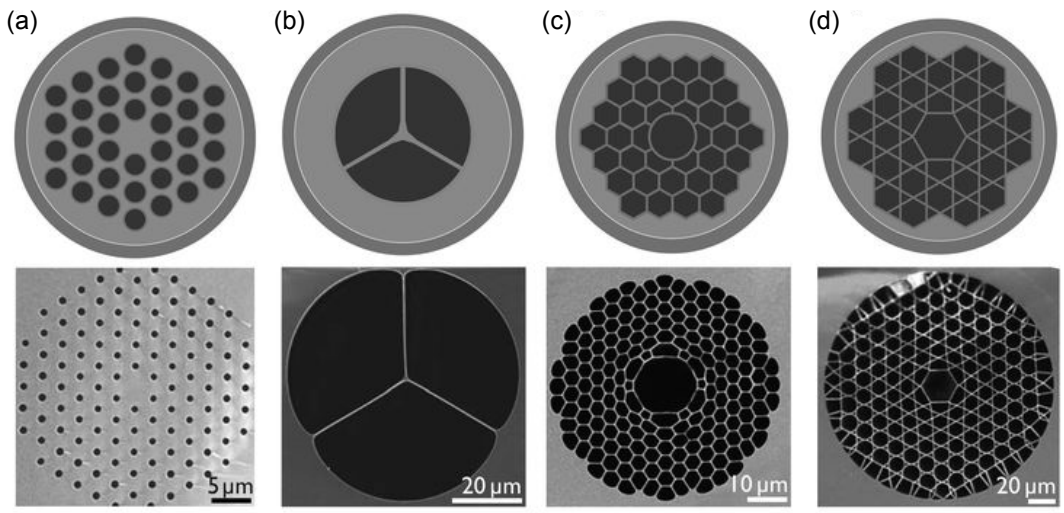

Figure 1.6: Schematic sketch of the PC fiber geometry (top) and SEM images of the core and surrounding cladding for (a) a SC-PC fiber; (b) a suspended-core PC fiber; (c) a HC-PBGF and (d) a kagomé HC-PC fiber [20].

its particular waveguiding properties. Indeed, wavelengths that fall within the PC's bandgap cannot propagate out and are thus confined within the core. As a result, the core can even have a lower index of refraction than the cladding.

A fantastic application of PC fiber nowadays is the generation of continuum sources [21, 22]. In this application, photonic crystal properties are combined with nonlinear properties allowing to generate a broad and coherent light source, which cannot be achieved by other standard materials.

1.2.3 Photonic crystal laser

Exploiting the capability of trapping light within a finite volume allows one to develop a new class of PC laser. A nanocavity in a PC laser is a "defect" region in a microstructured region of a high refractive index material. The existence of a PBG of the crystal allows to modify the density of electromagnetic modes and thus to enhance or suppress spontaneous emission. A local emission at the defect is therefore strongly confined and amplified. In other words, the PC plays the role of a perfect mirror around the defect. A PC laser is made by etching an array of holes into a material resulting in a microstructured zone with high refractive-index contrast between the air and the material. The difference in refractive index between the material and the

surrounding air provides feedback to trigger laser emission in the vertical direction.

Until now, most PC lasers are realized with semiconductor materials by using a combination of different techniques. For example, a 2D PC laser represented in Fig. 1.7 was formed in indium gallium arsenic phosphide (InGaAsP). A single defect was designed in a 2D PC to trap photons inside the laser structure. The fabrication of the laser cavities by mean of metalorganic chemical vapor deposition (MOCVD) and the fabrication of the defect cavity required a number of dry etching steps followed by a wet etching technique. The fabrication of the 2D PC was patterned using electron-beam lithography. Figure 1.7-(b) shows a SEM micrograph of a top view of the fabricated microcavity by using these techniques [23].

Other than PC laser, PC based micro- and nano-cavity can be used in many other applications such as enhancement of nonlinear optics effects, a manipulation of optical properties of single emitters. Importantly, the development of PC based micro- nano-cavity are all related to the enhancement of localized optical effects via the coupling of a single emitter to photonic devices. This interesting feature will be discussed in following section.

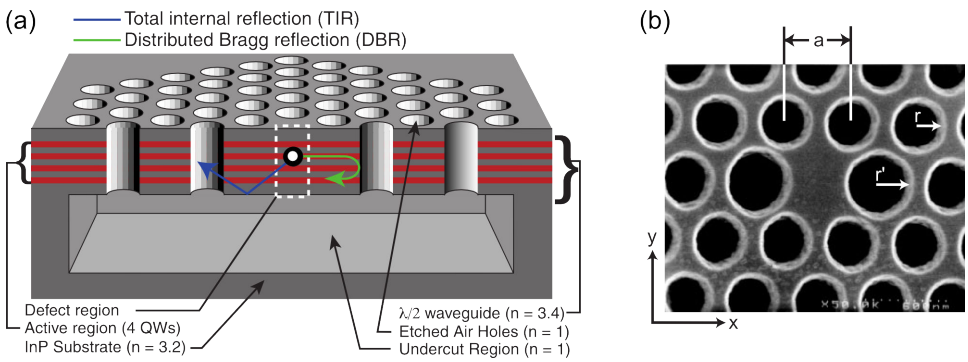

Figure 1.7: (a) Cross section through the middle of the photonic crystal microcavity. A defect is formed in the 2D photonic crystal by removing a single hole, thus forming an energy well for photons similar to that for electrons in a quantum wire structure. Photons are also localized vertically by TIR at the air-slab interface. The combination of Bragg reflection from the 2D photonic crystal and TIR from the low-index cladding (air) results in a three-dimensionally confined optical mode. (b) Top view of a microfabricated 2D hexagonal array of air holes in a thin membrane with a central hole missing. Photo from Ref. [23]

1.2.4 Coupling of single emitters to photonic crystals

Rising from the past decade, in the field of physics, especially in quantum physics, wavelength-scale photonic devices embedding a single fluorescent nano-object has draw a great deal of interest of many researchers. Indeed, a macroscopic photonic device containing a single emitter is considered as a atomic-like two-level system (or as an atom of two energy levels), which permits unidirectionally output one photon at a time. This kind of system is on the way to realize a solid-state single photon source whose applications are very promising in quantum information processing, quantum keys and quantum cryptography [24, 25]. Once embedded in a photonic device, the cavity-emitter system can perform a task for quantum information processing. In such a case, if the emitter can be in a strong coupling regime with a cavity mode, the Purcell effect lead possibly to realize a controlled entanglement of distinguishable quantum systems. Realizing these tasks in the solid state is clearly desirable, and coupling semiconductor quantum dots (QDs), or a single nitrogen-vacancy (N-V) color center in diamond or a single plasmonic nanoparticle to PC cavities is a promising route for this purpose [26–33].

A typical example of quantum dots-PC coupling is the experiment made by Albert *et al.* in ref. [34]. In this experiment, quantum dots are coupled into solid state micropillar cavities using the strong exciton–photon coupling regime. Micopillars (sketch is shown in Fig. 1.8-(a)) consist in self-assembled InGaAs quantum dots and two Bragg reflectors (DBRs). The DBR is a PC-based system, which is composed of $\lambda/4$ stacked GaAs–AlAs layers that are grown by molecular beam epitaxy with 26 (30) mirror pairs in the top (bottom) DBR. A layer of self-assembled $In_{0.4}Ga_{0.6}As$ QDs with a ground-state excitonic transition around 930 nm was inserted at the antinode of the confined photon field in the λ-GaAs spacer. The as-grown planar microcavity was dry-etched into the pillar structures, providing in-plane photon confinement. In inset of Fig. 1.8-(a), a "Nano-towers fire off single photons" is an experimental realization of such kind of quantum dots-PC system [37].

Figure 1.8-(b) shows an experiment made by Barth *et al.* in ref. [36]. In this experiment, they used individual metal nanoparticles that are deterministically placed on the dielectric backbone of a PC cavity by the use of an atomic force microscope tip.

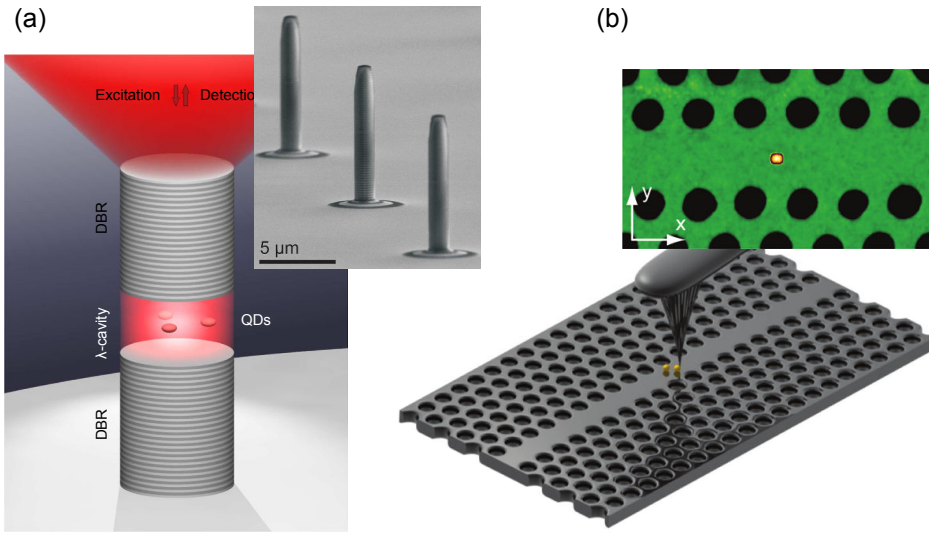

Figure 1.8: (a) Quantum dot - micropillar system: Sketch of the investigated micropillar cavity and fluorescence characterization of the strong-coupling regime. [34, 35]. Inset shows the "Nano-towers fire off single photons". (b) A cartoon of the planar double-heterostructure PC cavity and gold nanoparticles in an experiment for Tailored Light-Matter Coupling (bottom) and atomic force microscope (AFM) images of a PC cavity with a gold nanorod placed on top of the PC structure (top) [36].

This type of hybrid structure can exhibit both high quality factors and a pronounced hot spot of the electromagnetic field, potentially enhancing the interaction of the cavity mode with emitters or other types of active materials.

Besides the use of QDs and plasmonic nanoparticles as active materials coupled with PC-based devices, many researchers use N-V color centers instead. In most cases, the objective is to realize a solid state single photon source [37–39] based on micropillars, nanowire antennas, microdisks or 2D PCs [36]. Experiments with N-V centers are more difficult than those dealing with QDs or plasmonic nanoparticles since N-Vs are randomly located in the diamond lattice. The controlled creation and localization of a N-V center in diamond for efficient coupling into PCs still remain a significant challenge [40].

1.2.5 Discussions

Although PCs have found widespread applications in many areas, the realization of such kind of photonic structures at the nano scale remains a great challenge [41–43].

The first challenge relates to the material choice, which should present a high dielectric contrast in order to obtain a complete PBG. The second one relates to the fabrication method, which should allow to achieve controllable and fine structural feature, such as high resolution lithographic techniques.

- **Materials** are generally required to (*i*) be transparent over the range of PC frequency operation; (*ii*) display a high dielectric contrast (PBG conditions); (*iii*) be able to couple to active materials; and (*iv*) be relevant and easily adapted to the chosen fabrication method.

- **Fabrication techniques** should: (*i*) be able to fabricate 1D, 2D and 3D PCs with sub-wavelength feature size; (*ii*) be rapid, not complicated and inexpensive; (*iii*) be capable of engineering arbitrary defects at accurate and arbitrary positions inside the crystal; and (*iv*) not destroy or damage the used materials.

1.3 Methods for photonic crystal fabrication

Depending on materials and applications, different techniques have been identified for the fabrication of multi-dimensional PCs. It is worth to mention some powerful techniques, such as micromachining, colloidal self-assembly, interference photolithography and direct laser writing.

- **Micromachining** is a basic technology for fabrication of micro-components of size in the range of 1-500 micrometers. This approach has allowed the fabrication of PCs for near-IR domain from high refractive index semiconductors. Micromachining can be done by a combination of various techniques (photolithography, etching, LIGA, laser ablation, mechanical micromachining). For example, Lin and collaborators created a so-called "woodpile micromachined" arrangement [44] (see Fig. 1.9-(a)). In this technique, the periodic array is build up by depositing lines of polycrystalline silicon into micron sized SiO_2 trenches in successive layers. Once the structure is built up, SiO_2 is removed with HF, leaving a silicon-air PC. Noda *et al.* have produced some kinds of PCs in GaAs using a similar layering concept [45]. These PCs are created by carefully aligning, stacking, and fusing

prefabricated GaAs wafers together with subsequent chemical- and dry-etching processes.

- **Colloidal self-assembly** or self-assembly of colloidal microspheres or nanospheres is a parallel fabrication technique based on chemical deposition. The structures fabricated by this technique consists of low-refractive-index colloidal microspheres, which are self-organized in close-packed (fcc) crystals by surface forces. These crystals can be back-filled with a high index material, out of which the original spheres are dissolved in order to form inverse-opal crystals with a complete gap [46]. A typical example of such submicrostructures can be seen in Fig. 1.9-(b), where a billion SiO_2 microspheres of about 250 nm diameters are arranged in a fcc crystal. So far, colloidal self-assembly is still considered as an effective strategy for the fabrication of ordered micro- or nano-structures [47].

- **Inteference lithography**: An elegant approach, as described in reference [48], uses a four-beam holographic method to create a 3D periodic interference pattern in a block of photoresist. The high intensity regions of the interference pattern render the photoresist insoluble, allowing a 3D periodic material to be formed (Fig. 1.9-(c)). The holographic technique has the advantage of speed since the entire pattern in the photoresist is created within a few seconds. However, we note that the choice of photonic structures fabricated by this four-beam interference is limited. Recently, by using two-beam interference with a multi-exposure technique, Lai *et al.* demonstrated that it is possible to fabricated many other kinds of 2D and 3D PCs [49, 50]. It remains to be tested to what degree ideal defect-free structures can be experimentally realized, how the absorption of the laser beams affects the thickness uniformity, and how intentional defects and waveguides could be incorporated in those structures.

- **Direct laser writing** (DLW): This technique, as we will discuss in more detail in the next section is usually based on two-photon polymerization of a photosensitive material. It has emerged as a technique for the rapid, cheap and flexible fabrication of nanostructures for photonic applications. As an example, Hiroaki Misawa *et al.* demonstrated the fabrication of a 3D spiral PC with stop

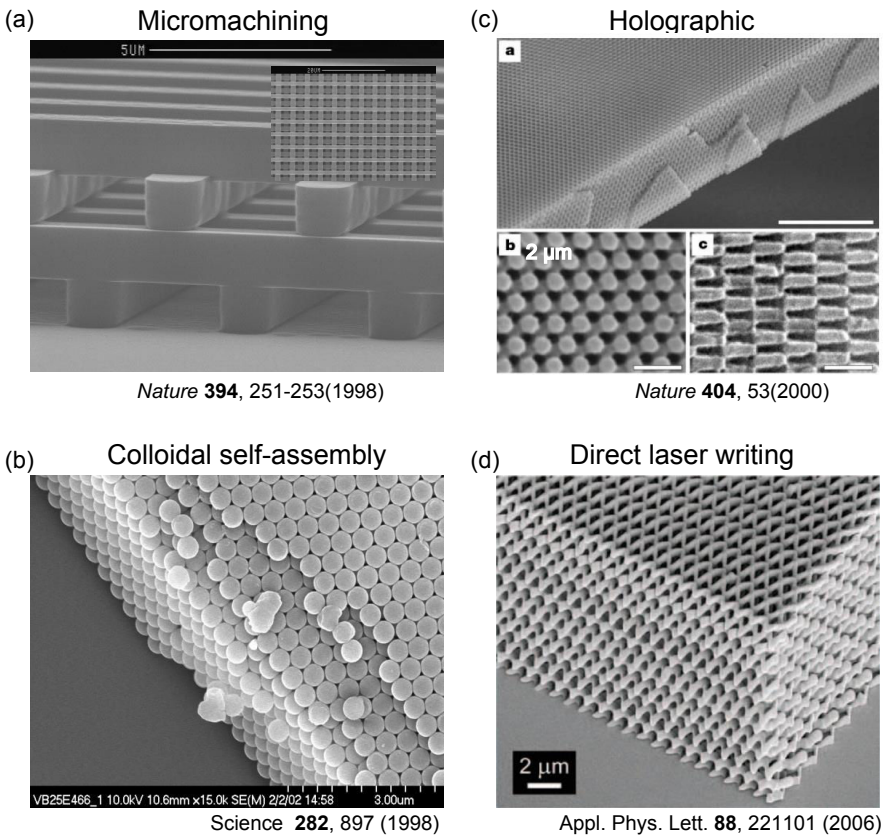

Figure 1.9: Some common techniques for fabrication of PCs. Micro-machining, colloidal self-assembly, interference photolithography and direct laser writing.

gaps below 1 μm as shown in Fig. 1.9-(c) this sample was fabricated in a 25 μm SU-8 film prepared by spin coating on a glass substrate [51].

Although these techniques have been demonstrated for successful fabrication of PCs, each one having their disadvantages. For example, the micromachining method requires a complex and expensive optical system for achieving ultrahigh-precision alignment. In addition, direct layer-by-layer micromachining is an expensive, inflexible, high-risk, and time consuming approach [52]. The second approach, which can generate structures at the molecular level with sub-nanometer precision. But external forces and geometrical constraints can alter the outcome of a self-assembly process, thus resulting in a distortion of the resulted PC. Interference lithography, although offering uniform, large area and very rapid, is impossible to design arbitrary shapes of PCs and does not allows to create defect at will.

DLW is time consuming and also quite expensive. But, out of that limitation, DLW is very suitable for the fabrication of any desired 2D and 3D PCs at sub-micrometer scale. Therefore, we present in the next section more detail about this fabrication technique.

1.4 Direct laser writing

It is well-known that there are two types of absorption mechanisms in photosensitive material (photoresist), namely one-photon absorption (OPA) and two- (or more) photon absorption (TPA). OPA requires only one photon of the incident light to excite a molecule. This is a linear absorption process, because the number of excited states is linearly proportional to the intensity of the incident light. In contrast, in TPA, a molecule needs two (or more) photons simultaneously to be excited. This process is nonlinear because the probability to bring a molecule from its ground state to an excited state depends non-linearly on the intensity of the incident light.

The fabrication of PCs by DLW technique can be realized by OPA or TPA mechanism. However, until now, only the TPA-based DLW technique allows to realize submicrometer 3D PCs. A DLW system can be divided into three main components: (1) light source, (2) beam delivery system, and (3) substrate/target mounting and translation system. For the light source, different lasers can be used, such as an ultrafast femtosecond, or continuous-wave laser. To chose an appropriate source, one must consider the fundamental interaction of laser with the material of interest. For beam delivery, there is a variety of ways to generate a tiny laser spot, including fixed focusing objectives and mirrors, optical fibers, or even fluidic system such as liquid-core waveguides or water jets. The choice depends on the desired application, such as with various adjustable parameters, required working distances, focus spot size, or required energy. The ultimate beam properties will be determined by the combination of laser and beam delivery optics. Finally, the substrate mounting and translation system is a piezoelectronic device, which allows to move the focusing spot of the laser beam with respect to the sample (or the sample to the focusing spot). The fabricated structure is pre-designed by using a computer-aided design (CAD) model, which commands the movement of the piezoelectric system via a computer of control. The accuracy and

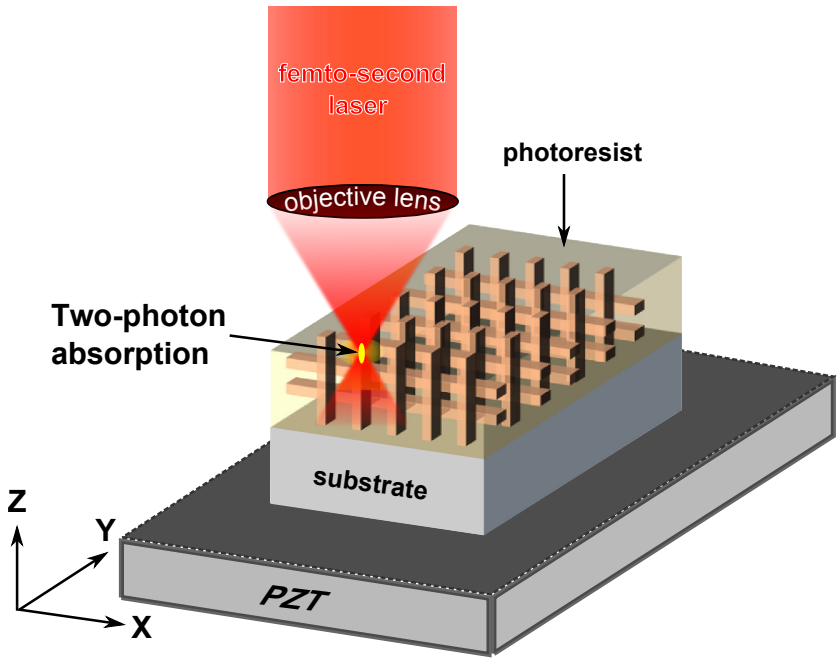

Figure 1.10: Schematic illustration of a direct laser writing system. PZT: 3D piezoelectric translator.

resolution of the movement, hence the spatial resolution of the fabricated structures, depend on the technology of translation stage and the quality of the optical focusing system.

The basic experimental setup used for DLW is illustrated in Fig. 1.10. In order to induce a TPA effect, a femto-second laser, usually a Ti:sapphire laser emitting around 800 nm is used as an excitation light source. The beam is tightly focused into a sub-micrometer spot by using a high numerical aperture objective lens. Only at this focus region, the intensity is high enough to induce the TPA effect, resulting in a polymerized structure. By moving this focusing spot, desired 3D structures can be created. To do so, the sample is mounted on a 3D translator piezoelectric scanning stage that provides the accuracy to pattern the resist with arbitrary 3D trajectories in a volume of $300 \times 300 \times 300$ μm^3. Additionally, an another motorized scanning stage can be moved laterally in an area of 10 cm$\times$ 10 cm for pre-alignment. All important features and electric components are addressed by a control software programmed in Labview or any automation packages incorporated with C, Matlab or Igor.

This TPA-based DLW allows to fabricate different photonic structures, which can

be used in different domains, such as photonic, biology, microfluidics, *etc.*

1.5 Motivation and outline of the thesis

As discussed above, various techniques have been identified for fabrication of sub-micrometer 2D and 3D PCs. Each method has its own advantages and disadvantages. The limitations of these techniques are either the accuracy or the flexibility or the cost or the consuming time for fabrication. Depending on the desired application, a suitable technique can be employed. Concerning optical lithography, the interference technique, for example, allows to fabricate rapidly PCs of large areas, but it does not allow to create defect on demand. DLW appears to be an excellent candidate because it allows for the fabrication of any kind of structures with or without defects at a sub-micrometer scale. However, some disadvantages still remain for this technique in comparison with other techniques mentioned above. Indeed, in a DLW system, a femto-second laser source and its accompanying optical components, which are rather expensive, are required.

The motivation of the thesis is directed by the idea of how to simplify the DLW system and to reduce its cost. We therefore realized theoretically a novel method to fulfill this motivation.

This thesis is organized as follows:

- In **Chapter 1** we outline some fundamental aspects of PCs: A brief overview of optical properties, applications and different techniques for fabrication of PCs. We describe briefly the operation mechanism of TPA-based DLW, and point out the motivation of the thesis.

- **Chapter 2** is devoted to the theory of focusing of electromagnetic waves in absorbing media based on the formulation of the Debye's diffraction theory. Results of this chapter guide us to fabricate desired 2D and 3D PCs.

- The first part of **Chapter 3** deals with the experimental setup and characterization of a DLW system based on OPA mechanism. In the last part of the chapter,

we present our first experiment of OPA-based DLW in a modest absoption regime in order to fabricate desired 1D and 2D sub-micrometer structures.

- **Chapter 4** is dedicated to a new fabrication technique, called low one-photon absorption (LOPA)-based DLW. We show that any sub-micrometer structures can be fabricated by this simple and inexpensive technique. 1D (nanograting structures), 2D (micropillar structures) and 3D - (woodpile, spiral and chiral twisted) structures are successfully fabricated.

- In **Chapter 5** we outline some effects which may cause the structures fabricated by LOPA technique being shrunk or distorted. We propose and demonstrate our strategy to deal with the accumulative nature of the linear absorption to improve the resolution of the fabricated structures.

- In **Chapter 6**, we show our experimental realization of coupling single fluorescent nanoparticles into micro-structure. This is realized by the LOPA technique with a double-step process. We show an example of successfully coupling a single gold nanoparticle into a spherical-shape polymeric micro-structure. This coupling regime allows to enhance the fluorescence of single nanoparticles.

- Finally, we summarize the main results obtained within the frame of the thesis and give an outlook of future experiment and research activities that will aim at gaining further insights into the specific application of LOPA technique.

Chapter 2

Focusing of electromagnetic waves in absorbing media

2.1 Introduction

Electromagnetic waves traveling from medium to medium with different refractive indices and different optical properties have been extensively studied by a number of authors. Of particular interest from both theoretical and practical points of view is the diffracted-light distribution in the region of focus when light is focused by a microscope objective lens. These investigations have contributed a lot in the domain of optical microscopy to design better objective lenses, especially those with high numerical apertures, as well as for high resolution optical imaging.

The literature that deals with the general focusing problem of electromagnetic waves is well established since the basic theory proposed by Peter Debye from the early nineteenth century for a superposition of homogeneous plane waves propagating away from the aperture plane in a specific range of directions [53]. In 1959, Wolf [54] was the first scientist who extended the Debye integral for high aperture focusing of electromagnetic waves in a single homogeneous medium. His elegant theory was the representation of the angular spectrum of plane waves, from which integral formula similar to the Debye integral were obtained. This work paved the way to further development of propagation and focalization of a light beam [55–62]. Authors derived an exact solution of the homogeneous wave equation and demonstrated the validity

of the extended Debye integral for systems that satisfy the high aperture condition. Gasper *et al.* [56] demonstrated a rigorous solution of the problem and obtained its asymptotic approximation and the derived expression for electric and magnetic fields. They also used the presentation of the angular spectrum of plane waves and considered the focusing problem for isotropic homogeneous media. Ling and Lee [59] treated the focusing of electromagnetic waves through an interface. A boundary condition in the form of a current distribution was used as a starting point, and the representation of the angular spectrum of plane waves was also applied. In a semi-geometrical approach, with the use of the stationary-phase method, expressions were obtained for electric and magnetic fields. However, because of the complexity of their theory, the use of their formulas for the computation of the electromagnetic field near focus was not practical in most cases. In 1976, Gasper *et al.* were the pioneer research group who considered an arbitrary electromagnetic wave as it travels through a planar interface. Ji and Hongo [60] treated the different problems of a point source and a spherical dielectric interface, using Maslov's method, to obtain the electric field in the focal region. A comprehensive treatment of different focusing theories was later given by Stamnes [63]. In 1993, Hell *et al.* [64] considered the focusing problem for mismatch refractive index (MRI) materials using the Fresnel-Kirchhoff integral. They decomposed the incident electric vector into s- and p-polarized parts and also calculated the effect of spherical aberration on the image formation for a confocal fluorescence microscope. However, the integral formula that they used is derived from the Green's theorem, which requires the continuity of the field and of its first and second derivatives within and on the boundary of the area of integration. This is not the case for the normal component of the electric field and the tangential component of the magnetic field, and so the final integral formula obtained may not be rigorously correct. It is not until the work of Torök et co-workers [65] the focusing of electromagnetic waves through a planar interface between materials of mismatched refractive indices was fully described by the mean of matrix formalism. They extended Richards-Wolf's theory of a high-aperture glass lens which focuses light through media with different refractive indices while introducing a considerable amount of spherical aberration. Later, they extended their formulation for a stratified media with difference refractive indices and proposed an analytic solution approximation

for Debye-Wolf integrals and calculation methods. Almost at the same time, it was shown independently by Wiersma and Visser [66] how to obtain the field in the second medium by using a completely different method. They used a vectorial diffraction theory, so-called m-theory by several contemporary workers. However, the performance of all aforementioned authors' formulations were numerically time-consuming and usually suffered a fast oscillation by diffraction integrals which may cause numerical artifacts. On the way for improving this, Leutenegger *et al.* [67] and Lin *et al.* [68] proposed fast calculation techniques by using Fourier transform to obtain a numeric diffraction performance. The calculation method given by Leutenegger *et al.* is faster by 40× in comparison with the classical methods by direct integration.

So far, the literature uses different formalism models. Most of these models were made by approximations of some rigorous solutions [56]. However, exact solutions of either Maxwell's or the wave equation have also been obtained [69]. Among many approaches and formalisms, the ones given by Torök *et al.* [65], by Wiersma and Visser [66] and by Leutenegger *et al.* [67] are often used because of the facilities for numerically calculations. Equations or the wave equation have also been obtained.

From our knowledge we have noticed that, although the diffraction of light which is focused through a planar interface between materials of mismatched refractive indices has been extensively investigated, no attention has been paid to electromagnetic wave focused into an absorbing media - the situation is usually encountered in practice when light is focused into photosensitive materials through an oil or glass medium. The investigation of the electromagnetic waves propagating in an absorbing medium is not trivial when light is attenuated when traveling through. In an absorbing medium, the refractive index is no longer determined by a single real quantity but by a complex representation. The wave vector, hence, is no longer a real vector but is determined by a complex vector, which is elliptically represented. There is a number of papers which deal with the propagation of electromagnetic waves through single or double interfaces between homogeneous isotropic and lossy media by using the ray tracing method [70–81]. A general complex ray-tracing method is proposed to determine the refractive indices, wave vectors, ray vectors (or Poynting vectors), and the polarization directions of the refracted waves for an arbitrary direction of incidence and arbitrary orientation of principal axes. Some "rigorous" expressions for the reflection and transmission

coefficients derived by the papers of these authors were expressed in various manner [82–86]. All these theories allow to explain experimental observations in different situations.

In the nanofabrication domain, an expensive example is direct laser writing (DLW) where light is focused into a photoresist. The investigation of the electromagnetic wave focused into such an absorbing medium is important in DLW because that, when light is focused in photoresists, the intensity of the focusing spot is continuously attenuated as a function of depth from the interface (between a transparent medium and a photoresist). The size and shape of the solidified volume at the focal region are completely defined by a threshold (which is proportional to the iso-intensity level at the focal region), at which the significant polymerization reactions occur.

The purpose of this chapter is to extend Wolf's treatment of the diffraction problem for the case when an electromagnetic wave is focused into an absorbing medium, in order to get a deep insight about the physics of the focusing spot formation, which is then applied for DLW.

The presentation of this chapter is as follows: In Section 2.2 we follow the same approach previously established by Torök for lossless media to derive the integral representation of the electromagnetic field in lossy media at the image space. In this section we also decompose the electric and magnetic vectors propagating through the optical system. In Section 2.3 we make use of the above results and give simplified formulas for the electric and magnetic fields in the second material. Then we introduce a numerical computation based on Matlab simulation to investigate the structure of the diffraction pattern at the focal region of a high numerical aperture (NA) objective lens (OL) for two general cases - without absorption and with absorption. Finally, we conclude our findings of this chapter and discuss about the possibility of introducing a new optical microscope with low absorption effect.

2.2 Focusing of electromagnetic waves into an absorbing medium

As mentioned before, Torök et co-workers have obtained a rigorous solution for focused electromagnetic waves in a stratified lossless media [65]. In order to establish the formulation of an inhomogeneous wave in absorbing media, we adapted their approach to derive the electromagnetic field just before the interface between two media. The field across the interface obeys the general Snell's law of refraction that Fedorov and Nakajimawe have recently obtained [87] (we introduce their formulations in appendix A) for individuals plane waves incident upon the interface. The field derived just after the interface is used as the boundary condition for a second set of integral formula corresponding to a superposition of plane waves, which describe the field inside the second medium. In this way the diffraction problem is solved in a rigorous mathematical manner, and the solution satisfies the inhomogeneous wave equation.

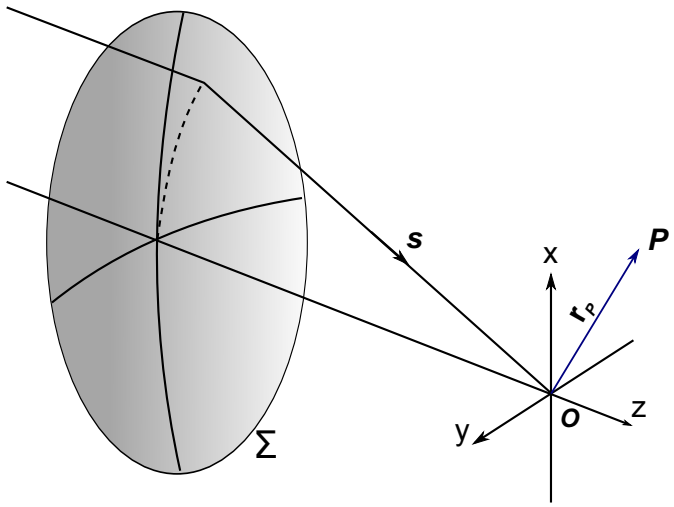

Figure 2.1: Diagram showing light focused by a lens into a single medium. A point source situated in the object space at $z = -\infty$ radiates a linearly polarized monochromatic and coherent electromagnetic wave. The propagation wave is then incident upon a lens of aperture Σ that produces a convergent spherical wave in the image space. The origin O of the (x, y, z) coordinate system is positioned at the Gaussian focus. The electric and magnetic fields are determined at the arbitrary point P within the focal region.

2.2.1 Debye-Wolf integral representation

We consider an optical system with a symmetric revolution with an optical z–axis as show in Fig. 2.1. This system images a point source that is situated in the object space at $z = -\infty$ and radiates a linearly polarized monochromatic and coherent electromagnetic wave. This wave is incident upon a lens of aperture Σ that produces a convergent spherical wave in the image space. The origin O of the (x, y, z) coordinate system is positioned at the Gaussian focus. The electric and magnetic fields are determined at the arbitrary point P from an aperture which was taken to be large as compared with the wavelength. In Fig. 2.1 and what follows, $\mathbf{s} = (s_x, s_y, s_z)$ is the unit vector along a typical ray in the image space and $\mathbf{r}_P = (x, y, z)$ is the position vector pointing from O to P. Let $\tilde{\mathbf{E}}(P, t)$ indicate the time-dependent electric field and $\tilde{\mathbf{H}}(P, t)$ indicate the time-dependent magnetic field at P at time t, so that

$$\tilde{\mathbf{E}}(P, t) = Re[\mathbf{E}(P) \exp(-i\omega t], \tag{2.1}$$

$$\tilde{\mathbf{H}}(P, t) = Re[\mathbf{H}(P) \exp(-i\omega t], \tag{2.2}$$

where Re indicates the *real* part.

In a homogeneous image space the time-independent electric and magnetic fields can be presented as a superposition of plane waves [53], and we use the form developed by Wolf [54]:

$$\mathbf{E}(P) = -\frac{ik}{2\pi} \iint_{\Omega} \frac{\mathbf{a}(s_x, s_y)}{s_z} \exp\left(ik[\Phi(s_x, s_y) + \mathbf{s} \cdot \mathbf{r}_p]\right) \, ds_x \, ds_y, \tag{2.3}$$

$$\mathbf{H}(P) = -\frac{ik}{2\pi} \iint_{\Omega} \frac{\mathbf{b}(s_x, s_y)}{s_z} \exp\left(ik[\Phi(s_x, s_y) + \mathbf{s} \cdot \mathbf{r}_p]\right) \, ds_x \, ds_y, \tag{2.4}$$

where $\Phi(s_x, s_y)$ is the aberration function (describing the optical path difference between the aberrated and the spherical wave front along $\mathbf{s}$, $\mathbf{a}$ and $\mathbf{b}$ are electric and magnetic strength vectors, respectively, of the unperturbed electric and magnetic fields in the exit aperture Σ, k is the wave number, and Ω is the solid angle formed by all the geometrical optics rays (and which is therefore a limit for all $\mathbf{s}$ unit ray vectors).

2.2.2 Extended Debye-Wolf integral representation

We note that Eqs.(2.3) and (2.4) represent a summation of the plane waves that are leaving the OL's aperture. In addition, the electric and magnetic fields do not depend on the particular wavefront within the solid angle Ω over which the integration is performed. This statement can be proved in a rigorous mathematical manner [88]. Equations (2.3) and (2.4) also show that the phase factor (apart from the aberration function) is a scalar product of the vectors $\mathbf{s}$ and $\mathbf{r}_p$. As a consequence, the phase factor expresses the optical path difference between wavefronts going through the point P and the Gaussian focus O, unlike Fresnel-Kirchhoff integral, for which the phase factor is proportional to the full path from aperture to P.

Our consideration is that, the image space of the OL consists of material 1 (lossless) and 2 (lossy) with refractive indices n_1 and $\tilde{n}_2 = n_2 + i\kappa$, respectively, which are separated by a planar interface perpendicular to the optical axis, as shown in Fig. 2.2. The origin O is positioned at the Gaussian focus. We reformulate Eq. (2.3) as follows.

In material 1 and at the interface ($z = -d$)) the incident electric field is given by

$$\mathbf{E_1}(x, y, -d) = -\frac{ik_1}{2\pi} \iint_{\Omega_1} \mathbf{W}^{(e)}(\mathbf{s}_1) \exp[ik_1(s_{1x}x + s_{1y}y - s_{1z}d)]\, ds_{1x}\, ds_{1y}, \quad (2.5)$$

where subscripts 1 (and 2 in what follows) denote values corresponding to regions in materials 1 (and 2), respectively, the OL is taken to be aberration free ($\Phi(s_{1x}, s_{1y}) = 0$), and

$$\mathbf{W}^{(e)} = \frac{\mathbf{a}(s_{1x}, s_{1y})}{s_{1z}}. \quad (2.6)$$

We shall not present the derivation of the formulas corresponding to the magnetic field because, apart from the strength vectors, Eq. (2.3) and Eq. (2.4) are of the same form.

To describe the field in the second material, we assume that each plane wave component refracting at the interface obeys the complex Snell's law, and the resulting field is constructed as a superposition of refracted plane waves. If the amplitude of the plane waves incident upon interface is described by $\mathbf{W}^{(e)}$, then the amplitude of

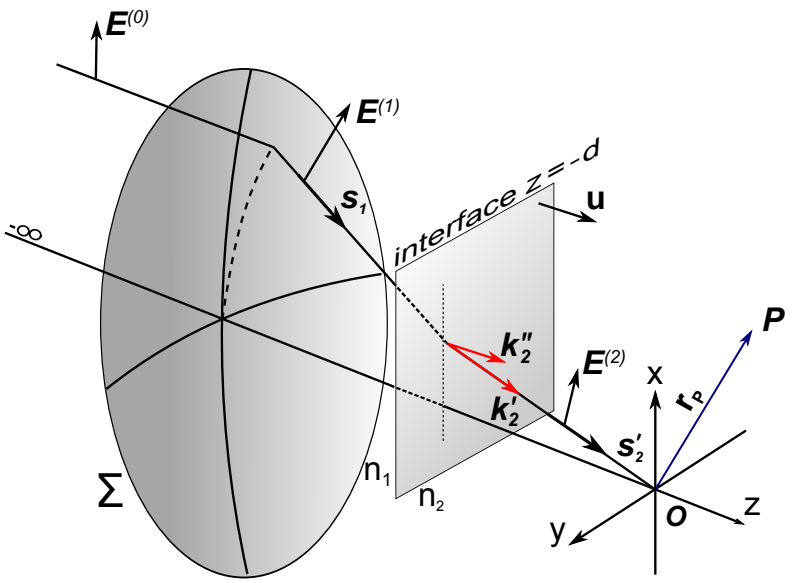

Figure 2.2: Diagram showing light focused by a lens into two media separated by a planar interface.

the transmitted plane waves in the second material is a linear function of $\mathbf{W}^{(e)}$, i.e.

$$\mathbf{T}^{(2)}\mathbf{W}^{(e)}, \tag{2.7}$$

where operator $\mathbf{T}^{(2)}$ is a complex function of the incidence angle, and of n_1 and $\tilde{n}_2$. The transmitted field in the second material at close vicinity ($z = -d + \delta$) of the interface is given by

$$\mathbf{E}_2(x, y, -d) = -\frac{ik_1}{2\pi} \iint_{\Omega_1} \mathbf{T}^{(2)}\mathbf{W}^{(e)}(\mathbf{s}_1) \exp[ik_1(s_{1x}x + s_{1y}y - s_{1z}d)]\, ds_{1x}\, ds_{1y}, \tag{2.8}$$

when $\delta \to 0$. We present the field inside the second material again as a superposition of plane waves. In the second material, the wavenumber vector $\mathbf{k}_2$ has a complex vector representation, *i.e.* $\mathbf{k}_2 = \mathbf{k}_2' + i\mathbf{k}_2''$, where $\mathbf{k}_2'$ and $\mathbf{k}_2''$ are real vectors. Each vector has its own direction of propagation which is characterized by the unit vector $\mathbf{s}_2'$ and $\mathbf{s}_2''$, respectively. In Appendix A.2 we shows that $\mathbf{k}_2''$ is always perpendicular to the interface, hence the integration in Eq. (2.8) depends only on the orientation of $\mathbf{k}_2'$, hence $\mathbf{s}_2'$. Now we can express the complex vector in the second medium as $\mathbf{k_2} = \mathbf{k}_2' + i\mathbf{k}_2'' = k_2'\mathbf{s}_2' + ik_2''\mathbf{s}_2''$ where $\mathbf{k}_2'$ and $\mathbf{k}_2''$ are defined by $|\mathbf{k}_2'| = \frac{\omega}{c_0}m'$ and $|\mathbf{k}_2''| = \frac{\omega}{c_0}m''$ with m' and m'' is defined by Eq. (A.15a)-(A.15b) in Appendix A.2. The

time-independent wave equation in the second medium can now be written as

$$\begin{aligned}\mathbf{E}_2(\mathbf{r}_p) &= \iint_{\Omega_2} \mathbf{F}^{(e)}(\mathbf{s}_2') \exp(i(\mathbf{k_2} \cdot \mathbf{r}_p)\, ds_{2x}'\, ds_{2y}', \\ &= \iint_{\Omega_2} \mathbf{F}^{(e)}(\mathbf{s}_2') \exp[i(k_2'\mathbf{s}_2' \cdot \mathbf{r}_p)] \exp(-k_2'' z)\, ds_{2x}'\, ds_{2y}'. \end{aligned} \tag{2.9}$$

We must determine the function $\mathbf{F}^{(e)}(\mathbf{s}_2')$, and for this we shall make use of Eq. (2.8), which represents a boundary condition for Eq. (2.9). Furthermore, we shall establish the relationship between $\mathbf{s_1}$ and $\mathbf{s}_2'$.

From the vectorial law of reflection we have,

$$k_2'\mathbf{s}_2' - k_1\mathbf{s}_1 = (k_2' \cos\phi_2 - k_1 \cos\phi_1)\mathbf{u}, \tag{2.10}$$

where $\mathbf{u}$ represents the normal to the interface, $\phi_1 = (\mathbf{s}_1, \mathbf{u})$ and $\phi_2 = (\mathbf{s}_2', \mathbf{u})$, that

$$k_2' s_{2x}' = k_1 s_{1x}, \quad k_2' s_{2y}' = k_1 s_{1y}. \tag{2.11}$$

As a result of a coordinate transformation and setting $\mathbf{s}_2' = f(\mathbf{s}_1)$, Eq. (2.9) becomes

$$\begin{aligned}\mathbf{E}_2(\mathbf{r}_p) = \iint_{\Omega_1} &\mathbf{F}^{(e)}(\mathbf{s}_2') \exp(ik_2'\mathbf{s}_2' \cdot \mathbf{r}_p) \exp(-k_2'' z) \\ &\times \mathbf{J}_0(s_{1x}, s_{1y}; s_{2x}, s_{2y})\, ds_{1x}\, ds_{1y}, \end{aligned} \tag{2.12}$$

where $\mathbf{J}_0$ is the Jacobian of the coordinate transformation :

$$\mathbf{J}_0 = \left(\frac{k_1}{k_2'}\right)^2$$

obtained by the use of Eqs. (2.11). Equation (2.12) satisfies the boundary condition represented by Eq. (2.8) when

$$\mathbf{F}^{(e)}(\mathbf{s}_1, \mathbf{s}_2) = \left(\frac{i{k_2'}^2}{2\pi k_1}\right) \mathbf{T}^{(e)} \frac{\mathbf{a}(s_{1x}, s_{1y})}{s_{1z}} \exp[-id(k_1 s_{1z} - k_2' s_{2z}')] \exp(-k_2'' d), \tag{2.13}$$

Substituting Eq. (2.13) into Eq. (2.12), we obtain the electric field in the second material:

$$\begin{aligned}\mathbf{E}_2(x, y, z) = -\frac{i}{2\pi k_1} \iint_{\Omega_1} &\mathbf{T}^{(e)} \mathbf{a}(s_{1x}, s_{1y}) \frac{{k_2'}^2}{s_{1z}} \exp[-id(k_1 s_{1z} - k_2' s_{2z}')] \\ &\times \exp(ik_2' s_{2z}' z) \exp[ik_1(s_{1x}x + s_{1y}y)] \\ &\times \exp[(-k_2''(z+d)]\, ds_{1x}\, ds_{1y}. \end{aligned} \tag{2.14}$$

It is important to emphasize that, since both the boundary condition represented by Eq. (2.8), and the integral representation from Eq. (2.9) are exact solutions of the homogeneous and inhomogeneous wave equations. Therefore we have successfully obtained a consistent extension of Wolf's solution in the second material.

In order to perform the numerical calculation of the diffraction integral in Eq. (2.14), we need to define an explicit form of the electric strength vector $\mathbf{T}^{(e)}$. This term is defined in Appendix **??**.

2.3 Numerical results

We performed numerical computations by using our diffraction integrals of Eq. (2.14) to determine the electric energy density distributions occurring when a hight NA OL that obeys Abbe's sine condition is used. The incident illumination is assumed to be linearly polarized along the lateral x–axis of the Cartesian coordinate. It should be noted that for a high NA OL (NA>1) it is necessary to immerse the lens in oil or in water in combination with a microscope coverslip. If a glass is used as a coverslip, the use of a glass-like materials as an immersion medium is necessary for refractive index matching. In an optical microscope and DLW, oil is preferable. Glass and oil have the same refractive index, which is about 1.51, so they can be considered as an unique medium. For simplifying, we merely use the short term *glass* instead of *glass+oil* for indicating the first medium. The numerical result for a glass-air system (air OL) has been shown by Török in Ref. [65], in this thesis we focus on a glass-photoresist system (with use of high NA oil immersion OL). This configuration is important in material science, especially in direct laser writing when light is focused into a photoresist layer through a oil and glass medium. In what follows, we calculate the time-averaged electric energy density distribution at observation points. The time-averaged electric energy density distribution is written as:

$$\langle w_e(r_p, z, \phi_p)\rangle = \frac{n^2\epsilon_0}{2}(\mathbf{E}\cdot\mathbf{E}^*)$$

where n is the refractive index, c is the speed of light in vacuum, ϵ_0 is the vacuum permittivity and $\mathbf{E}$ and $\mathbf{E}^*$ denote the electric field and its complex conjugate, which are defined by Eqs. (2.14), after noting the modifications as shown in Appendix **??**.

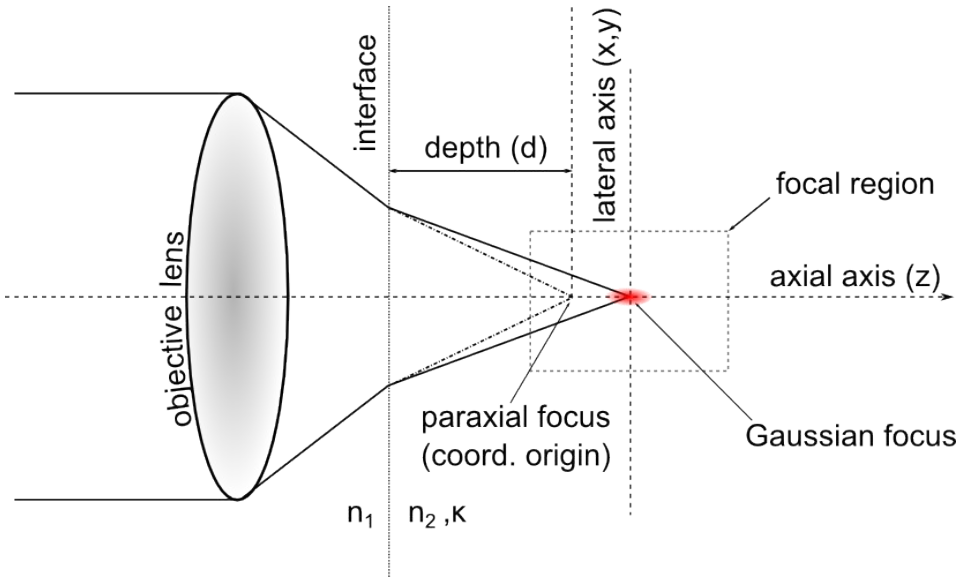

Figure 2.3: Illustration of a laser beam focused in stratified media and different notations used in numerical calculation.

The intensity is obtained by multiplying the expression of time-averaged electric energy density distribution by the velocity of the wave, c/n, it can be expressed as

$$I = \frac{cn\epsilon_0}{2}(\mathbf{E} \cdot \mathbf{E}^*).$$

In this work, the integral formula are programmed by a personal code script based on the Matlab software. Some details of the script are presented in Appendix B. This allows us to numerically study the intensity distribution at the focal region of a high NA OL as a function of different experimental conditions. For reason of unique definition, we predefine our physical parameters as following (also see Fig. 2.3).

- The time-averaged electric energy density distribution is time-averaged of electric energy density, which refers to the amount of energy stored in a region of space per unit volume. For convenient, sometimes we use the short term *electric energy density* instead.

- The term *paraxial focus* refers to a mathematical point where the focusing point is located if the optical system is aberration-free (ideal case). In this case, obviously, the Gaussian focus coincides with the paraxial focus.

- The term *depth* refers to the depth below the interface where the paraxial focus is located.
- The term *axial direction* refers to the positive or negative direction parallel to the optical axis (z–axis).
- The term *lateral direction* refers to the direction perpendicular to the optical axis.
- The term *main maximum* refers to the maximum of the time-averaged electric energy density distribution at the focus.
- The term *subsidiary maximum* refers to the maximum value of time-averaged electric energy density distribution at near focus within the focal region.
- The term *global maximum* is the highest value of time-averaged electric energy density distribution within the entire region of interest; there can only be one global maximum.
- The term *global minimum* is the lowest value of the time-averaged electric energy density distribution within the entire region of interest; there can only be one global minimum.
- The term *global maximum* can be coincided with the main as well as the subsidiary maximum.
- The term *focus shift* refers to amount of shift from the paraxial focus of the main maximum (when the electric energy density maximum's position no longer coincide with the paraxial focus due to spherical aberration).
- The term *axial size* and *lateral size* respectively refer to the full width at half maximum of the focusing spot along the axial and lateral directions where the intensity is measured. The short term FWHMs is used to denote both axial and lateral sizes.

We also assume that the OL is aberration-free and we only consider the spherical aberration due to the MRI of media in the image space. The reason is that modern

high-performance lenses are generally well corrected for spherical aberration. Therefore, when considering a real optical system, the assumption of a perfect spherical wave emerging from the lens and converging toward the Gaussian focus point.

2.3.1 Lossless media

In this section, all numerical computations were performed for a wavelength of λ=532 nm. First we studied the structure of the electromagnetic field distribution at the focal region of an oil-immersion lens. In this case calculations were performed for NA=1.15, NA=1.3 and NA=1.45 and refractive indices are $n_1 = 1.51$ and $n_2 = 1.58$ for the first and second material, respectively. We notice that although the electric energy density values are given in arbitrary units, all values correspond to a constant incident beam energy, and so the energies in all the figures in this section can be directly compared.

In Figs. 2.4 electric energy densities are shown in the (xz)–plane for a numerical aperture of (a) NA=1.15, (b) NA=1.3 and (c) NA=1.45, corresponding to solid semi-angles in glass of 49.6°, 59.4° and 73.8°, respectively, those in photoresist are of 46.7°, 55.4° and 66.6°, respectively. Field at the depth of 5 μm is measured and the electric energy density contours are plotted on a logarithmic scale. The results show how the diffraction pattern is formed at the focal region. The diffraction pattern is distributed to many subsidiary maxima and subsidiary minima, which are represented by iso-energy curves. Different colors corresponding to different iso-energies are referenced to color bars. For NA=1.15 the electric energy density is closely symmetrical about the focal plane. For NA=1.3 it is slightly asymmetrical, this asymmetry being more pronounced with the lateral subsidiary maxima. For NA=1.45 the distribution is asymmetrical, the axial maxima being more pronounced in the positive z–axis direction and the lateral maxima being displaced in the positive z–axis direction. The lateral and axial sizes of the main maximum are substantially decreased with respect to those corresponding to NA=1.15 and NA=1.3. Along the negative axial direction, local maxima become smaller and local minima become larger; thus the modulation of subsidiary peaks at the negative axial direction becomes less pronounced compared with that at the positive axial direction. The innermost iso-energy density at the

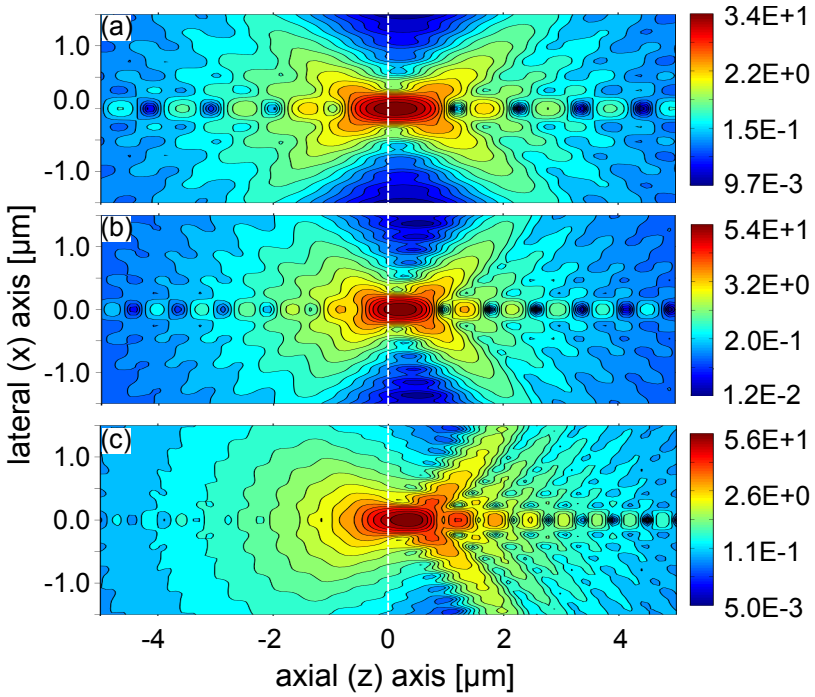

Figure 2.4: The time-averaged electric energy density distribution in the (xz) meridional plane for (a) NA=1.5, (b) NA=1.3 and (c) NA=1.45 at a depth of d=5 μm. Calculation for glass ($n_1 = 1.51$) and photoresist ($n_2 = 1.58$) and a wavelength of λ=532 nm.

center of each pattern generally appears as an ellipsoid which indicates the maxima electric energy density of the focal region. The axial and lateral sizes of this volume reduces when going from –(a) to –(c). On going from the NA=1.15 to NA=1.3, the electric energy density for the axial maximum increases by $\approx 1.6\times$, and on going from NA=1.15 to NA=1.45, it increases by $\approx 1.65\times$. We expected large increments, but in fact, they are quite modest. The reason is that, as NA increases, the initial symmetrical pattern is progressively replaced by an asymmetrical one about the focal plane. As a result, the iso-energy density volume is increased and slow down the acceleration of the maxima electric energy density. The axial position of the maxima electric energy density move forwards to the positive direction as NA increases. This indicates that the focus shift increases as a function of the NA. In this configuration, the focus shift is small. We calculated the time-averaged electric energy density for a numerical aperture of NA=1.3 and for focus depths of (a) d=5, (b) d=10, (c) d=20, (d) d=40, (e) d=80 and (f) d=160 μm. Figure 2.5 shows the results obtained with

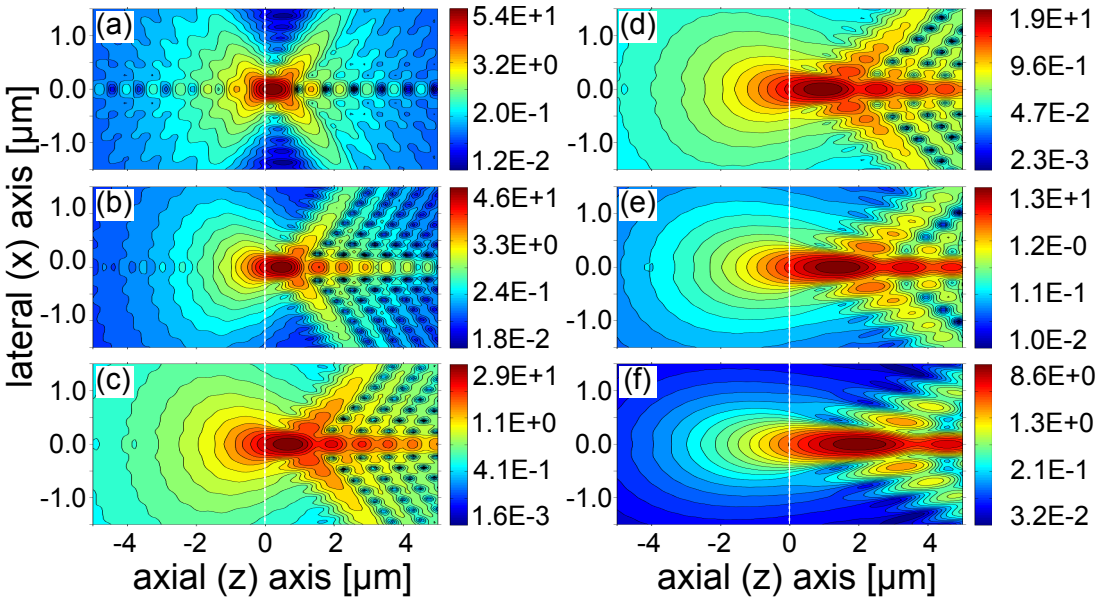

Figure 2.5: Time-averaged electric energy density distribution in the (xz)–meridional plane for NA=1.3 and depths of (a) d=5, (b) d=10, (c) d=20, (d) d=40, (e) d=80 and (f) d=160 μm. Calculations for glass ($n_1 = 1.5$) and photoresist ($n_2 = 1.58$) at a wavelength of λ=532 nm.

NA=1.3. The results show that, on going from a depth of d=10 μm to d=160 μm, the electric energy density becomes less concentrated as depth increases. The main maximum the electric energy density decreases by $\approx 4\times$ (results not shown), $\approx 6.5\times$ (results not shown) and $\approx 8.2\times$ for NA=1.15, NA=1.3 and NA=1.45 respectively. We usually believe that the main maximum of the electric density is large at higher NAs compared with the lower ones, but this statement must be carefully used when MRI is large. This problem is discussed in more detail in the next example. The lateral and axial sizes become smaller at higher NAs and becomes larger when increasing the focus depth. Only ≈ 2 μm of the focus shift is observed at a depth d=160 μm.

Now we examine the following parameters: intensity, focus shift, and lateral (x) and axial (z) sizes of the focus. It is important to describe the algorithm by which we computed the axial and lateral sizes. First, intensity versus distance along the optical z–axis axis was calculated, and the z value for the intensity maximum was determined. Second, this curve was shifted to the negative electric energy density direction by half of its maximum value. Third, the first roots along the positive and negative z–axis directions were determined, and the distance between them gave the axial size. The

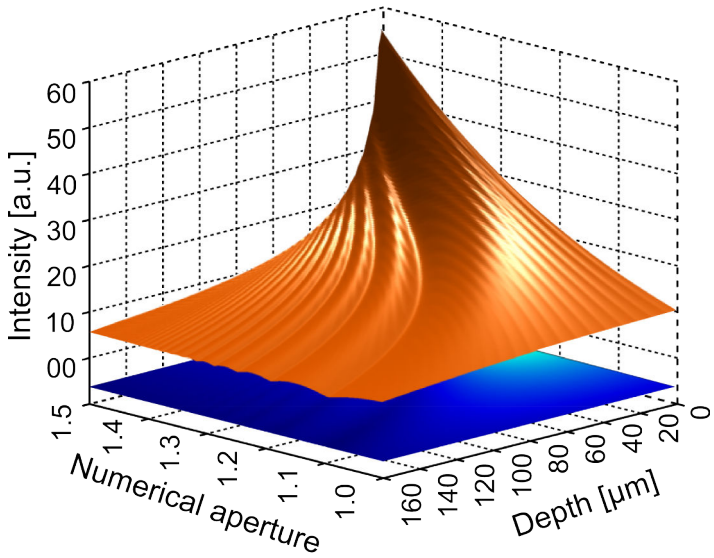

Figure 2.6: (a) Maximum intensity (at the focus) as a function of numerical aperture and depth. Calculated for glass ($n_1 = 1.51$)–photoresist ($n_2 = 1.58$) interface.

same procedure was repeated for the lateral distribution. The algorithm was done by using a custommade-FWHM Matlab function.

In Fig. 2.6, the intensity is shown as a function of NA and focus depth. The lower panel shows a painter plot, which is a projection of the plot in a plane parallel to the (xy)–plane of the Cartesian coordinate. We can see that, for low NAs the intensity does not much vary and remains low regardless of the depth. As NA increases, the intensity increases and varies approximately inversely proportional to the depth. When NA exceeds 1.1, the dependence of the function on the depth becomes nonlinear but remains monotonic. At NA=1.1, the function is no longer monotonic. Many orders of irregularity occurs at NA in the range 1.1-1.5. It is interesting that, the intensity decreases smoothly at high NAs as depth increases. This can be seen clearly for NA=1.5 where no irregularities are observed. In this case the intensity decreases monotonically when increasing depth. A smoothing effect can be observed on the function when NA and depth are large. It can thus be concluded that the three-dimensional distribution of the electric intensity behave in a regular as well as in non-regular manner within the calculated region. When working with a well-defined NA one should pay attention at which depth the nonlinearity behavior occurs.

In Figs. (2.7) the focus shift is plotted as a function of NA and depth. Like for

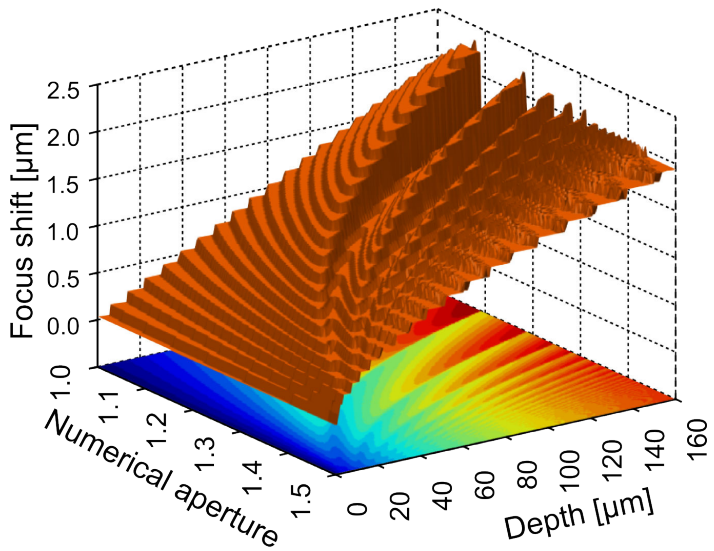

Figure 2.7: Focus shift as a function of NA and depth.

electric intensity, the focus shift shows linear then nonlinear behaviors as a function of NA and depth. The linear regime is observed when NA approximately exceeds 1.15. When NA > 1.15, the dependence of the focus shift on the depth becomes a nonlinear but monotonic function. The maximum of the focus shift observed in this system is $\approx 2,5$ μm, at NA=1.1 and for a depth d=160 μm, the step-like behavior of the focus shift due to the nonlinearity varies as a function of both NA and depth is more complicated. In our investigation each jump-step is about 100 nm long.

In Figs. 2.8–(a) and Figs. 2.8–(b), the lateral (x) and axial (z) sizes, respectively, are plotted as functions of both NA and depth. The calculation was performed for NA ranging from 1.0 to 1.5 and depth ranging from 0 to 150 μm. The same trend of variation as in the low NA case [89] is observed here, both the lateral and the axial size change linearly when NA<1.1 and nonlinearly when NA>1.1. FWHMs start to change nonlinearly at a depth of about 30 μm and NA = 1.1. Outside this region, the FWHMs become nonmonotonic. Maximum lateral and the axial sizes observed in this case are 0.362 μm and 3.996 μm for NA=1.1 and d=160 μm, respectively. Interestingly, the lateral size increases very quickly at these value resulting in a sharp peak in Figs. 2.8–(b). Although the nonlinearity exists, when NA is larger than 1.2, the lateral size changes monotonically but the change is very small. All plots in –(a)

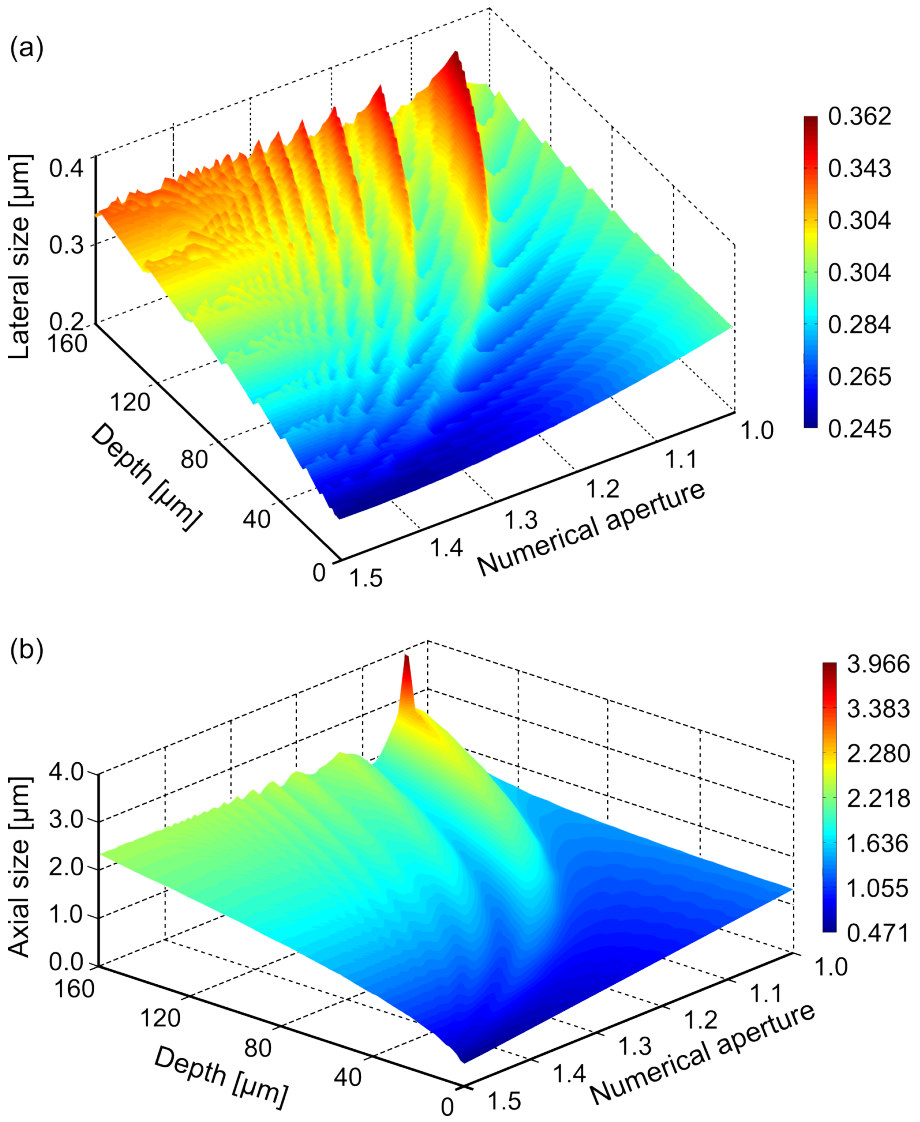

Figure 2.8: (a) Lateral and (b) axial size of the focusing spot as a function of NA and depth. For a depth d<30 μm, a linear behavior dominates. The nonlinearity makes the focusing spot size to monotonically vary when NA<1.1 and nonmonotonic only when NA>1.1. The well-defined linear region is limited by (d<30 μm and NA<1.1), elsewhere the nonlinearity predominates.

and –(b) exhibit a similar trend, leading to a well-defined region within the computed range of NA and depth where the FWHMs behave in a monotonic manner and another region where they become nonmonotonic. Because of nonlinearity, working at a depth larger than 30 μm is not recommended in the case of large spherical aberration.

Important conclusions can be drawn from the above numerical results for the

lossless case. All results consistently predict a regular behavior (monotonic regions) and an irregular behavior (nonmonotonic regions) of intensity, focus shift, and FWHMs. The explanation of this unusual behavior is as follows. For small depths, the axial distribution of the electric energy density is only slightly asymmetric around the maximum. As depth increases, the spherical aberration introduced by the MRI medium increases, and the axial distribution becomes more asymmetric. When increasing depth, this strong degree of asymmetry induces a secondary maximum located close to the main maximum. The distortion increases, and the main maximum decreases, as a result of an increasing spherical aberration. The negative side distortion increases sufficiently with electric energy density to it become equal to the original maximum, which results in a widening of the distribution. These results show that when the effect of spherical aberration is taken into account, it is essential to consider the presence of the developing secondary maxima. In microscopy as well as in DLW with high NA lenses, MRI is usually encountered, the secondary maxima is the main factor which obstruct to get high resolution. In DLW, especially operating in one-photon absorption mechanism, when the secondary maxima is dominant as compared with the original maximum, high dimensional structures are impossible to be fabricated.

2.3.2 Lossy media

We have numerically evaluated the convolution of the focused electromagnetic wave in a lossless medium. All results suggest that, although light is not absorbed by the material, the maximum intensity is reduced when increasing the focus depth. Now we consider a general system where the second material is considered to be lossy. In such a medium, light is continuously absorbed. The mathematical term ${k_2'}^2 \times \exp\left[-k_2''(z+d))\right]$ in Eq. (2.14) expresses the exponential decay factor of the electric field amplitude. It is worth to note that this term depends on the wave vectors k_2' and k_2'', on the depth of the focus d with respect to the interface and z–axis coordinate of the observation point. Generally, the effective refractive index is not a constant. It depends on: (i) the refractive indices of the first and second medium n_1 and n_2; (ii) the extinction coefficient κ; and (iii) the refraction angle

ϕ_2 of each individual plane wave that strikes the interface. Such angle-dependent effective refractive index to change the attenuation coefficient every moment during numerical integration. The materials which possess high extinction coefficients (strong absorption) and low extinction coefficients (weak absorption) are easy to be found among a wide range of photoresists. In direct laser writing, there are three common types of photoresist, namely SU-8, AZ® series and EPON resins. The extinction coefficient of these photoresist vary depending on the applied wavelength. For sake of comparison and simplification, in this section, we shall not consider the change of refractive index with respect to the applied wavelength. Indeed, the refractive index of the first (glass) and second medium (photoresist) are merely chosen to be $n_1 = 1.51$ and $n_2 = 1.58$ respectively. In all cases, an aberration-free OL with NA=1.3 is used. We will examine three examples. In the first example we examine the structure of the electromagnetic wave, especially in the intensity at the focus, with different extinction coefficients. In the second example we study the structure of the electromagnetic wave in both axial and lateral directions, especially the main maximum intensity at the focus for different depths from the interface. In the third example, we investigate the maximum intensity as a function of both NA of the lens and the depth d. In the two first examples, a single wavelength λ=532 nm is considered.

In Fig. 2.9 the intensity is plotted in the (xz)–meridional plane for extinction coefficients of (a) $\kappa = 0.05$, (b) $\kappa = 0.0059014$, (c) $\kappa = 0.0009004$ and (d) $\kappa = 0.0000306$. In all subfigures, the glass-photoresist interface is located at $z = -40$ μm. For comparison, the extinction coefficients are chosen in a broad absorption range. The absorption coefficients taken in this example correspond to those of common photoresists used in DLW. Indeed, the extinction coefficient in Fig. 2.9–(a) can be found in AZ 1500 photoresist at the wavelength of 0.405 μm, and those in Fig. 2.9–(b)-(d) correspond to SU-8 photoresist at λ=308 nm, λ=365 nm and λ=532 nm, respectively. However, as supposed, we simplify the problem by considering only a single wavelength of λ=532 nm for all different extinction coefficients. Figure 2.9–(a) shows that due to a high absorption coefficient, the electromagnetic wave incident on the interface rapidly decays in the second medium just after the interface. Some light can penetrate far in photoresist to reach the focus but does not reach geometrical spot (focusing spot). In this case the global maximum is located near the interface.

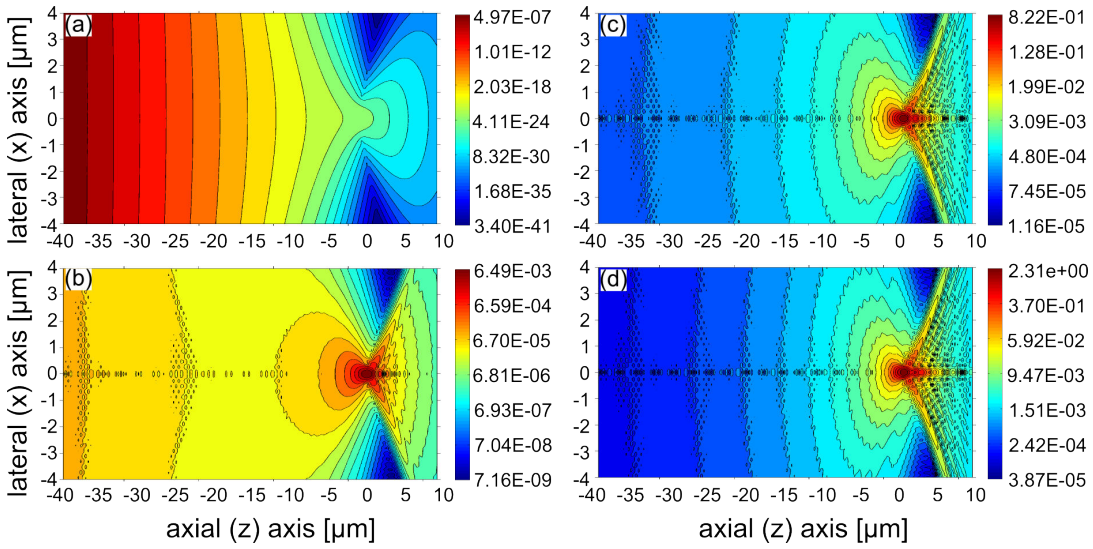

Figure 2.9: Time-averaged electric energy density distribution in a meridional (xz)–plane. Calculation are made for a depth of 40 μm and an extinction coefficient of (a) $\kappa = 0.05$, (b) $\kappa = 0.0059014$, (c) $\kappa = 0.0009004$ and (d) $\kappa = 0.0000306$.

On going from the interface to the paraxial focus the electric energy density drops by $\approx 10^{15}$. The local maximum drops $1/e$ times after traveling just ≈ 1 μm from the interface, this length is well-known under the name *penetration depth*. As long as the plane of constant amplitude is parallel to the interface, the penetration depth can be dictated by Beer-Lambert's law. In this case the calculated penetration depth is ≈ 0.85 μm.

In Fig.2.9–(b), the extinction coefficient $\kappa = 0.0059014$ is nearly ten times smaller in comparison to that in Fig.2.9–(a), electromagnetic wave penetrates deeper in the photoresist resulting in a geometrical focusing spot. The subsidiary maxima start to appear along the positive direction and the energy distribution is more concentrated on the opposite side. The iso-energy density curves tend to bound the focus. Although the global maxima migrate from the near-interface to the focal region, producing a perceivable focusing spot, most of light is absorbed along propagation.

In Fig. 2.9–(c), when the extinction coefficient becomes sufficiently small, $\kappa = 0.0009004$, the electric energy density at the focusing spot is much improved. The energy distribution is more concentrated. Diffraction pattern appears clearly. The electric energy density near the interface is three order of magnitude smaller than that

in Fig. 2.9–(b). The electric energy density at the focus slightly increase. Near the focus the energy density increases faster outwardly from the main maximum focus.

Decreasing further the extinction coefficient by about thirty times, $\kappa = 0.0000306$, (see In Fig.2.9–(d)), the main maximum increases by $2.8\times$ and the global minima increases by $3.5\times$ in comparison to that in Fig. 2.9–(c).

As compare to the case with no absorption, the main maximum reaches $\approx 0\%$ for $\kappa = 0.05$, $\approx 0.27\%$ for $\kappa = 0.0059014$, $\approx 34.3\%$ for $\kappa = 0.0009004$ and $\approx 96,1\%$ for $\kappa = 0.0000306$. As expected, the energy is more concentrated at the focusing spot when decreasing the absorption coefficient. The case of $\kappa = 0.0000306$ can be considered a nearly transparent case. In such a case, the form, shape and intensity of the focusing spot are closely identical to those without absorption case.

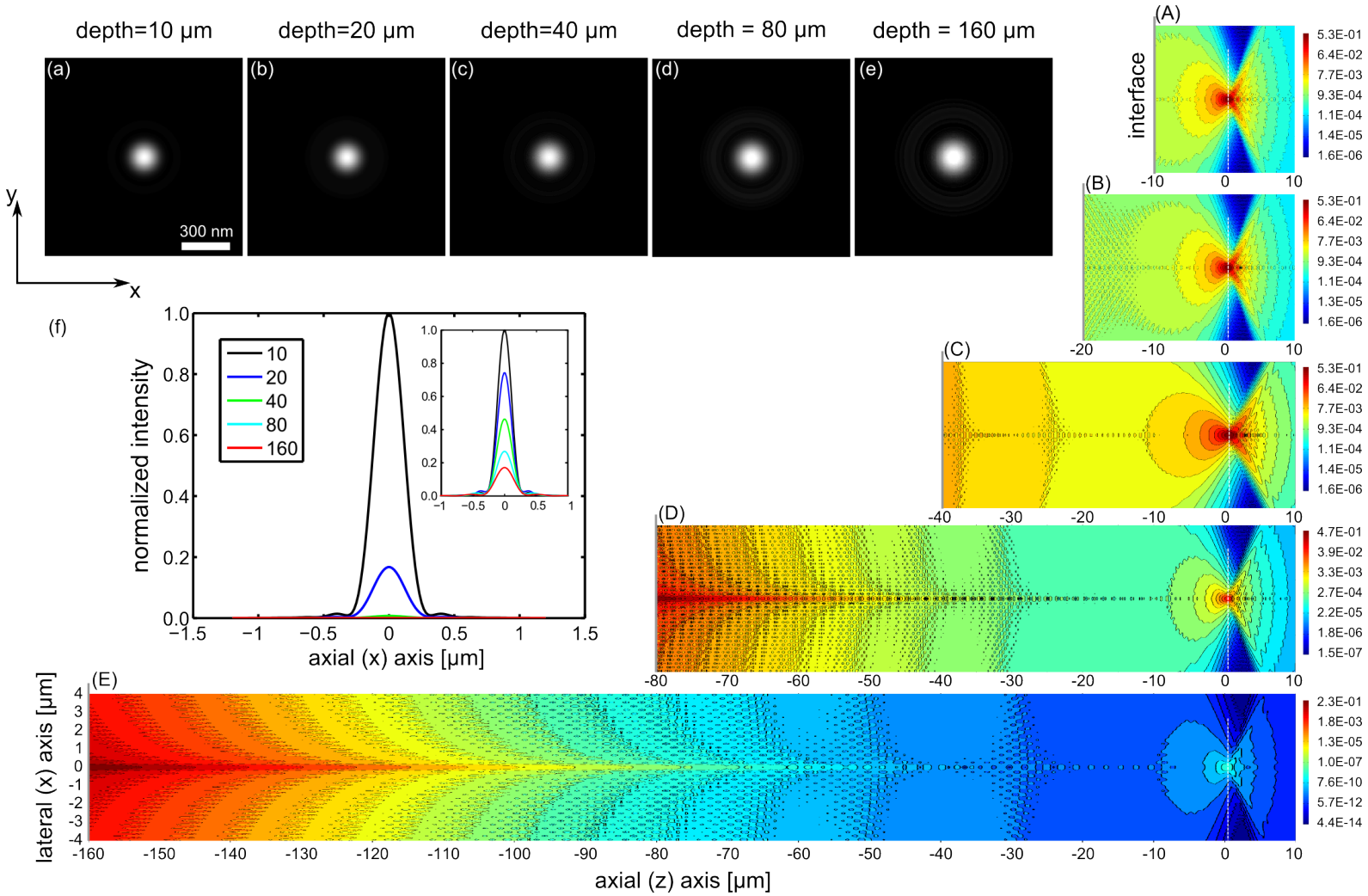

Figure 2.10: Time-averaged electric energy density distribution is plotted in the (xz)–plane for depths of (A) d=10, (B) d=20, (C) d=40, (D) d=80 and (E) d=160 μm. The correspond energy density distribution in the (xy)–plane are plotted in –(a)-(e). Intensity distribution across the focal point of each case are plotted together in –(f). Calculation are made for an extinction coefficient of $\kappa = 0.0059014$, NA=1.3, and a green light laser wavelength λ=532 nm. For comparison, inset in subfigure –(f) the normalized intensity is plotted for the case without absorption ($\kappa = 0$).

Now we examine the electromagnetic diffraction pattern at different focus depths from the interface. In this study, the extinction coefficient is taken to be $\kappa = 0.0059014$; other parameters of the system are unchanged. In Fig. 2.10 the averaged-energy density is plotted in the (xz)–meridional plane for depths of (A) d=10, (B) d=20, (C) d=40, (D) d=80 and (E) d=160 μm. The interface is on the left-hand side of each panel. The lateral coordinate is $[-4 + 4]$ as indicated in (E), which is the same as in (A)-(D). The axial coordinate varies corresponding to each case.

When going from d=10 μm to d=160 μm, the main maximum decreases. The global maxima at a depth larger than d=80 μm do not longer coincide with the main maxima, but are located at near interface. The focus shift is larger at higher depths. From (A) to (E) these are 0.32, 0.67, 0.83, 1.05 and 1.22 μm. As compare to the lossless case, the main maximum is slightly shifted toward the negative direction. This indicates that, not only the intensity is altered by absorption but also the focus shift. The latter is less pronounced than that of the corresponding lossless case.

In Figs. 2.10–(a)-(e), a slice across the main maximum perpendicular to the optical axis is plotted in the (xy)–plane for each case corresponding to –(A)-(E). The scale bar in –(a) is 0.3 μm, the same scale holds for –(b)-(e). When going from d=10 μm to d=160 μm, the lateral size of the main maximum increases and the maximum intensity decreases. This indicates that the energy distribution is less concentrated when increasing the depth. The intensity at the main maximum is plotted in –(f). In this figure, intensities are normalized to the maximum intensity of the focus for a depth d = 10 μm. As depth increases, the maximum intensity drops rapidly. Indeed, when going from a depth d = 10 μm to d = 20 μm, the intensity deceases by about 5×. The maximum intensity continues to decrease by three, five and six orders of magnitude for depths of 40 μm, 80 μm and 160 μm, respectively. For comparison, the normalized intensities at the same depths are plotted together in the inset for Fig 2.10–(f) for the case with no absorption.

In Fig. 2.11 the maximum intensity (left) and focus shift (right) are plotted as a function of NA and focus depth. Calculations are made for SU-8 photoresist with extinction coefficients κ corresponding to (a) λ=308 nm; $\kappa = 0.0059014$, (b) λ=365 nm; $\kappa = 0.0009004$, and (c) λ=532 nm; $\kappa = 0.0000306$.

On the left column of Fig. 2.11 the maximum intensity is plotted as a function of

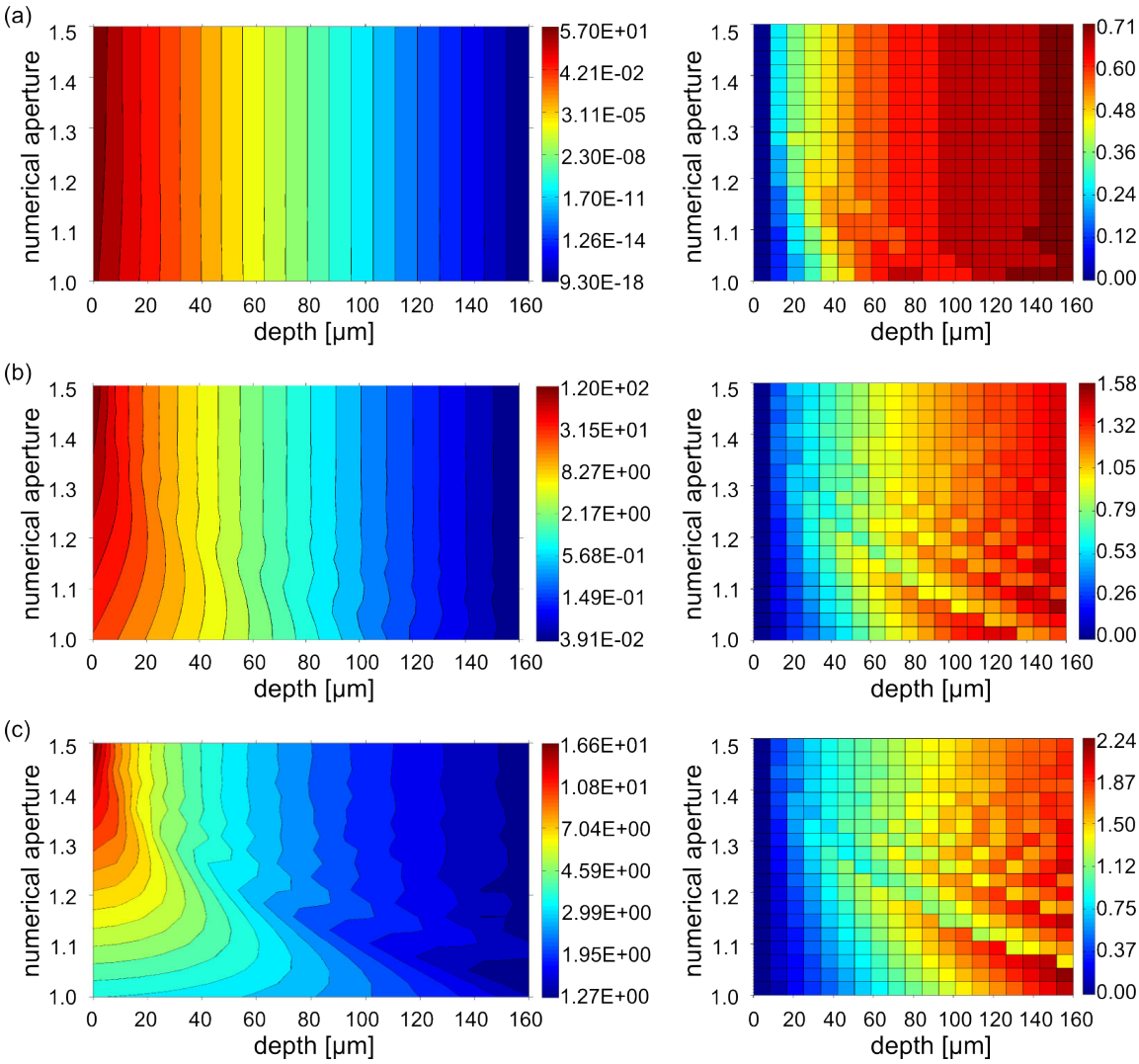

Figure 2.11: Maximum intensity (left) and focus shift (right) are plotted as a function of NA and depth for SU-8. Calculations are made for extinction coefficients κ corresponding to (a) λ=308 nm, $\kappa = 0.0059014$, (b) λ=365 nm, $\kappa = 0.0009014$, (c) λ=532 nm, $\kappa = 0.0000306$.

the numerical aperture and the focus depth. In –(a), we can see a little influence of the NA when going from NA=1.0 to NA=1.5. Most of the coming light is absorbed near the interface because of the absorption in this case is really strong. In –(b), the influence of NA starts to appear. At a depth smaller than 20 μm, the higher NA of the lens provides higher concentration of energy at the focus. For example, the maximum intensity at the focus of NA=1.5 for a depth d=20 μm is as high as that for NA=1.0 at the interface. The nonlinear behavior starts appearing at NA=1.3 and

for a depth of 20 μm. The nonlinearity propagates towards lower value of NA when increasing the focus depth. The situation is more clear in –(c) in which the absorption is sufficiently small. In such a case the influence of NA on the electric energy density at the focus is easier to visualize, as well as the nonlinearity. Interestingly, on going from the interface, the maximum intensity produced by a high NA is attenuated more quickly than in the case of low NA. For instance, the maximum intensity for NA=1.4 and a depth of d=40 μm is the same as for NA=1.1, at a depth d=60 μm.

On the right column of Fig. 2.11 the focus shift is plotted as a function of numerical aperture and focus depth. The color bar is represented in the micrometer scale. The influence of the absorption on the focus shift with respect to the paraxial focus is evident. Indeed, the focus shift in the case of –(a) is quite small as compared to that of –(b) and –(c).

A conclusion can be draw from results of this section, we can see that SU-8 is nearly transparent at wavelength of λ=532 nm, the photoresist exhibits extremely weak absorption. In this case, behaviors of the maxima intensity, focus shift as well as many other aspects are mostly identical to the lossless case.

2.4 Conclusions and perspectives

We have obtained a formulation for the diffraction occurring when light is focused by an aplanatic lens through a planar interface between a lossless and a lossy material. In our formalism, the MRI and the attenuation factor are treated in a rigorous mathematical manner. In our numerical calculations, time-averaged electric energy density distributions in the region of the focusing spot ware evaluated for a glass-photoresist interface with high NA OLs. The consistent results were obtained for two general cases: with and without absorption. In the first case, we examined the structure of the diffraction pattern at the focal region at different NAs and at different focus depths. The result shows that as NA of the lens increases, the time-averaged electric energy density distribution increases and the size of the main maximum decreases. In general, if either the NA or the focus depth decreases, the focus shift of the main maximum increases and the energy distribution becomes asymmetric, with the axial and lateral maxima moving in the positive z direction. Quantitative

data for the electric energy densities, sizes, and positions of the energy maxima were obtained. In the second case we focused on the intensity distribution in the entire calculation domain to highlight the effect of absorption. We paid our special attention to the distribution of electric energy at the focus by calculating of the maximum intensity as a function of numerical aperture and focus depth. The result shows that, as the extinction coefficient increases, the main maxima at a given depth decreases accordingly, light after passing through the interface is mostly absorbed by the material and, very little light can reach the Gaussian focus. Conversely, as the extinction coefficient decreases, the focused light can penetrate deeper, the maximum intensity at the focus increases and the electric energy density becomes more concentrated. Hence, the electric energy density of the focusing spot becomes denser, shaper in both size and shape (lateral and axial size decreases). In DLW, when moving the focusing point within a photoresist, and since polymerization is dominant at higher intensity points, it is not possible to obtain a good result if the focusing spot is deformed or if intensity distribution is not high enough. This issue will be treated in the next chapter.

Chapter 3

Realization of photonic structure by UV light-based direct laser writing

In the previous chapter we have theoretically investigated the structure of electromagnetic waves propagating in an absorbing medium through a planar interface. The results have shown that the intensity at the focus is very high as compared with that at its vicinity. For example, if an objective lens with a numerical aperture of 1.3 is used to focus a 532 nm wavelength light into SU-8 photoresist, the intensity at the focus at a depth of 10 μm is about three order of magnitude higher than that at an off-axis point located at just 2 μm far from the focus. Thanks to such a high intensity, a chemical change occurs only in the small volume confined by a iso-intensity level, which exceeds a chemical reaction threshold. The chemical change of photoresist used in the fabrication domain is predominated by photo-polymerization reaction, in which monomers are linked together to form a long polymer chain. Polymers, in turn, are twisted together to form a solidified macroscopic structure. Direct laser writing (DLW) takes this principle to realize the fabrication of microstructures.

This chapter is devoted to experiment work. We first describe our experimental setup and equipments, which are necessary for the realization of the DLW technique. Then, we demonstrate the fabrication of some polymer-based photonic structures by use of a pulsed UV laser operating at 355 nm wavelength. We theoretically

and experimentally discuss the different aspects of this one-photon absorption-based confocal microscope setup and the quality of the fabricated structures.

3.1 Direct laser writing system

Generally, the experimental setup for DLW is equivalent to a well-known confocal microscope, which consists mainly of three parts: a light source, a magnification optics system, a substrate/mounting sample translation system and a detection system, as detailed in chapter 1. The experimental setup for DLW in our laboratory is shown

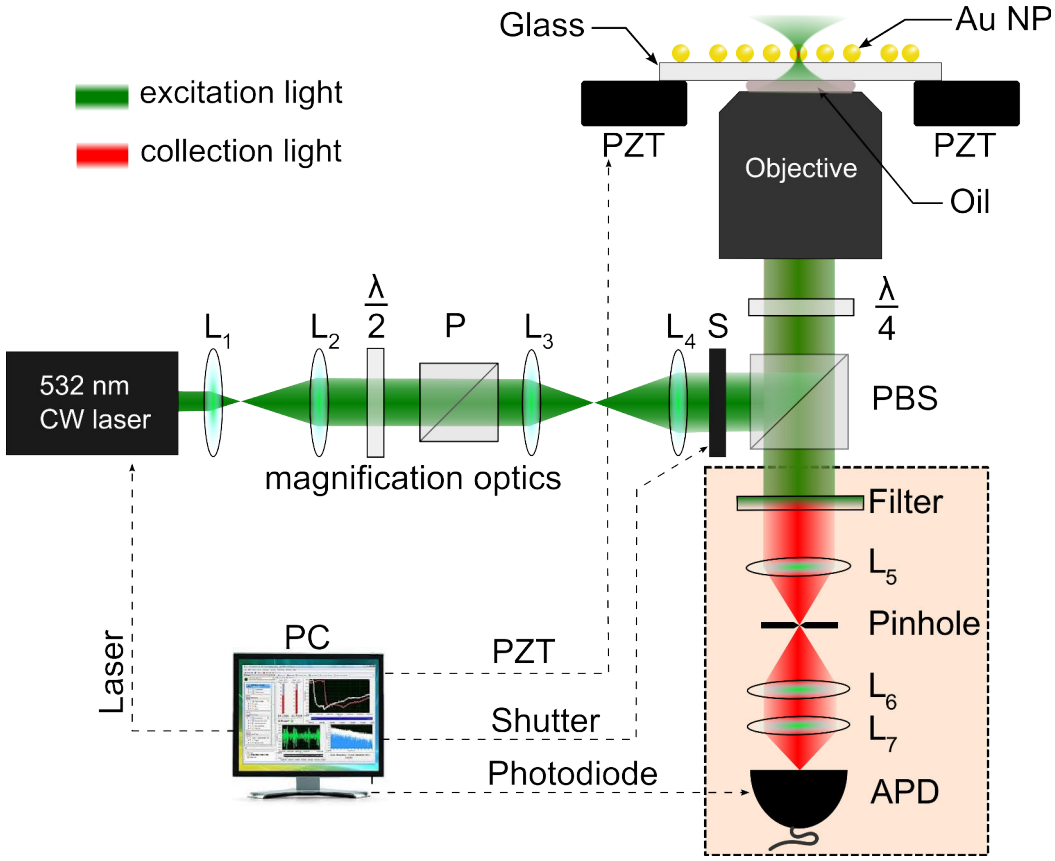

Figure 3.1: Sketch of the experimental setup for direct laser writing. Abbreviation: L: lens, P: polarizer, PBS: polarizer beam splitter, $\lambda/2$, $\lambda/4$: half- and quarter-wave plates, S: electric shutter, PZD: 3D piezoelectric translator, APD: avalanche photodiode, Au NPs: gold nanoparticles, PC: computer connected with electronic hardwares (controllers, PCI cards) and softwares (Igor, Labview programs).

schematically in Fig. 3.1. The laser beam (wavelength of 355 nm or 532 nm) is directed to the "beam stirring and magnification optics" system. Passing through this system, the laser beam is extended and collimated by different lenses. The laser power is monitored by using a combination of a half-wave plate and a polarizer. A quarter-wave plate placed in front of the objective lens (OL) can be rotated to adjust the polarization so as a desired beam polarization (circular, elliptic or linear) is obtained. The "clean" beam with defined polarization and power is then focused into photoresist by a high numerical aperture (NA) OL. The implementation of DLW achieved by scanning the sample with respect the focusing spot of the laser beam. This corresponding movement task is made by a 3D piezoelectric actuator state (PZT). Fluorescence emission collected by the same OL is sent to the detection system. Data acquisition and data analysis are accomplished by an external apparatus and integrated computer softwares.

Below we describe in detail some optical components of the setup, which are used thoroughly in all experiments of the thesis.

Laser source

In this work we used two kinds of lasers, which are continuous and pulsed laser operating at 532 nm and at 355 nm, respectively. In DLW, both of them are used for the fabrication of PCs in SU-8 photoresist. Besides, the 532 nm laser source is also used for all system characterizations (confocal system, data acquisition calibration, *etc.*) using a single gold nanoparticle (Au NP).

- Pulsed laser (Spectra Physics): 355 nm wavelength; maximum averaged power: 300 mW; pulse duration: 1ns; repetition rate: $\approx$ 100 kHz.
- Continuous wave laser (Oxxius): frequency-doubled Nd-YAG laser, 532 nm wavelength, maximum power: 300 mW, Coherence length: 300 m; Pointing stability: 0.005 mrad/C.

Note that the laser power of both lasers can be controlled by a computer.

Translation system

In order to accurately translate the sample with respect to the focusing spot during fabrication, DLW requires a high-resolution piezo-based translation PZT system. In our experimental setup, a high-precision nanopositioning system for up to six degrees of freedom is used (P365 PIMars Nanopositioning Stage - Physik Instrumente). This piezo-based translation system offers large travel ranges of $300 \times 300 \times 300$ (μm^3) and very high precision. According to the company specification, this device possesses a resolution of 1 nm when operating in open-loop and 2 nm in close-loop regime. The stability for an accuracy of about 10 nm can be maintained during a long period of up to 5 hours. However, the precision and the stability is very sensitive to mechanical vibrations and ambiance temperature. We tried to keep the PZT system far away from any mechanical noise source and the room temperature was maintained within 20°-25°C.

Detection system

In our DLW system, the detection system is sketched by a dash-pink rectangle in Fig. 3.1. This system is used for the calibration and optical characterization of the system. The emission of the fluorescent object (glass/photoresist interface, Au NP) is collected by the OL and sent to the detection system. A filter (long pass 580 nm-cut off wavelength) is used to selectively transmit the fluorescent wavelengths while blocking the original excitation wavelength (355 nm or 532 nm). The fluorescent beam is focused into a small spot where a pinhole with diameter of 100 μm is placed so that only the fluorescence from the focusing point of the OL can passes through the pinhole and all out-of-focus light is blocked. After passing the pinhole, fluorescence is detected by an avalanche photodiode (APD) (SPCM-AQRH-13 Perkin Elmer). Optical-electrical signal transformation is performed by a PCI card (6014 M-series, NI). Fluorescence images are then processed by computer software (Labview, Igor)

3.2 Sample preparation

Figure 3.2 shows the sample preparation procedure. The samples following this preparation procedure are supposed to be used in experiments for the characterization of confocal microscope system and for the fabrication of submicrometer structures by one-photon absorption-based DLW. Most of our DLW experiments were done with SU-8 2000 series (MicroChem). For example, a 1D nanograting was patterned on a 0.5 μm thick sample (SU-8 2000,5); 2D micropillar arrays was patterned on 2 μm thick sample (SU-8 2002); 3D photonic crystals were patterned on 25 μm thick (SU-8 2025) samples.

Generally, the procedure is composed of 2 steps: substrate cleaning and material deposition, which are described as follow.

Substrate cleaning

The surface of the glass substrate (160 μm- thickness) is usually covered by dust and organic contaminations, which reduce the adhesion of photoresist to the substrate. In order to increase their adhesive properties, cover glasses must be submitted to a

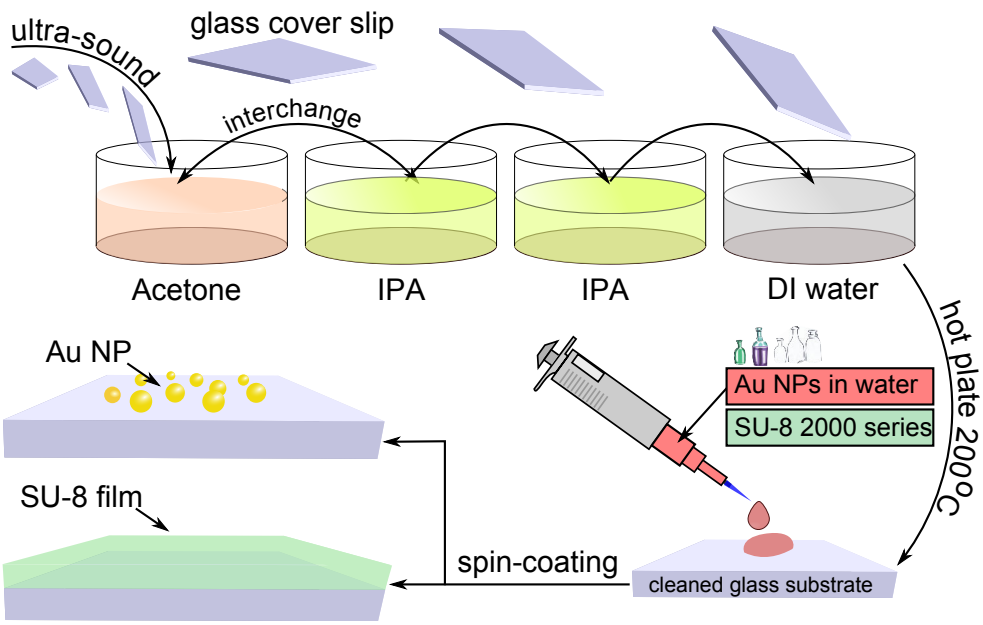

Figure 3.2: Illustration of sample preparation procedure.

cleaning process before the deposition of the photoresist material. Our procedure for cleaning is described as follow.

- Soap and ultrasound cleaning: cover glasses were immersed in soapy water for 10 minutes then cleaned by a cotton swab. To be more effective, cover glasses then were subjected to ultrasound for 40 min to remove dust particles and residues on the glass surface.
- Solvent cleaning: In order to remove oils and residual organic contamination, cover glasses then placed into a tank of acetone for 5 min, then into a tank containing isopropyl alcohol (IPA) for 1 min. This procedure is repeated several times by exchanging cover glasses in acetone and IPA tanks repeatedly. Then cover glasses were rinsed with a fresh IPA solution in another tank.
- Dehydration: After taking out of the IPA tank, cover glasses were rinsed with DI water and dried with a nitrogen gun. The cover glasses were then placed on a hot plate at 200°C for 30 min.
- Cleaned cover glasses are left to cool down to room temperature for 10 min.

After cleaning, cover glasses are ready for the deposition of SU-8 photoresist or Au NP using the spin-coating technique.

SU-8 deposition

After cleaning and cooling down the cover glass substrates, we used them immediately for spin-coating. The sample preparation procedure for SU-8 is described in Table 3.1.

Table 3.1: Sample preparation procedure of SU-8 2000 series

Type	Spinning speed ($rpm.$)	Acceleration ($rpm.s^{-1}$)	Time ($min.$)	Soft-bake ($min.$)		Thickness (μm)
				65°C	95°C	
SU-8 2000,5	2500	200	1	1	2	0.5
SU-8 2002	2500	150	1	1	2	2.0
SU-8 2005	2500	100	1	2	4	5.0
SU-8 2025	2500	100	1	2	7	25

Table 3.2: Sample preparation procedure of Au NP on glass substrate

Type	Spinning speed ($rpm.$)	Acceleration ($rpm.s^{-1}$)	Time ($min.$)	Bake at 160°C ($min.$)
Au NP	1500	100	1	15

Four types of SU-8 2000 series are used in this work. For each, the preparation parameters in order to get the desired film thickness and best performance of used material are shown. SU-8 2000,5/2002/2005/2025 were spin coated on a cleaned cover glass substrate at high speed 2500 rpm, accelerating ramp time for 10/10/30/30 s and hold on for 60 s. Soft-bake was applied just after several minutes of relaxation at room temperature using hot plates, at 65°C for 1/1/2/2 min, then at 95°C for 2/2/4/7 min. The samples were then cooled down to room temperature and stored overnight away from light in a box before exposure. Besides the ordinary conditions of the sample preparation procedure, we have found that the adhesion is not sufficiently good if the after-softbaked sample is not relaxed for at least a half of day. The same sample preparation procedure was strictly kept for all our experiments.

Gold nanoparticles deposition

In experiments for system characterization or measurement calibration, 50 nm diameter Au NPs (Sigma-Aldrich) were spun-coated on a cleaned cover glass following the parameters as described on Table 3.2.

3.3 Optical characterization of SU-8 photoresist samples

SU-8 is a kind of negative tone photoresist, which is composed of a resin, a photoactive compound, and a solvent. When illuminated with light, the resin is converted into an insoluble form typically by undergoing an increase in molecular weight or by

formation of a new insoluble molecule. The increase in molecular weight is generally achieved by polymerization or cross-linking of resin monomers. Insolubility can also be attained by initiating a photochemical reaction to alter polarity or hydrophobicity. For polymerization and cross-linking reactions, the photoactive compound is generally a photoinitiator which forms free radicals or strong acids upon exposure to light.

On the way of realizing OPA microscopy-based applications, qualitative characterization of absorption and fluorescence of SU-8 is required in order to gain knowledge about the one-photon response of material. For this purpose, one should optically measure the absorption band and fluorescence spectra when material is exposed to Ultra-Violet-Visible (UV-Vis) light.

To measure the absorption band of SU-8 we prepared three sets of samples with 2 μm, 5 μm, 25 μm thickness. The absorption spectra was recored by Perkin Elmer UV-Vis Spectrometer for absorbance measurement. Figure 3.3-(a) shows the measured absorbance of a 25 μm thick film. We note that, although the absorbance is very close to zero for wavelengths larger than 400 nm, SU-8 still presents a linear absorption even at 532 nm.

To obtain the absorption coefficient from the measured absorbance, we apply the

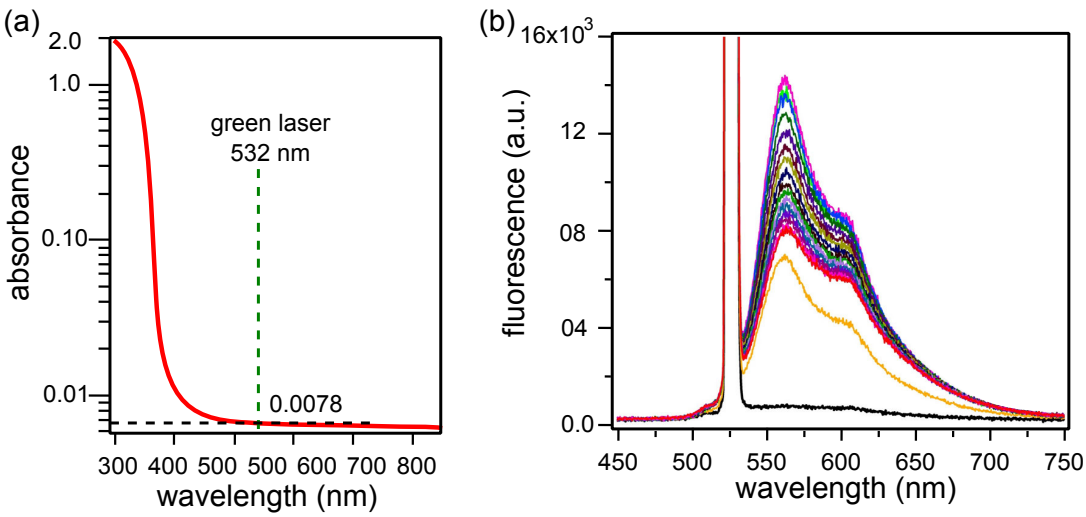

Figure 3.3: (a) Absorbance spectrum of uncured SU-8 photoresist with a thickness of 25 μm at $\lambda = 532$ nm, the absorbance is about 0.0078. (b) Fluorescence spectrum of SU-8 as a function of time, obtained by an excitation at $\lambda = 532$ nm.

following relation [90]:

$$\alpha = 2.303\frac{A}{d}, \tag{3.1}$$

where α is the absorption coefficient, A is the absorbance, d is the film thickness and 2.303 is a conversion factor from a decimal to natural logarithm.

The relationship between the absorption coefficient α and extinction coefficient κ is:

$$\kappa = \frac{\alpha\lambda_0}{4\pi}, \tag{3.2}$$

where λ_0 is the wavelength of light in vacuum.

From the above relation we calculate the extinction coefficient of SU-8 for a film thickness of 25 μm at a wavelength of 532 nm: $\kappa = 0.0000306419$. This result plays a particularly and extremely important role in our theoretical as well as experimental studies in this thesis.

According to the measured absorption spectrum of SU-8, we examined fluorescence spectra by applying an excitation light at 532 nm. For this experiment, a green laser, of about 100 mW, was lightly focused into a 25 μm-thick SU-8 sample by using a simple lens of $f = 100$ mm. The fluorescence was detected by an Ocean spectrometer. Figure 3.3-(b) shows the fluorescence spectra of SU-8 photoresist, in which 15 curves corresponding to the fluorescence spectra measured at different exposure times are recorded. The exposure time at which we recorded the fluorescent spectra are 10 min, 20 min... 150 min which correspond to curves from the vertically lowest to the highest orders. We found that the fluorescence signal decreases quickly as a function of time, probably due to the polymerization effect. The study of fluorescence mechanism of SU-8 is out of the scope of this study. The important conclution is that SU-8 absorbs a laser beam at $\lambda = 532$ nm and emits in the VIS range. Based on this fluorescence measurement, we therefore used a long-pass filter with a cut-wavelength at 580 nm to detect only the fluorescence signal. The fluorescence signal of SU-8, even very weak, allows to characterize the sample, particularly for the determination of the glass/photoresist interface.

3.4 Characterization of the confocal microscope system

The alignment and the characterization of the optical system is a very important task in DLW to get rid of some optical aberrations. In an imaging system, optical aberrations normally refer to distortion, spherical aberration, chromatic aberration, coma, astigmatism, Petzval field curvature, defocus and tilt. Almost optical aberrations originate from the imperfection or defects in optical devices, some of them are due to the misalignment of optical elements within a system [91]. Determining what aberrations are present in an optical system is not always an easy task. Usually two or more aberrations are present in any given system. Experimentally we should get rid of certain aberrations due to the misalignment of the optical system. However, spherical aberrations inherently exist in most DLW systems due to the refractive index change between different media. Alignment and optical characterization are mutually related and hence need to be optimized.

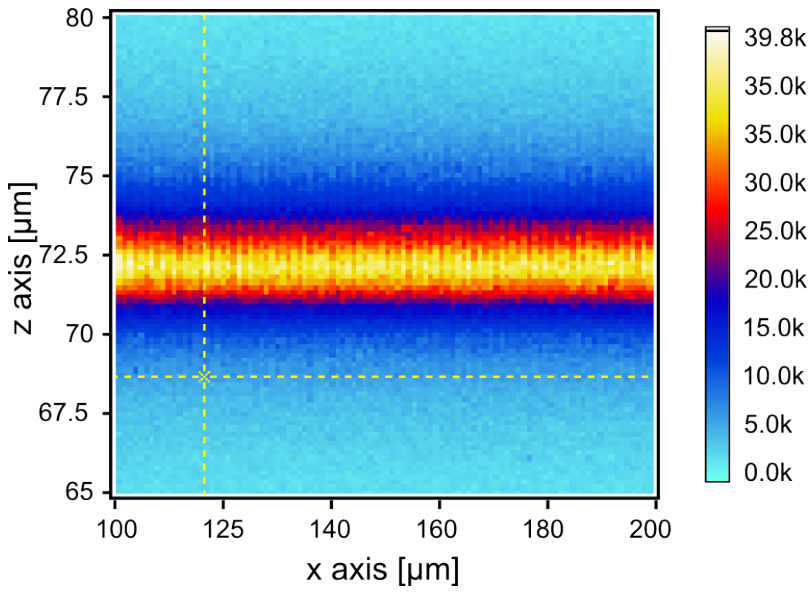

Figure 3.4: Fluorescence image in the (xz)–plane in an interface determination experiment. The bright strip close diffraction limit width containing the interface. The exact z–position of the interface is obtained by curve fitting.

Before starting an experiment with DLW, we always check the state of the system by using a Au NPs sample. Imaging a single Au NP is a good way to verify whether the system is well aligned or not. Here we show an experiment, in which we "correct" the DLW system from misalignment.

In this test, a circularly polarized laser beam with wavelength of 532 nm was focused by a NA=1.3 lens in the back side of a cover glass substrate through a oil+glass media. On top of the back side, 50 nm-diameter spherical Au NPs were prepared following the procedure that we have described above.

The characterization of the system starts by scanning the focusing spot in a longitudinal (xz)–plane to determine the air/glass interface. An example of Au NPs fluorescent image is shown in Fig. 3.4. In this image, the bright horizontal strip indicates the fluorescence at the air/glass interface. The width of the strip is about $500 - 600$ nm and cannot be narrower because of axial diffraction limit. Hence the interface position (z–value) is determined only via data plotting and data fitting using computer softwares. Once the air/glass interface position has been determined, we scanned the focusing spot in the (xy)–plane at a z–position corresponding to the interface.

Figure 3.5–(a) shows a fluorescence image obtained from a scan in the (xy)–plane and at $z = 72$ μm. In this image, Au NPs appear as blue dots. It is worth to note that, by spin-coating technique, Au NPs are not usually well separated from each other. On a glass substrate, both single particles and cluster of gold particles are found. By zooming–in a bright blue dot we are going to image a single particle. Figures 3.5–(b) and 3.5–(c), show the fluorescence images obtained by scanning in the (xy)–plane and the (xz)–plane, within a 2×2 (μm) range. The bright spot at the center of each image represents the emission of a single Au NP. Note that, for the same excitation power, the Au NP fluorescence is much higher than that of the air/glass interface. Since the size of Au NPs is very small (50 nm), it can be considered as a point-like source. The fluorescence spot of a single Au NP therefore represents the point spread function (PSF) of the used OL. The experimental axial and lateral sizes of the PSF function is about 0.240 μm and 0.580 μm, respectively. These values being close to the theoretical ones.

From this test, we confirm that the optical system is well aligned and ready for

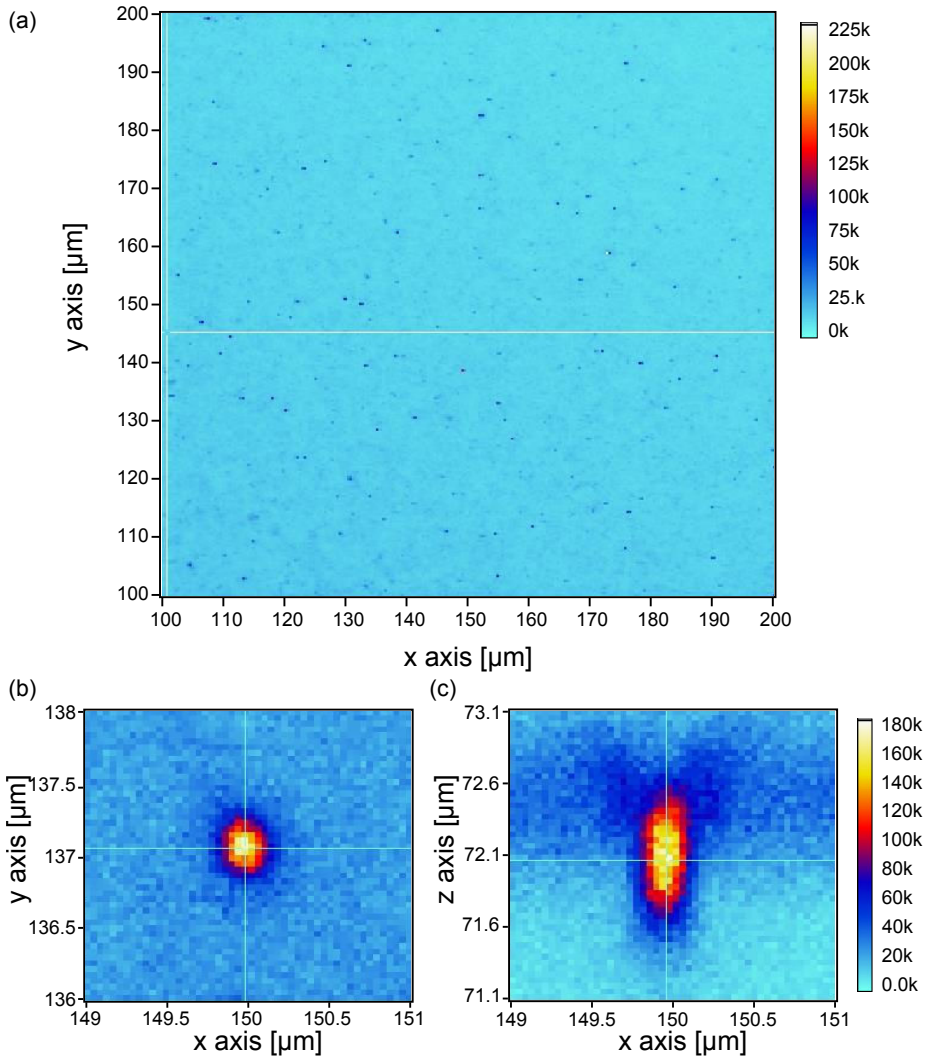

Figure 3.5: (a) Scanning image in the (xy) plane: Au NPs appear to be blue dots. In the color bar, k stands for $\times 10^3$. (b) and (c) micrographs of the scan in the (xy) and the (xz) planes: PSF function of a single Au NP in both lateral and axial axis.

fabrication. However, we note that there exists a small distortion of the focusing spot, as evidenced in Fig. 3.5-(c), due to the refractive index mismatch between glass and air. This spherical aberration is further tested by using other OLs. Figure 3.6 shows the simulation and experimental results for three different OLs. The spherical aberration is clearly seen and is impossible to eliminate in such application. However, we expect that when working with a glass/photoresist interface, this effect will be minimized.

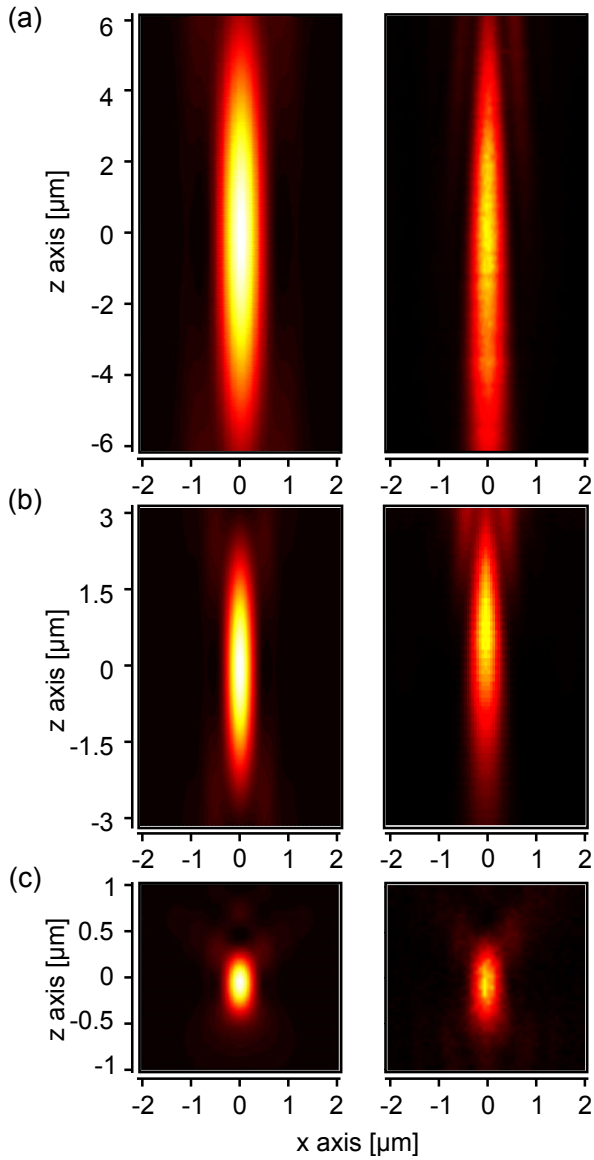

Figure 3.6: Fluorescence images of the single Au NP obtained in the (xz)–plane with (a) NA=0.4, (b) NA=0.65 and (c) NA=1.3. Left: Simulation results; Right: experimental results.

When the confocal system is well characterized and optimized, it is ready for the fabrication of polymer-based photonic structures by DLW technique.

3.5 Fabrication of 1D and 2D photonic structures by one-photon absorption-based DLW

In this section, we realize one-photon absorption (OPA)-based DLW for the fabrication of micrometer scale structures. In this experiment, an OL with NA of 1.3 is used; SU-8 is used as the photoresist and a laser source with wavelength of 355 nm (UV laser) is used as the excitation source. Figure 3.7–(a) shows the measured absorbance of SU-8. At 355 nm, absorbance is 0.464, which corresponds to an extinction coefficient of 0.0012. At this wavelength, the structure of the diffraction pattern at the focus is more or less the same as for the case previously investigated in Fig. 2.9–(c) and Fig. 2.11–(b). SU-8 photoresist at this wavelength exhibits a quite high absorption. In photolithography and interference lithography, this wavelength is preferred because of efficient fabrication of 2D structures.

In Fig. 3.7–(b) the normalized maximum intensity at the focus is plotted as a function of the focus depth. The calculation was performed for NA = 1.3, a wavelength of 355 nm and an extinction coefficient of 0.0012. The result shows that the intensity of the focusing spot decreases quickly as the focus depth increases. The maximum

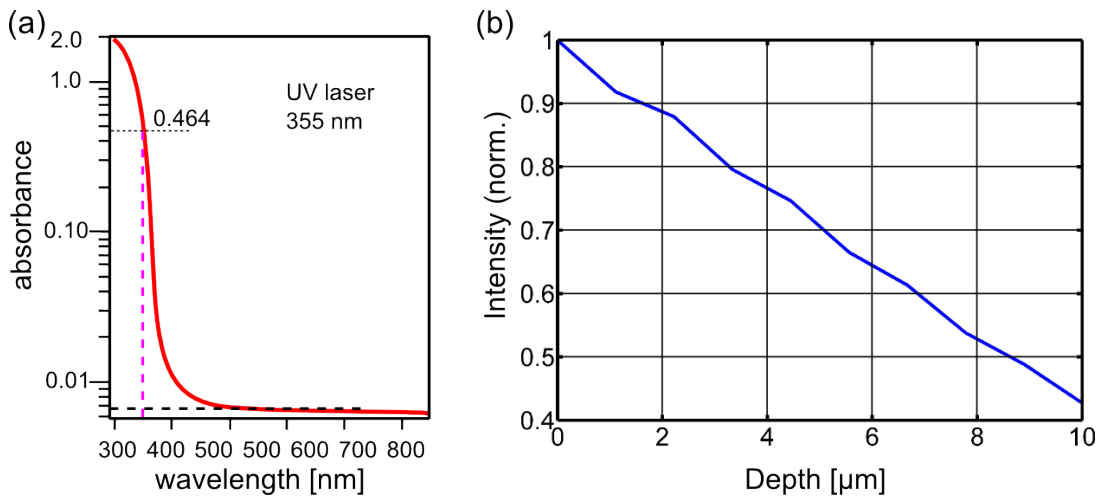

Figure 3.7: (a) Absorption spectrum of SU-8 photoresist. (b) Normalized maximum intensity at the focus as a function of depth. The calculated extinction coefficient of SU-8 at a wavelength of 0.355 μm is 0.0012

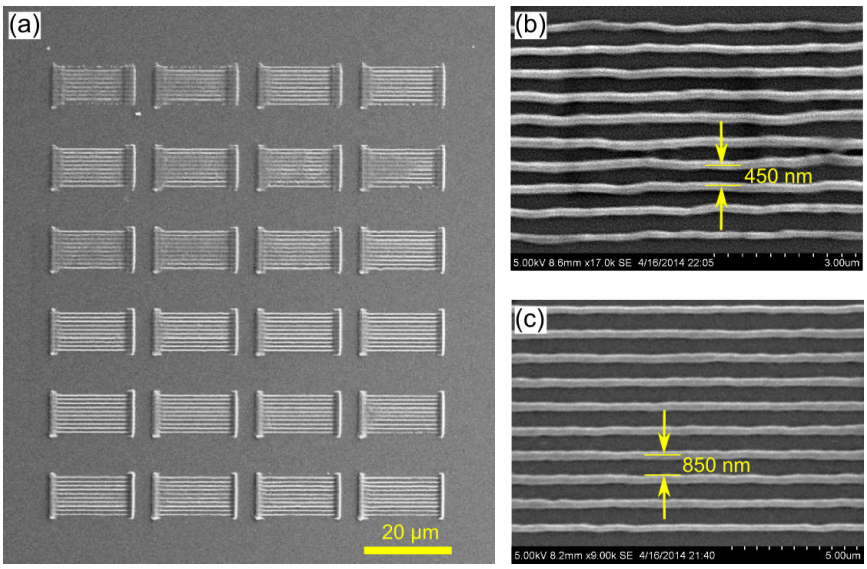

Figure 3.8: Fabrication of low dimensional structure by high absorption DLW. (a) SEM image of 35 different 1D CPC structures with different scanning speeds, ranging from 10 μm/s to 28 μm/s. Zoom-in views of a 1D CPC structure with the pitch of (b) 500 nm, and (c) 1000 nm.

intensity at the focus at a depth of 10 μm is reduced down to 43% as compared to that at interface. Therefore, a DLW employing this excitation wavelength allows to fabricate structures with limited thickness .

In the first experiment we fabricated a series of nanogratings on a 0.5 μm thin film of SU-8 photoresist. A nanograting pattern consists of parallel lines made of SU-8, surrounded by air gap. A nanograting is fabricated by scanning the laser spot relatively to the sample one-by-one along the x-axis. The laser power and scanning speed are important parameters, which define the line width of the structure. An increase of the laser power or a decrease of the scanning speed broadens the line width. To identify the condition of fastest writing and smallest features, the scan speed was closely fixed to the maximum speed of the mechanical stage and the laser power was varied. No pattern was left when the photoresist was exposed below a certain threshold laser power. Under an optimized laser power for the smallest line width and stable features, submicron patterns could be obtained.

Figure 3.8–(a) shows a SEM image of an patterned sample in which we fixed the scanning speed to 10 μm/s while varying the laser power from 50 μW to 170 μW by an

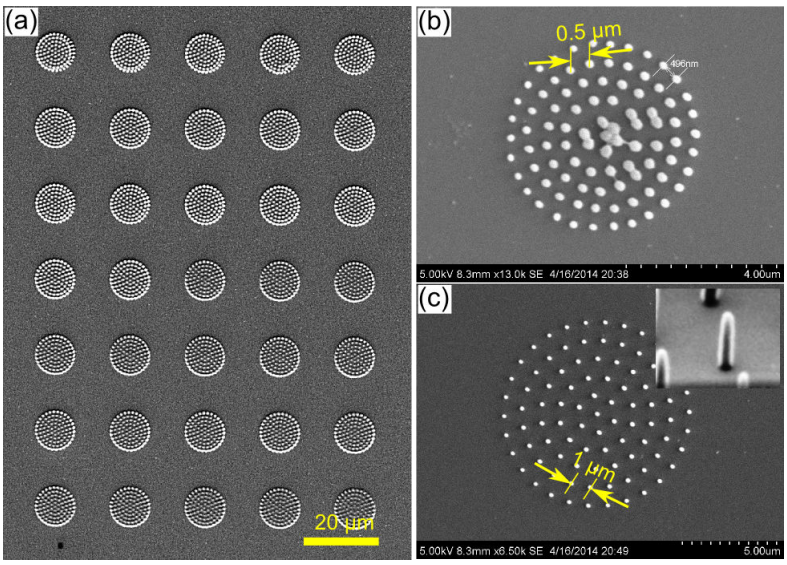

Figure 3.9: Fabrication of low dimensional structure by high absorption DLW. (a) 1D nanograting structure and (b) 2D CPC structure.

increment of 5 μW. The optimum power of 70-90 μW and optimum scanning speed of 10-12 μm/s were derived from those experiments. Figure 3.8–(b)-(c) show experimental results of the fabricated structures when applying these optimum parameters. Very small feature sizes have been obtained, for example, in Fig. 3.8–(a) nanogratings with a 150 nm line width and 500 nm pitch are fabricated.

In the second experiment we fabricated a series of circular photonic crystals (CPCs) on a 2.0 μm thin film. CPC is a periodic structure, which consists of concentric micropillars growing on the substrate. The CPC structure is applied, for example, to improve light extraction efficiency and output uniformity of a photoelectric conversion device [92]. We also carried out several tests in which either laser power is fixed while the scanning speed is varied or vice-versa. The aim of these experiments were same as that of the first experiment: optimization of the fabrication parameters to get the smallest feature size. In Fig. 3.9–(a), a SEM image shows a series of CPC structures, which are fabricated by fixing the laser power to 50 μW while varying the scanning speed from 10 to 28 μm/s along z direction across the entire thickness of the sample. The obtained optimum power obtained from these experiments is 50 μW and optimum scanning speed is 22 μm/s.

Applying these optimum parameters we carried out further experiments in which the period (of CPC structures) was changed. The goal of these experiments are to reach the smallest possible size of these structures. For example, the CPC structure shown in Fig. 3.9–(b) has a 500 nm period. It is obvious that the diameter of micropillars in each pattern varies from the periphery to the center, in particular when the period decreases to the diffraction limit.

Inset of Fig. 3.9–(c) shows a micropillar with narrowed tip. The diameter of the pillar at the top is ten times smaller than that of its base. This effect can be explained by our calculation, which has been shown in Fig. 3.7, *i.e.* that the maximum intensity at a depth of 1.5 μm is ten times smaller in comparison with the maximum intensity at the interface. The absorption effect, which leads to the deformation of the structure, is more pronounced when increasing the height of the structure.

Now we examine an important case where OPA DLW using UV-light is attempted to fabricate 3D PC. Sketch on the top of Fig. 3.10 shows a 3D woodpile PC, which consists of layer-by-layer of stacked parallel rods with a half -period shift between two successive layers in the same direction. The width of the rod is defined by w; the distance between two adjacent rods is defined by d; the distance between two adjacent layers is defined by h and the distance between two adjacent unit cell is defined by c. The construction of the structure using DLW is described as follow. First, the first layer was written on the cover glass substrate (each rod is written along the x direction). The second layer was then written along the direction perpendicular to the first layer, vertically separated by a distance h from the first layer. The third layer was constructed in the direction perpendicular to the second layer (hence parallel to the first one), and was shifted by $d/2$ along the y direction with respect to the first layer. The forth layer was written on the top of the third one, also distances by h from the third one and was shifted by $d/2$ with respect to the second layer. Repeat the procedure by layer-by-layer stacking in the same manner until the height of the structure meets specification. In the experiment with a 3D woodpile structure, we carried out many tests by varying the laser power and scanning speed, alternatively. We also varied the size of the structure by changing the distance between two adjacent layers (hence the size of overall structure is changed accordingly). However, after many tests, we found that no structures were fabricated or most fabricated structures

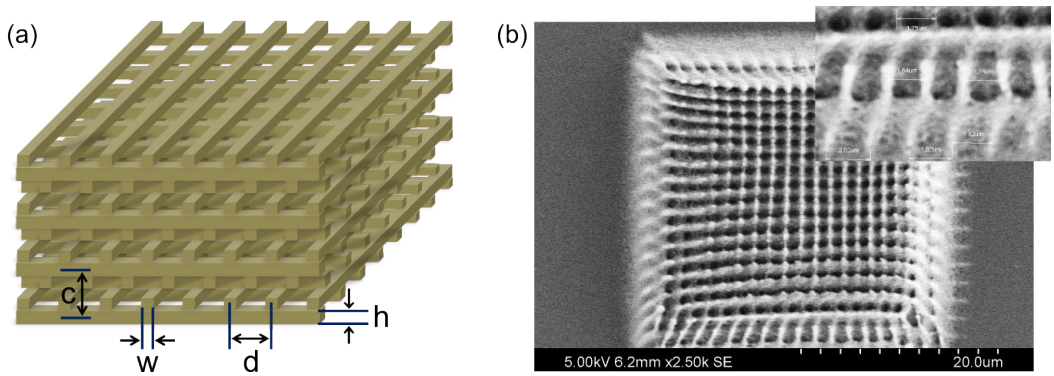

Figure 3.10: Fabrication of 3D PC structures by strong absorption DLW. (a) a model of 3D woodpile structure. Parameters c, w, d, and h are defined in the text. (b) Experimental result of woodpile structure. Image shows the structure's top-view and a part of the side-view (inset). While very poor quality of spaced rods is observed from the top-view, no separated rods is observed from the side-view.

were completely solidified even if the laser power was sufficiently weak. Among many experimental results, the structure shown in Fig. 3.10–(b) was the best one. In this structure there are some spaces between rods. Separated rods can be seen from the edges of the structure or only at the top but not in the bottom part. Once again, this result confirms the strong absorption effect of the SU-8 photoresist at 355 nm. We confirmed that there is no way to improve this problem and the fabrication of 3D PCs with UV light was unsuccessful. However, this result suggests that if the absorption effect is decreased, we could obtain clear 3D structures.

3.6 Discussions and conclusions

We have presented in detail about the experimental setup and different aspects which affect the quality of the DLW system. We described the sample preparation procedures for SU-8 and Au NP samples. We evaluated the tolerance of the confocal system through imaging the PSF of single Au NP. The PSF can be considered as a figure of merit of confocal system, which depends on numerous optical components used in the system. The strong absorption of the material (such as SU-8 which strongly absorbs the UV-light) is compatible with an efficient fabrication of 1D and 2D structures with feature size of about several hundreds nanometers, but it is impossible to fabricate 3D

PC structures. The effect of strong absorption imposes a limit to 3D fabrication not only along the third dimension (z–dimension), (hence the working thickness is limited), but also perturbs the uniformity of the fabricate structures. However, through these tentative fabrications of 3D structures with one-photon absorption, results suggest that the fabrication of 3D structures is probably possible if the linear absorption could be minimized. The fabrication of 3D structures in a low absorption regime will be theoretically and experimentally presented in the next chapter.

Chapter 4

Low one-photon absorption direct laser writing

Direct laser writing (DLW) has adapted two excitation mechanisms for photo-induced fabrication of sub-micrometer structures, namely one-photon (OPA) and two-photon absorption (TPA), aiming at specific applications. Indeed, when using a thin film, the OPA excitation method is a very convenient technique, based on a simple and low cost laser source operating at a wavelength located within the absorption band of the thin film material. However, due to a strong linear absorption, this method is limited to the surface of the sample, *i. e.* to a two-dimensional (2D) scanning as evidenced in chapter 3. High spatial resolution 3D imaging or fabrication is therefore impossible with OPA method applied to strongly absorbing samples. In contrast, TPA excitation provides intrinsic 3D addressing, thanks to a local nonlinear absorption, which occurs only for the very high local intensity provided by tight focusing in a confocal laser scanning microscope (CLSM) combined with a femtosecond laser operating at a wavelength around 800 nm for which the material is fully transparent [93, 94]. This TPA nowadays allows many potential applications in different domains, in particular, for 3D imaging and 3D fabrication of sub-microstructures, but requires expensive laser sources and complicated optical components [95–98].

With aim of reducing the cost of the production and simplifying the fabrication system, we developed a new method based on the ultra-low absorption (LOPA) of the photoresist at a particular wavelength. The technique is expected to fabricate desired

1D, 2D and 3D submicrometer structures equivalent to those obtained by TPA.

In this chapter, the blueprint of this novel method is presented in section 4.1 and experimental realization of the method for the fabrication of 1D, 2D and 3D photonic submicrometer structures is shown in section 4.2. In the last section of this chapter, a conclusion and a discussion of the method for a potential wide range of applications are presented.

4.1 Concept of low one-photon absorption direct laser writing

On the course of demonstration of the new technique, we made use of SU-8 photoresist as a typical representative of the photosensitive material class, which is widely used in MEMs as well as in many other applications. First, we theoretically make a short comparison between high and low absorption of SU-8 photoresist at different wavelengths, which allows us to introduce the LOPA concept and to identify LOPA's requirements. Finally, we discuss about a specific application of LOPA for DLW.

In Fig. 4.1 the maximum intensity at the focus is plotted as a function of focus depth for a numerical aperture (NA) of 1.3 and three values of SU-8 extinction coefficients. These extinction coefficients are calculated by the formula and the absorption spectrum shown in chapter 3. For clarity only a depth range of 25 μm is plotted. We compare three specific cases. The first case deals with a wavelength of 308 nm with an extinction coefficient $\kappa = 0.0059014$ located at the peak absorption of SU-8. In such a case the intensity at the focus exponentially decreases and comes very close to zero beyond a depth of 20 μm. For some applications such as in nanoelectronic circuit design where a thin film ($<$ 500 nm) is treated, an excitation wavelength located at the absorption peak is favorable for efficient fabrication. DLW operating at this wavelength offers rapid fabrication and high resolution. The second case deals with SU-8 photoresist and an excitation wavelength of 355 nm. This scheme is very common practice in photolithography, particularly for high-aspect-ratio structure fabrication. However, SU-8 photoresist at this wavelength still possesses a quite large extinction coefficient $\kappa = 0.0009004$. Again, the maximum intensity of the beam focus

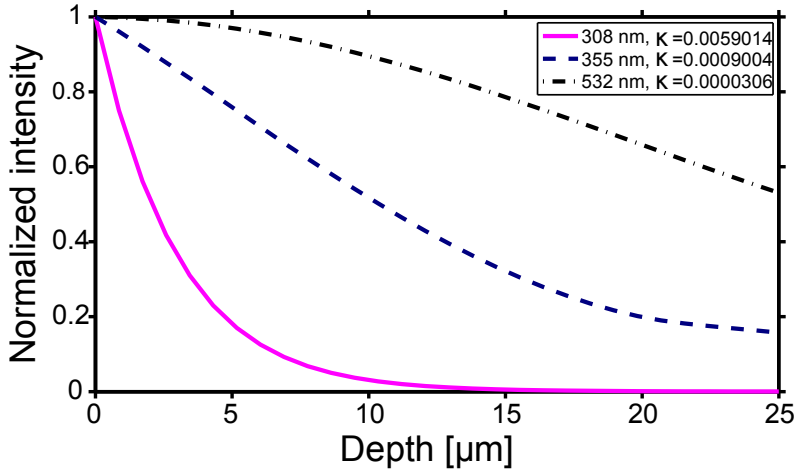

Figure 4.1: Maximum intensity at the focus plotted as a function of focus depth for three extinction coefficients of SU-8: $\kappa = 0.0059014$ (solid-violet curve) at $\lambda = 0.308$ μm; $\kappa = 0.0009004$ (dash-blue curve) at $\lambda = 0.355$ μm; And $\kappa = 0.0000306$ (dash-dot-black curve) at $\lambda = 0.532$ μm. Calculated for NA=1.3, λ=532 nm, $n_1 = 1.51$ (glass) and $n_2 = 1.58$ (SU-8).

attenuates rapidly from the surface as it travel through a glass/photoresist interface. According to our calculation, only 20% of the maximum intensity is retained after propagating through a distance of 25 μm from the interface. Now we consider the third case, where a wavelength of 532 nm is used for excitation. In this case, the attenuation factor at the extinction coefficient $\kappa = 0.0000306$ is really small, the maximum intensity retains 60% after traveling a distance of 25 μm from the interface.

Actually, the absorption of SU-8 at 532 nm is really low as compared to that at 308 nm and at 365 nm. To know how the attenuation of the maximum intensity in the case of 532 nm is close to the case without absorption, we do compare the trend of attenuation between lossy and lossless cases while keeping the same conditions of the system (except setting the extinction coefficient to be zero for the lossless case). In addition, we compare between two cases: with mismatched refractive index (MRI) and without mismatched refractive index (MRI-free). The former is supposed to be the main cause of attenuation in the cases shown in Fig. 4.1.

In Fig. 4.2 the maximum intensity of the focus is plotted as a function of focus depth for a NA = 1.3, wavelength $\lambda = 532$ nm and two extinction coefficients: $\kappa = 0$ corresponding to the lossless case (solid-red curves) and $\kappa = 0.0000306$ corresponding

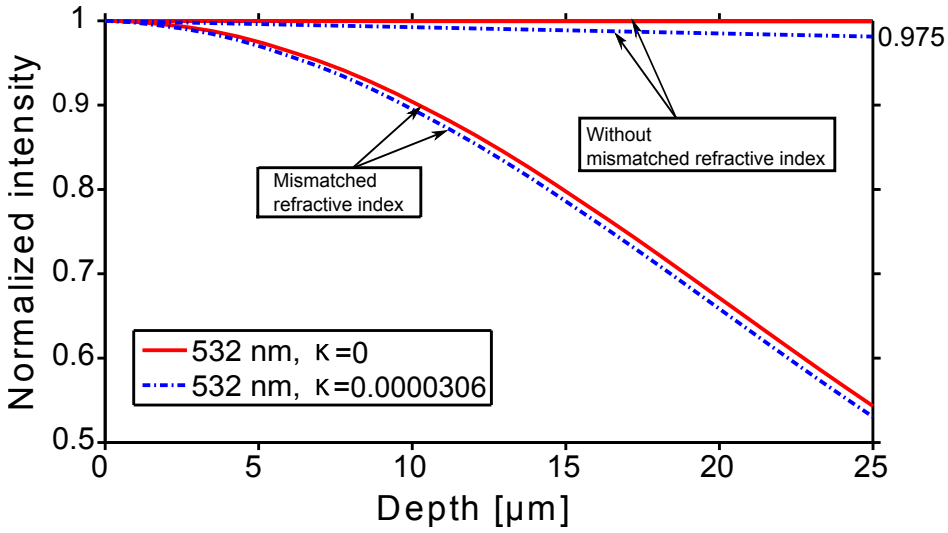

Figure 4.2: The normalized maxima intensity at the focus is plotted as a function of focus depth for two different circumstances: with MRI ($n_1 = 1.51$, $n_2 = 1.58$) and without MRI ($n_1 = n_2 = 1.58$). Calculated for NA=1.3, λ=532 nm and $\kappa = 0.0000306$ (dash-blue curves). For comparison, the corresponded case of without absorption is also plotted (solid-red curves).

to the lossy case (dash-blue curves).

We examine the first situation where MRI is present in the system (two curves at lower part in Fig. 4.2). In this case, the refractive index of the first and second medium is $n_1 = 1.51$ and $n_2 = 1.58$, respectively. The result shows that, the curve corresponding to lossy case traces very closely to the lossless case when increasing the focus depth, which means that SU-8 possesses an ultra-low absorption at the wavelength of 532 nm. Electromagnetic wave propagates in SU-8 like in a transparent medium. The deviation between both cases is only 2.5% at a depth of 25 μm and becomes progressively larger as depth increases.

I n keeping the same conditions, we now consider the case of MRI-free (the refractive index of the first medium is the same as that of the second medium, $n_1 = n_2 = 1.58$). Calculation results show two curves at the higher part in Fig. 4.2. The behavior of the maximum intensity versus depth is as expected. Indeed, the lossless case show evidently that the maximum intensity does not attenuate at all along the propagation, since the two media are optically identical. In the lossy case, maximum intensity attenuates along the propagation with very weak losses.

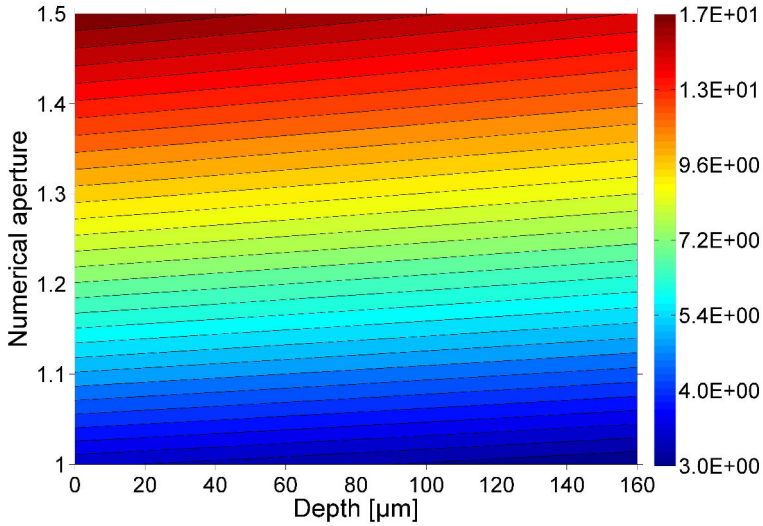

Figure 4.3: Maximum intensity as a function of both NA and focus depth for the case without MRI. Calculation for a wavelength of 532 nm, an extinction coefficient $k = 0.0000306$ and refractive indices $n_1 = n_2 = 1.58$.

In comparison between MRI and MRI-free we see that the deviation of the lossy curves from lossless curves are almost the same. This result confirms that MRI is the main cause of attenuation of the maximum intensity at the focus in the ultra-low absorption case.

Results in previous chapter have shown the propagation of the maximum intensity as a function of both NA and focus depth when MRI is present in the system. In such a case, the maximum intensity at a certain depth can be weaker with a high, rather than a low, aperture lens. This irregular behavior leading one to chose a low aperture lens for their experiments when they have to face with a mismatched refractive index. Otherwise, if one can find out a solution to match refractive indices, one can freely to use their highest aperture lens to get better results, especially in applications where the working region is located at a large depth within an absorbing medium. This statement can be approved by our following calculations.

In Fig. 4.3, the maxima intensity is plotted as a function of NA and depth. The first and second material have the same refractive index of 1.58 (refractive index matching) and the extinction coefficient of SU-8 is taken from the ultra-low absorption case of the example shown above. Figure 4.3 shows 30 contours of constant intensity.

In contrast to the case of Fig. 2.11–(c), in this calculation the irregular behavior has disappeared. On the contrary the linearity behavior of the maximum intensity predominates. The upslope of every contour (due to absorption) is quite small because of the small extinction coefficient of SU-8 at the used wavelength. When going from NA = 1.0 to NA = 1.5, the maximum intensity increases by approximately 6 times. This may gain the input laser power up to 6 times when one decides to use an objective lens with NA of 1.5 instead of 1.0.

As a conclusion for this section, we can draw some attentive conclusions thanks to the above theoretical results, as follows. When light is focused from a transparent medium to an absorbing medium, two problems need to be considered if one wish to have the highest intensity at the focal region:

(1) - Absorption strength: In many kinds of applications, strong absorption, rather than weak absorption, is desired. But in 3D imaging systems and DLW, strong absorption must be avoided. In such a case, low or ultra-low absorption is desired. In an ultra-low absorption regime, excitation light can penetrate over a long distance, rather than only in a short distance from interface as in the strong absorption case, to excite specimen or trigger a polymerization. We always have an opportunity to get low or ultra-low absorption within the visible spectrum for almost materials. Indeed, most materials which are currently used in these applications (SU-8, AZ, EPON...) possess an absorption spectra in visible range. At the edge part (sometimes in the valleys) of the absorption band, the absorption is very weak, or close to zero. If a laser, whose wavelength falls within this range, is applied, the light intensity distribution remains almost the same as in the absence of material when traveling in the medium. In DLW, a high aperture lens is usually a favorite choice since it provides a very high intensity at the focus, about million times higher as compared to that at the entrance pupil of the lens. Although the absorption is ultra weak at this wavelength, the effective photo-induced effect in focusing region is therefore comparable to that obtained at the maximum absorption wavelength with a moderate intensity. Accordingly, photopolymerization reaction is strongly dominant at the focusing region. In some cases, the photo-induced effect is only observed at the limited size focusing spot where the intensity is high enough to induce physical or mechanical or chemical changes.

(2) - Effects due to optical aberrations: Effects due to optical aberrations (coma, astigmatism, field curvature, *etc.*) are frequently encountered in optical laser scanning microscopy as well as in DLW. These effects cause barrel distortion and pincushion distortion in the imaging system. In DLW, an imperfection in the focusing spot may result in a deviation and distortion in the shape of the fabricated structures. Because of their influence on the quality of the focusing spot, one must get rid of these effects out of the optical system. Fortunately, most commercial lenses are corrected, so chromatic aberration and spherical aberration are mostly treated. The other effects depend on specific applications chosen by the operator. In previous chapters, we have taken into account spherical aberration, which originates from MRI between two media having different indices of refraction. We have seen that, due to spherical aberration, the nonlinear behavior is a predominant effect on the distortion of maxima intensity domain, resulting in a reduction of intensity as depth increases, even if no absorption is present. In this section, we have shown that, if one can eliminate MRI out from the system, the nonlinearity, hence, should be suppressed. In such a case, a high NA objective lens is better to concentrate the electromagnetic field at the focus region resulting in a higher maximum intensity. Such a small and symmetrical focusing spot provides higher resolution.

With all above remarks we have been able to introduce a new idea for 3D imaging and 3D fabrication by means of DLW dealing with one-photon absorption. The new concept is low one-photon absorption microscopy (LOPA), based on three factors:

1 - **Low or ultra-low one-photon absorption**

2 - **Optical aberration-free**

3 - **Strong focusing**

The experimental realization of LOPA microscopy is trivial and straightforward. The first requirement is fulfilled when one choses to work with a monochromatic light source whose wavelength is within a low absorption spectral domain of the material. The second requirement is a bit harder to satisfy: one must get rid of MRI by using an appropriate intermediate immersion medium (oil, ethanol, water, *etc.*) in contact with the substrate or in direct contact with the absorbing medium (where the specimen or photoresist is located). The final requirement is simple (but rather costly) corresponding to a high NA and aberration-free objective lens.

LOPA microscopy in conjunction with regular DLW is called LOPA DLW. On realizing LOPA DLW we use just a simple and low cost CW laser as a monochromatic light source. The laser wavelength 532 nm, the same wavelength with that used in the numerical calculation. SU-8 negative tone photoresist is used as an absorbing material. A high NA oil-immersion objective lens of NA=1.3 is used to focus the laser beam into the photoresist. So, 532 nm CW laser, SU-8 and NA=1.3 lens are the three parameters which almost satisfy the requirements of LOPA microscopy. System alignment is the last condition which must be taken into account so that all LOPA microscopy requirements are fully satisfied. In the next section, we experimentally demonstrate the LOPA microscopy idea by realizing LOPA DLW.

4.2 Experimental demonstrations

4.2.1 LOPA-based direct laser writing technique

By using a standard fabrication process that already described in chapter 3, we demonstrated that LOPA-based polymerization is achieved only at the focusing spot, where the excitation intensity is strong enough to simultaneously trigger local photochemical reactions leading to polymer cross-linking during the subsequent post-exposure bake step. Note that, in the case of two-photon polymerization DLW, there exists a first threshold related to light intensity, above which two photons are simultaneously absorbed, and a second threshold related to dose, above which complete photopolymerization is achieved. However, it should be borne in mind that resist exposure is also per se a highly nonlinear process. Indeed, there exists a dose threshold above which the polymerization process can be fully completed. An example of the complete polymerization condition is the use of the interference technique with a low power continuous-wave laser to fabricate 2D and 3D structures [99]. Therefore, in the case of LOPA, there exists only one threshold related to dose. Furthermore, thanks to the high intensity of the focusing spot, complete photopolymerization is only achieved in a small focus. Figure 4.4 shows an example of experimental results, imaged by a scanning electron microscope (SEM). For each exposure a solid volumetric structure, so-called “voxel”, is formed at the focusing spot. A volumetric structure is then build

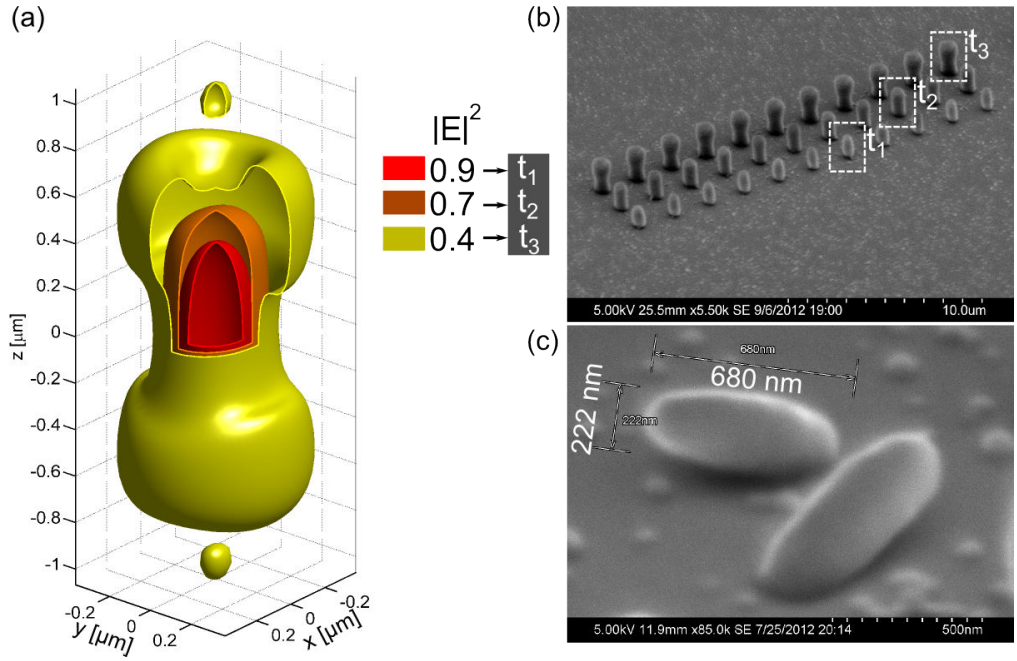

Figure 4.4: Fabrication of voxels by single-shot exposure. (a) Theoretical calculation of the contour plot of light intensity at the focusing region (NA= 1.3, $n = 1.518$, $\lambda = 532$ nm). This experimental results explain the OPA nature where the formed voxel shape is determined by the exposure dose. (b) SEM image of a voxel array obtained by different exposure doses. Three ranges of voxels are fabricated correspondingly to the exposure time t_1, t_2 and t_3 whose corresponded doses are 0.9, 0.7 and 0.4 as indicating in (a). (c) Complete voxel lying on the substrate indicated an ellipsoidal form (exposure time t_1 was applied). This form is similar to that obtained by the TPA method.

up by joining individual voxels that are each exposed by a single-shot exposure, such that the structural feature (rod cross-section) is determined by the shape of these voxels. By changing either the excitation power or the exposure time, *i. e.* the dose, voxel size and shape can be adjusted. Note that, in order to obtain and to evaluate these small voxels on a glass substrate, we fabricated the same voxel array at different z-positions and with different exposure times. Only 2.5 mW of a continuous green laser is needed to create these structures, for an exposure time of about 1 second per voxel. Figure 4.4–(b) shows, for example, a voxel array fabricated with three different exposure times. The dose dependence can be explained theoretically by calculating the iso-intensity of the focusing spot at different levels. Three kinds of voxels obtained with t_1 , t_2 and t_3 as shown in Fig. 4.4–(b) correspond to three different iso-intensities,

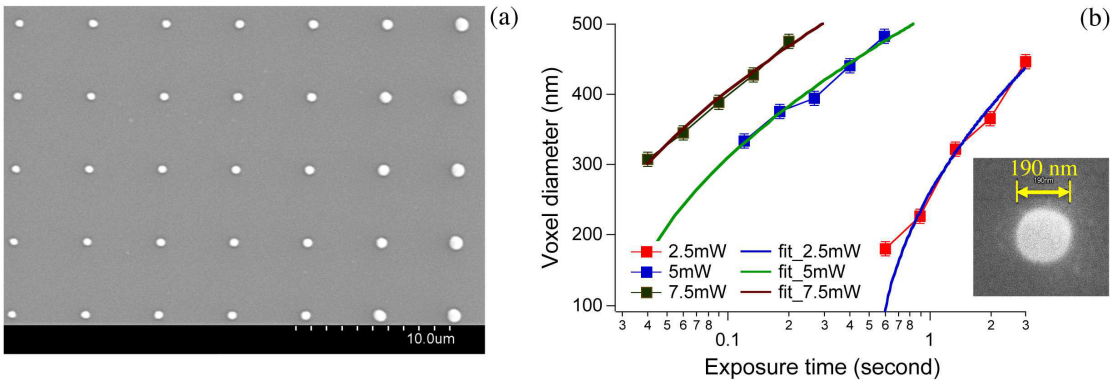

Figure 4.5: (a) SEM image of a voxel array fabricated at different exposure times and with $P = 2.5$ mW. (b) Exposure time dependence of voxel size, with different laser power values, $P = 2.5$ mW; 5 mW; 7.5 mW, respectively. The continuous curves are obtained by a tentative fit using the diameter-dose relationship for one-photon absorption. Insert shows a SEM image of a small voxel obtained with an exposure time of 0.5 second at a laser power of 2.5 mW.

namely 0.9, 0.7 and 0.4, respectively. The evolution of voxel size and shape observed experimentally fully confirms this operation in the OPA regime. Indeed, in the case of TPA, the creation of bone-like shape voxel, corresponding to that obtained with t_3, for example, requires very high excitation intensity and would not be easily realized due to TPA intensity threshold, as already mentioned above. In the case of LOPA, all these voxels shapes are obtained by simply adjusting the exposure time while keeping a low laser power. To obtain small voxels, shorter exposure times, t_1, for example, should be applied. Of course, the exposure time required to create submicrometer structures varies as a function of the laser power.

Figure 4.5 shows the voxels size as a function of exposure time for three values of laser power. The exposure time is changed finely around time t_1 as shown in Fig. 4.4–(b). A voxel with a size as small as 190 nm is obtained with, for example, a power of 2.5 mW and an exposure time of 0.5 second, as shown in Fig. 4.5–(b). The fabrication of smaller voxels is possible, but due to some limitations such as the quality of the instruments used (mechanical vibration, electric device, SEM, *etc.*) and also due to the poor adhesion of the small polymerized voxel on a glass substrate. We have not been able to obtain smaller structures, the size of individual voxels is quite small when considering the wavelength used for the writing process. As for the linear

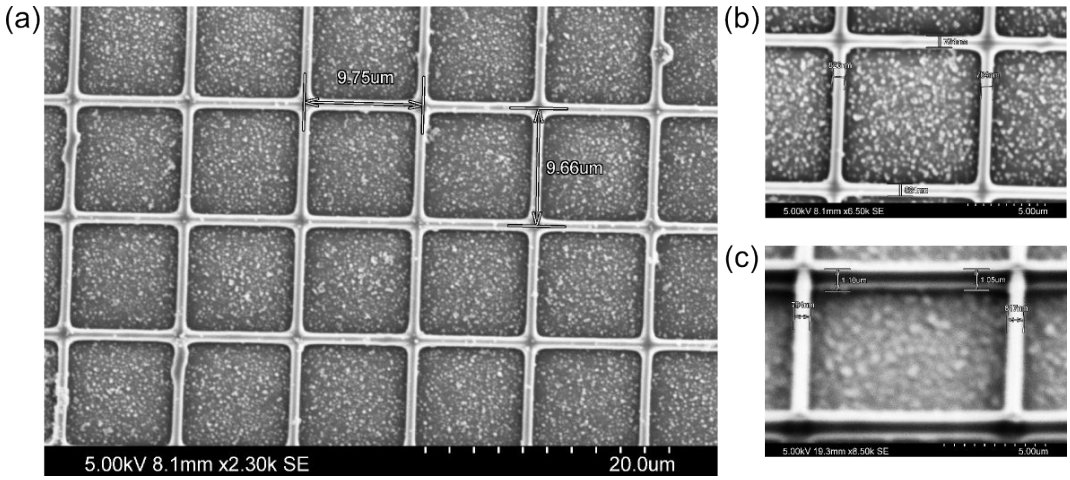

Figure 4.6: A 2D "Chess board"-like photonic structure fabricated by scanning the focusing spot along the x–axis and the y–axis (lines separated by 10 μm). Measured lateral diameter of rod (line width) is 800 nm in agreement with the one set by the program. Parameters: input power = 10.8 mW, scanning speed = 1.43 μm/s, film thickness = 2 μm.

dependence with intensity (OPA vs. TPA), the diameter-dose relationship agreement confirms this behavior, as we have used the intensity I_0 for our fit, instead of I_0^2 in the case of TPA.

The optimum dose for the smallest single voxel is used as standard dose for fabrication of 1D, 2D and 3D structures. For laser light of 532 nm wavelength and a microscope objective with NA=1.3, our result has shown the nealy elliptical cross-section of the voxel with an aspect ratio (axial diameter/lateral diameter) of about 2.8 (theory) and 3.0 (experiment). The absolute dimension of the voxels can be adjusted through the deviation of voxel standard dose of the laser beam, with higher doses leading to larger voxels.

Depending upon the size of the structure and on the desired line width of rods, the voxel standard dose can be altered to meet requirements. For example, 2D "Chess board" like PC structure shown in Fig. 4.6 was patterned on a 2 μm film. The line width of each individual rod was programmatically set to 0.8 μm, which is about 3.6 times of the voxel standard size. It is possible to increase the standard dose by $<3\times$ by either slowing down the scanning speed or by increasing the input power. Structure in Fig. 4.6 was done by applying the latter way, and shows that the resulted

size is uniform, around 800 nm. Increasing further the input power to get a thicker line width (or higher), *i.e.* 2 μm, is not a good solution (we shall discuss about this in chapter 5). In this case, the better result is obtained if writing side-by-side two or more parallel lines with a certain lateral shift (or axial shift along the z direction).

A 2D micropillars PC structure shown in Fig. 4.7 was fabricated using the same writing process as for CPC structure (shown in the previous chapter). In this pattern, the periodicity is 5 μm, the height of micropillars equal to the film thickness (2 μm) and only one third of the voxel standard dose was used. We notice that, the input power used for z axis patterning is quite different from that used for in-plane patterning. It is about 3× less compared to in-plane patterning. The reason is that, when the focusing spot was moving along the z–axis the SU-8 material within a vertical column (x= const, y=const, $z = z(t)$) receives much larger dose than in the in-plane case. As a result, if the same input power (of in-plane case) is used, then the obtained line width should increase by 2-3×.

All of the above examples is to demonstrate the nature of absorption of photons by SU-8 photoresist and the capability of LOPA DLW for the fabrication of submicrometer structures. In the next section we will experimentally demonstrate LOPA DLW for the fabrication of 3D PC structures.

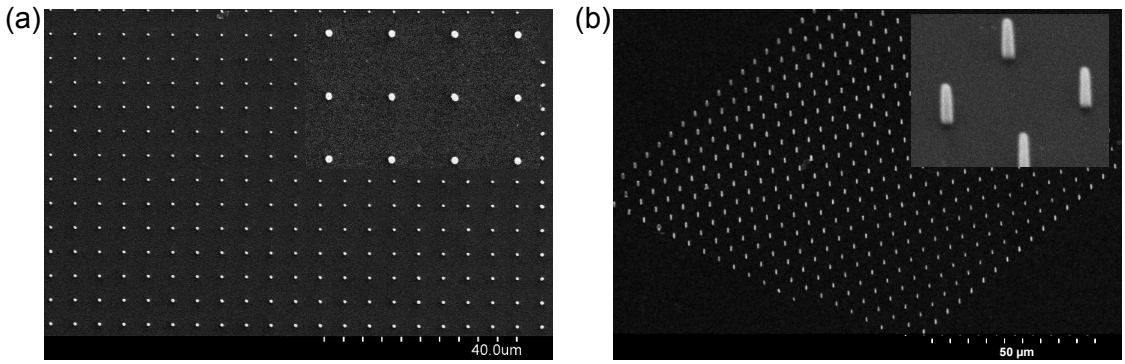

Figure 4.7: SEM images of (a) top-view and (b) side-view of a 2D micropillars PC structure. Focusing spot started to move from lower half space inside cover glass substrate to the upper half space in SU-8, and terminated in air. Measured diameter of micropilars is ≈ 600 nm. The periodicity is 5 μm, the height of micropillar equals to the film thickness of 2 μm. Input power was 5 mW, scanning speed of 1.43 μm/s.

4.2.2 Fabrication of three-dimensional PCs

Below we experimentally demonstrate LOPA DLW for the fabrication of 3D PCs. We will see that PCs fabricated by LOPA DLW are not only possible but also as good as those created by TPA DLW.

The fabrication of 1D and 2D structures is straightforward in which the scanning is performed either in the (xy)–plane or along the z–axis. The accumulative nature of OPA is only present when the separation is as small as the lateral diffraction limit of the optical system. In this case, although the accumulation effect exists when scanning is made along z, its effect on the quality of 2D structure is negligible. Differently, in 3D fabrication, the focusing spot driven by the translation system moves within the entire volume. In this case, broadening of the line width includes absorption not only from on-focus photon but also from a considerable number of off-focus photon during displacement. In other words, the resulted line width is an absorptive contribution of the overall 3D diffraction pattern. The broadening of the line width is large in a strong absorption regime but is really small in LOPA. Indeed, a successful fabrication of 3D PC is evidenced to demonstrate the LOPA idea.

In our experiments of 3D fabrication, the dose was adjusted by changing the velocity of the PZT movement while the input power is fixed. Doses are varied from structure to structure depending upon the size and separation (periodicity of PC). In the first experiment we fabricated a series of different size 3D woodpile PC structures on glass substrate. Sometimes, the resulted structure disappeared because of the poor adhesion of SU-8 structures to the glass substrate. But on the way of demonstration of the LOPA technique we decided not to use any kind of promoter to improve adhesion. We also noted that SU-8 exhibits a strong shrinkage effect which results in the distortion of the fabricated structures. After a number of experiments, we found acceptable parameters for woodpile structure, *i.e.*, an input power of 2.5 mW and a velocity of 1.43 μm/s. Applying these parameters, we were able to fabricated a series of 3D PC structures such as woodpile, twisted chiral and circular spiral.

Figure 4.8 shows a SEM image of a 3D woodpile PC fabricated by using these optimum fabrication parameters. The structure consists of 16 stacked layers. Each layer consists in parallel rods with period $a = 2$ μm. Rods in successive layers are

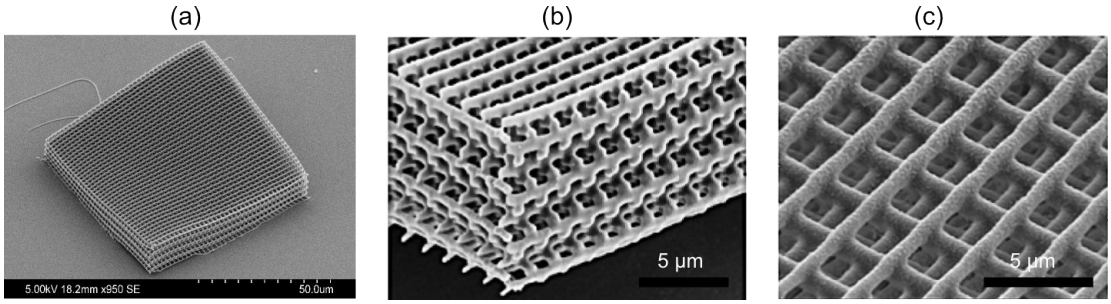

Figure 4.8: SEM image of a woodpile structure fabricated with the following parameters: distance between rods = 2 μm; distance between layers = 0.8 μm; number of layers = 16; structure size = $(80 \times 80 \times 12)\mu m^3$; laser power = 2.5mW.

rotated by an angle 90° relative to each other. Second nearest-neighbor layers are displaced by $a/2$ relative to each other. Four layers form a lattice constant $c = 2.8$ μm.

SEM measurement shows that the line width of rods on the top layer is ≈ 450 nm, it is about 1.5× of our voxel standard size. This means that the size of the rod can be minimized further. Indeed, Fig. 4.9 shows a SEM image of a woodpile structure with measured separation between rods on the top layer only of 0.9 μm and the measured line width was only ≈ 180 nm. This result shows evidently that separation of rods and layers are comparable to the wavelength of visible light. The structure probably has a photonic bangap but we were not able to measure this because of lacking equipments. We notice that our fabricated woodpile PC structure with small periods of the same quantity as that obtained by TPA DLW [100].

oreover, in comparison with the same structure obtained by means of TPA DLW in references [94, 101] this woodpile structure fabricated by LOPA DLW possesses even smaller feature size and period.

In second series of experiments for the fabrication of 3D chiral twisted PC, we used the same procedure as in previous series in order to find optimum fabrication parameters. The SEM image of the structure is shown in Fig. 4.10. This structure consists of stacked 28 layers of parallel rods. The distance between rods is $a = 2$ μm and the distance between two successive layers is $c/3 = 0.8$ μm. The length of the hexagon edge is $l = 25$ μm, the laser power $P = 2.8$ mW and the scanning speed = 1.34 μm/s. The measured line width of rods on the top layer is 294 nm; this width

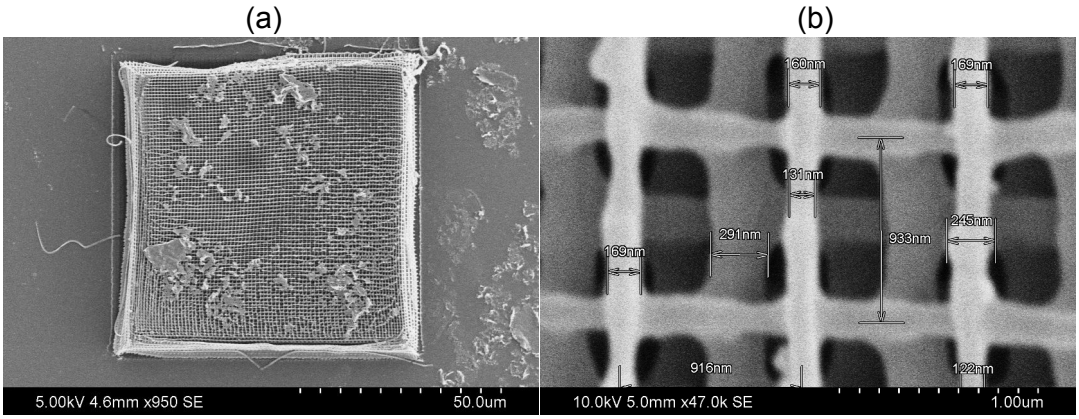

Figure 4.9: SEM image of a woodpile structure fabricated with the following parameters: distance between rods = 1 μm; distance between layers = 0.480 μm; number of layers = 16; footnote size = $(80\times80)\mu m^2$; laser power = 2.5 mW; scanning speed = 2.0 μm/s.

is 336 nm at the end of a rod near glass interface. These line widths are nearly the voxel standard size, and slightly decrease as a function of depth. Both shrinkage effect and absorption give rise to reduction of the line width and of the line length of rods on top of the structure. The latter is consistent with our calculation but for a depth of only 20 μm, the shortening is negligible. To improve the quality of this kind of structure one should find out a material with lower shrinkage effect than SU-8.

The chiral PCs fabricated by LOPA DLW shown in this experiment are the same as those obtained by means of TPA DLW in reference [102], except that our structure is free-standing and 4 layers larger than the structure in reference [102].

In the third series we fabricated 3D spiral PCs. The FCC lattice based circular spirals PCs (sketched in Fig. 4.11–(a)) consist of side-by-side vertically standing spirals. Each spiral has a pitch C, a diameter D and is made of rods with a cross section width w and length h. The fcc configuration is achieved by shifting adjacent spirals by half a period as they wind in the vertical $< 001 >$ direction. The lateral lattice constant a is twice of the distance between adjacent spirals and the vertical lattice constant is the pitch length C. A SEM image of our fabricated structure is shown in Fig. 4.11–(b). This structure consists of 20×20 spirals veridically standing on glass substrate. The parameters of this structures are as follow: diameter of a spiral $D = 2$ μm; spiral pitch $C = 2$ μm; lattice constant $a = 3$ μm; spiral height equals to film thickness = 15 μm; laser power = 2.6 mW and scanning speed $v = 1.34$ μm/s.

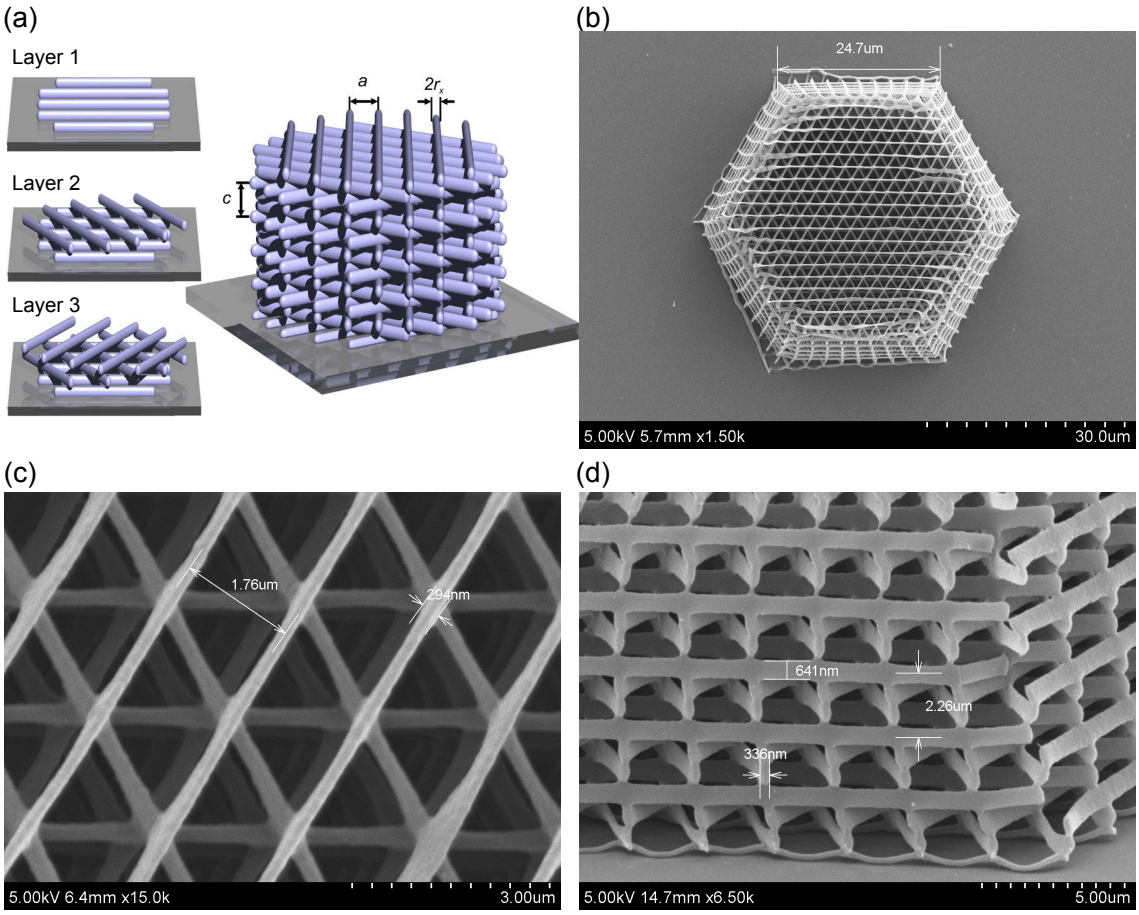

Figure 4.10: 3D chiral twisted PC fabricated by LOPA DLW. (a) Sketch of a 3D chiral twisted PC and its parameters together with the layer-by-layer construction during fabrication process. (b) SEM image shows a top-view of fabricated 3D chiral twisted PC. (c) A top-view magnification micrograph of the strucure in (b). (d) A side-view magnification micrograph of the structure in (b). Structure and fabrication parameters: distance between rods $a = 2$ μm; distance between layers $c/3 = 0.75$ μm; number of layers = 28; line width $2r = 300$ nm; laser power $P = 2.8$ mW and scanning speed $v = 1.34$ μm/s.

Measured line width is $w = 290$ nm at the center-top of the structure. The axial size of rod measured near glass substrate is 900 nm and near the top is 700 nm. In comparison with the same structure fabricated by TPA in Ref. [101], the structure in this experiment (by LOPA) is free-standing and possesses smaller and smoother rods.

Through experimental results of all above examples, we observed the same trend leading to preliminary conclusions: (i) 3D PCs were successfully fabricated by means of LOPA DLW. The obtained results are as good as those obtained by TPA DLW. The

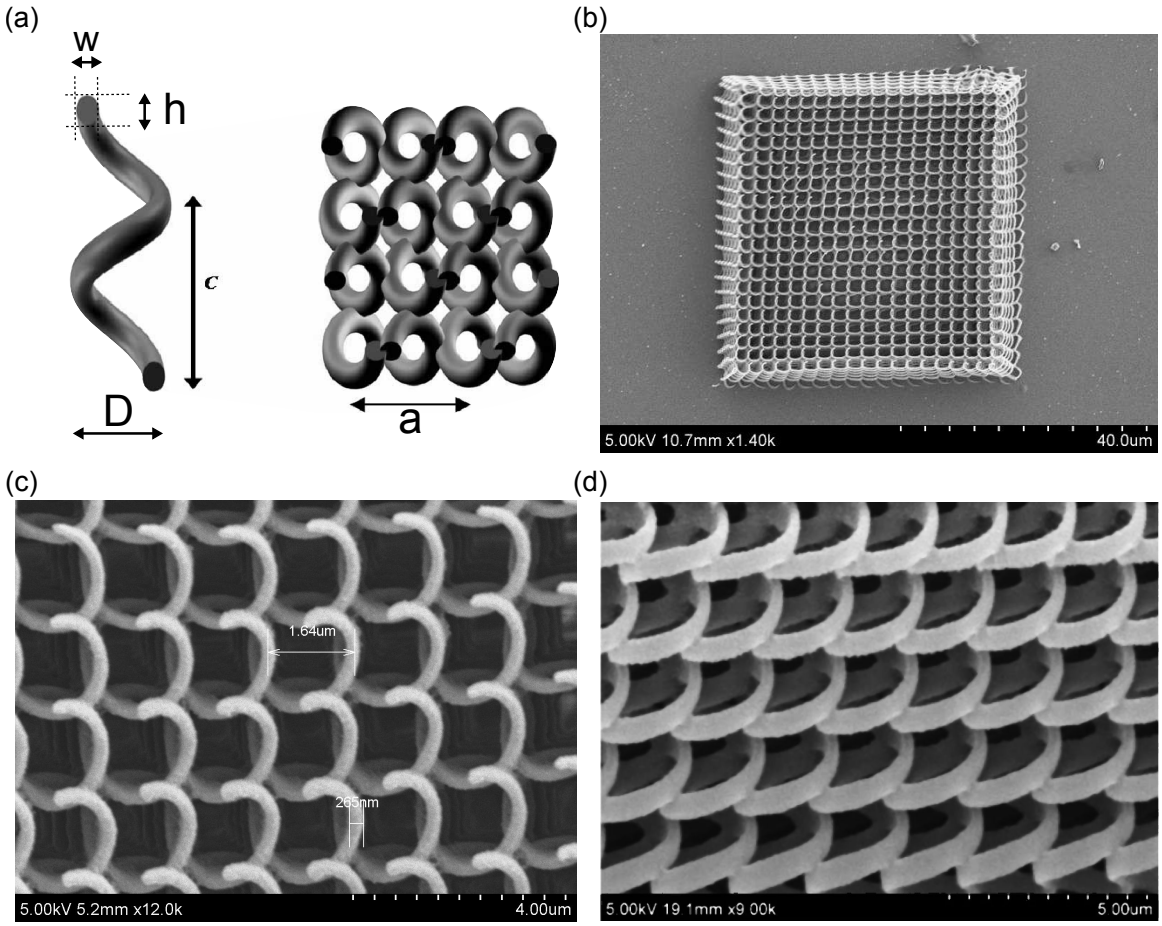

Figure 4.11: 3D spiral PC fabricated by LOPA DLW (a) Sketch of a spiral and its parameters together with an array of 4 x 4 spirals that are arranged in a FCC lattice. The lattice constant a is twice the distance between adjacent spirals. Each spiral has a pitch C, a diameter D and is made of rods with a width w and a length h. (b) SEM image of fabricated structure. Structure and fabrication parameters: diameter of a spiral $D = 2$ μm; spiral pitch $C = 2$ μm; lattice constant $a = 3$ μm; spiral height equals to film thickness = 15 μm; laser power = 2.6 mW and scanning speed $v = 1.34$ μm/s.

smallest feature size reaches 150 nm corresponding to the smallest lateral cross-section of rod (woodpile, Fig. 4.9). The best quality of the fabricated structure is obtained when the line width of rods is about that of the voxel standard size (lateral and axial cross-section size is about 220 nm and 680 nm, respectively. The corresponding aspect ratio (axial/lateral) is about 3. To achieve this specification, the recommended input power and scanning speed is around 3.0 mW and 1.5 μm/s. (*ii*) The fabricated structure appeared to be shrunk to some extent, varying upon the line width and the

height of the structure. The shrinkage effect due to the material is the main factor, the second cause is attributed to the attenuation of light intensity as a function of depth. This effect confirms the nature of OPA.

So far, we have experimentally demonstrated LOPA microscopy through LOPA DLW. The fabricated structures were without artificial defect. In the next section we will show that by means of LOPA DLW, any structures with controlled defects could be fabricated.

4.2.3 Fabrication of PCs with defect and arbitrary structures

In the DLW technique, the fabrication of PC with defect and arbitrary structures is just a problem of programing. Indeed, to design a defect inside a PC, we designed a "defect" in the programming code (G-language, Labview) where the code can simultaneously order the PZT (via controller) and electric shutter to perform the task. The control of shutter is for adjusting the exposure time correspondingly to the current position of the PZT. We also can program the velocity of the PZT displacement to be faster or slower. All the programming task is to adjust the exposure time to make the structure element (dot, rod, spiral, *etc.*) at the current position to obtain controlled number of photon from the laser beam.

Taking an example, the letter "LPQM" in the structure shown in Fig. 4.12–(a) is a kind of cavity defect in PC. Circular spirals are omitted to create the letters. The

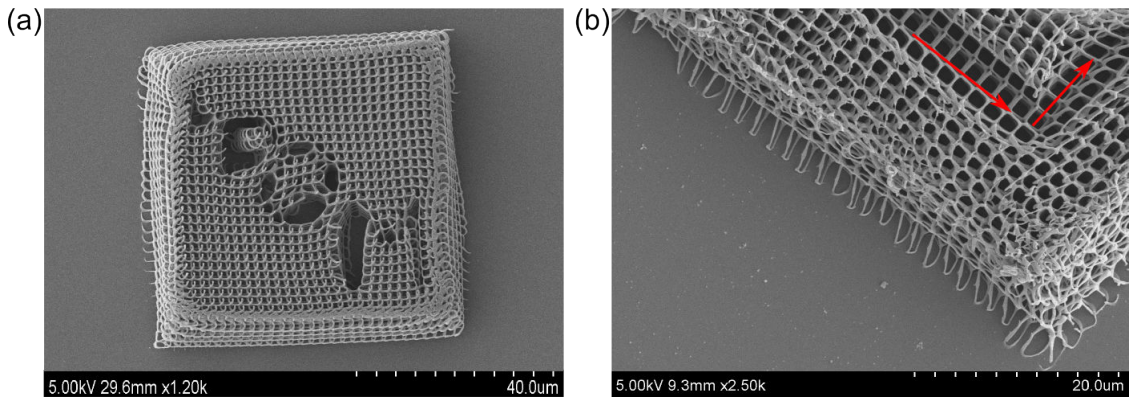

Figure 4.12: SEM images of PCs with defects: (a) Letter "LPQM" defect in a circular spiral PC and (b) a "L"-like waveguide defect in square spiral PC.

defect in the structure in 4.12–(b), is a kind of waveguide defect in a square spiral PC. The waveguide was designed on top of the structure by just shortening the height of three (along one side) and two (along the other size) square spirals in the (xy)–plane by the length of three pitches from the top.

In a structure as shown in Fig. 4.13, a waveguide defect was engineered inside the body of the structure, the input and the output are denoted by red arrows. In this structure, all spirals along the waveguide were shortened by a length of one pitch at the beginning.

Now we consider a quite different case, where the structure to be fabricated is volumetric object, *i.e.* a micro-cow or a micro-Eiffel tower. To do so, it is worth to distinguish two types of writing process, the first one (which is related to all experiments in previous section) is called "path scanning" and the other one is called "volumetric scanning", which is used in this section. In "path scanning", the focusing spot of the laser beam is moving along a path leaving behind its polymerized trace. These traces are then completely solidified during the subsequent post-exposure baking resulting in a structure made up by rods. The size and shape of rod is completely defined by the focusing spot of the laser beam. This writing process is popular in what the PC is fabricated. "Volumetric scanning" deals with an abstraction of shape, a representation of an object by a sparse set of planar elements that define cross sections

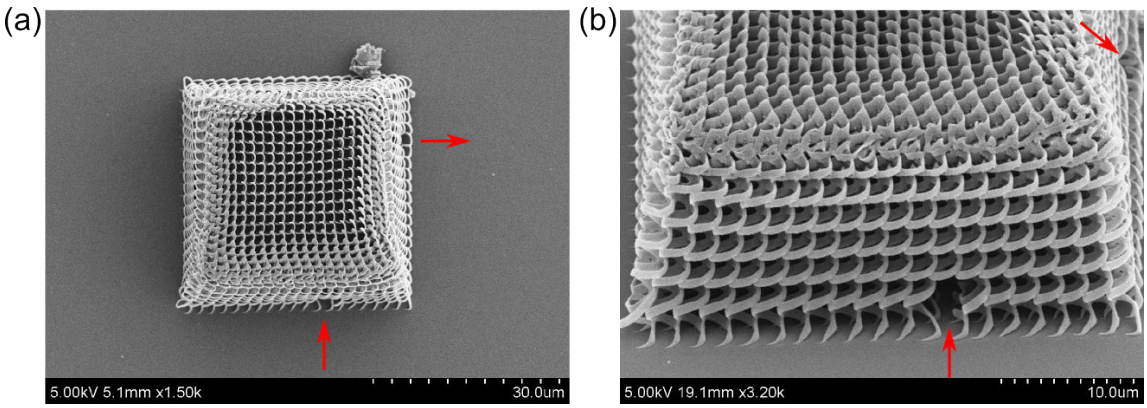

Figure 4.13: 3D circular spiral PC fabricated with waveguide defect. A "L"-like waveguide defect is introduced inside the body of the structure by shortening a pitch long at the beginning of the spirals along the designed waveguide. Red arrows denote the waveguide location, the input and the output.

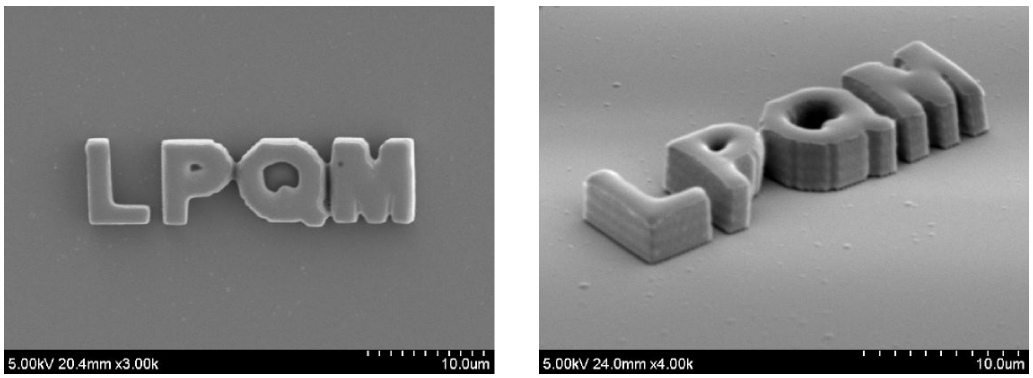

Figure 4.14: The "LPQM" structure was patterned on a 5 μm SU-8 film with an input power of 2.3 mW and a scanning speed of 10 μm/s. For the fabrication of this structure, the "volumetric scanning" was applied.

through the input object at different positions and orientations. In the algorithm, the model of the object is numerically sliced into many parallel cross-sections. In each cross-section only data along the shape are sampled. The sampled dataset is then converted into a format that is readable by the LabVIEW code. Finally the PZT performs scanning slice-by-slice, only along the shape, from the first slice (normally below the glass-photoresist interface) until the 3D object is completely imaged in photoresist. This "volumetric scanning" finally becomes the "path scanning" literally. This writing process is common in 3D printing and 3D patterning by means of TPA DLW. As a demonstrative example, we fabricated a "microletter" structure. The letter "LPQM" firstly was modeled by a CAD system. Data were then exported to STL extension data file, converted into individual DXF files using RP software and imported into an executable Labview code. At this state, Labview reads coordinate data point x, y, z and send it one-by-one to the PZT controller. After patterning, the patterned sample was subjected to a PEB followed by a chemical development step as usual.

4.3 Conclusion and prospects

We have developed a simple, high-resolution laser writing process in a one-photon absorption regime in a weakly absorbing photoresist material, namely low one-photon absorption microscopy (short term: LOPA microscopy) then applied for direct laser

writing (short term: LOPA DLW). The LOPA DLW is a novel technique, which enables the fabrication of very small single objects and of 2D and 3D periodic structures such as photonic crystal. The idea of using ultra-low one-photon absorption opens a new and inexpensive way to address 3D structures, namely 3D fluorescence imaging and 3D fabrication.

We derived three main requirements of LOPA microscopy are:

1. Low or ultra-low one-photon absorption,
2. Optical aberration-free,
3. Strong focusing.

Satisfying the first requirement allows light penetrate deeply into material with negligible loss. Satisfying the second requirement allows the focusing spot to retain its size and shape (hence intensity will not much change) when traveling inside the material. Satisfying the third requirement permits light be strongly focused into a tiny volume. Once the three requirements are satisfied, the focusing spot possesses very high intensity confined in a diffraction-limited volume and traveling freely within the material with very low loss. In DLW, the energy loss of the laser beam due to the material takes play only at the focus due to polymerization reactions.

We demonstrated LOPA DLW by a number of experiments, in which 1D, 2D and 3D PCs are fabricated. In terms of quality of the structures fabricated by LOPA DLW, we have shown that these structures fabricated by LOPA DLW are the same as those obtained by TPA DLW.

Since the requirements for realizing LOPA microscopy are trivial and straightforward in practice, LOPA microscopy emerges as the first simple and low-cost technique for fabrication of any sub-micrometer structures for a broad range of applications, especially for PCs. However, LOPA microscopy shows some inherent drawbacks, which may limit the quality of the fabricated structures. Dealing with these drawbacks and proposing a technique for improvement is the main objective of the next chapter.

Chapter 5

Optimization of LOPA-based direct laser writing

Being a consequence of linear behavior of absorption mechanism, the dose accumulation effect is the inherent nature of linear absorption material [103, 104]. In contrast to a conventional TPA method, a photoresist operated in OPA regime doesn't exist any threshold of polymerization [105–107], hence the voxel size can be controlled by adjusting the exposure dose. In principle, polymerization occurs at the focusing spot with a single-shot exposure resulting in a very small voxel (smaller than the diffraction limit) [108]. However, when two voxels are built side-by-side with a distance of about several hundreds nanometers, two resulting voxels are no longer separated [103, 109, 110]. This issue evidently originates from the dose accumulation effect in OPA process.

In order to get better resolution and better uniformity of the fabricated structures, besides of many current techniques for manipulating the voxel itself [103], one also looks for a way to compensate the dose accumulation effect [111, 112]. This chapter deals with the origin of the effect and propose a compensation technique for getting better structural uniformity. We demonstrate the dose accumulation effect and our strategy by both theory and experiment. We propose a technical way to get rid them out of the system, in order to get higher structural resolution.

5.1 Dose accumulation effect

Experimental realization of LOPA-DLW in fabrication of 1D, 2D and 3D photonic crystal shown evidently the advantage of LOPA idea in combining with regular DLW. That, only few milliwatt of a CW laser and in a moderate time, any kind of sub-micrometer structure with of without designed defect could be fabricated. However, we found that some fabricated structures are not uniform or distorted. The physical causes of the distortion can be attributed to 2 main effects: *shrinkage effects* [113], and *dose accumulation effect* [112].

Figure 5.1–(a) shows a micropillar structure which is distorted by shrinkage effect - the pillars at the edge of the structure tend to collapse towards to the center reducing the size of the structure at the top. The reason is that, the shrinkage effect leads to residual stress of the structure and be more pronounced at the free-ends (the top, edge faces). SU-8 photoresist used in this thesis is just an example since it exhibits a really low absorption at the chosen wavelength. We can use any other kind of photoresist instead of SU-8 in order to efficiently reduce the shrinkage effect and to get high quality of the final structures.

The effect due to dose accumulation is the main cause of the distortion in all structure fabricated by LOPA DLW. The origin of the effect comes from the accumulative nature of linear absorption. Indeed, in OPA fabrication, voxel formation is a liquid to solid transformation process. This process is linearly proportional to the intensity of the excitation light. The degree of polymerization within the focusing spot (being to form a voxel) as well as at out-of-focus region are completely defined by the number of photon, which are present at the volume of interest. Although isolated voxel fabrication is ideally confined to the focal volumetric spot, the superposition of many out-of-focus regions of densely-spaced voxels leads to undesired and unconfined reaction. As a result, if voxels are made side-by-side and distances between them are about diffraction limit, the accumulated out-of-focus leads to the degree of polymerization in the space between vowels become comparable with the main in-focus one resulting in a formation of many interconnection wires. This effect also appears and being more pronounced as a function of exposure dose. Since the accumulative nature

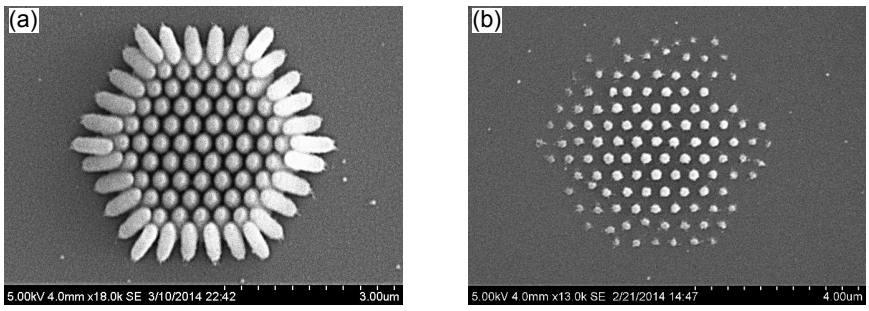

Figure 5.1: *Shrinkage* is more pronounced at the free-ends of the structure. In this structure, the micropillars at the edge tend to collapse to the center resulting in the size of the top part is less than at the bottom part.

is a process of no-degree-limitation, the polymerization reactions continuously take place until the entire volume becomes hundred percent exposure to the light, resulting a completely solidified block of the sample.

In what follows we will investigate the dose accumulation effect of OPA in DLW in both theory and experiment.

First we verify the accumulate nature of LOPA by following experiments. We consider a situation where a single exposure (a single-shot) is made, it may result in a single voxel with the size defined by a volume within which the spatial exposure dose is above a solidification threshold. That has been confirmed experimentally in the LOPA fabrication technique (voxel size $\approx$ 190 nm $\times$ 190 nm $\times$ 580 nm) as we seen in Fig. 4.5 of chapter 4. Now, we make a further shot by the side of the first single-shot in order to observe what is going on when two focusing spots are very close to each other. Similar with OPA microscopy where the microscopy image can not resolve two small objects which localize at about several hundreds nanometers from each others, the fabricated voxels in DLW also cannot be separated. Abbe's criterion states that, the minimum resolving distance of two objects is defined as $0.61\lambda/\mathrm{NA}$, where λ is the wavelength of incident light. This diffraction barrier thus imposes the minimum distance between different voxels, created by different exposures. Moreover, when multiple exposures are applied, even with a distance far from the diffraction limit, the energy of this exposure will contribute to others, and the effective voxel size consequently increases. Indeed, in the case of OPA, photons could be absorbed anywhere they are, with an efficiency depending on the linear absorption

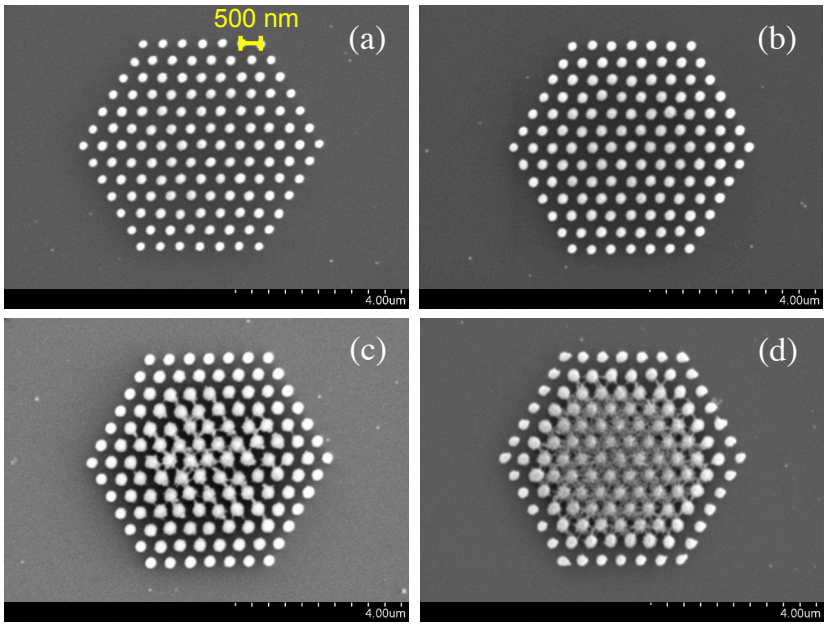

Figure 5.2: Dose accumulation effect of LOPA technique, realized with $d = 0.5$ μm. In each structure, the dose, which is proportional to power and to exposure time, is kept constant for all voxels. The dose (power= 2.5 mW) is increased for different structures from (a) to (d).

cross-section of the irradiated material. The absorbed energy is gradually accumulated as a function of exposure time. A symmetric micropillar pattern fabricated with very short lattice constant near diffraction limit is the best for representation of accumulation effect. Figure 5.2 shows the evidence of the variation of voxels size (in the micropillars structures, the diameter of a micropillar is also defined as a voxel size) of different patterns fabricated with different exposure doses. Note that in each pattern the exposure dose applied for a single-shot is kept constant so that we can directly compare the lateral size of voxels from voxel to voxel and from center to the outermost ring in the hexagonal pattern. The dose accumulation effect is very clear with high exposure dose, due to the out-of-focus polymerization predominated by the overlapping of second- or first-order diffraction rings of the diffracion pattern, in analogy to those of well-known Airy disk. At higher exposure dose voxels are randomly linked to each other by small interconnection wires. It is more pronounced when space between components approaches the LOPA's fabrication limit.

To be more clear, we perform some calculations of the same situation using Matlab

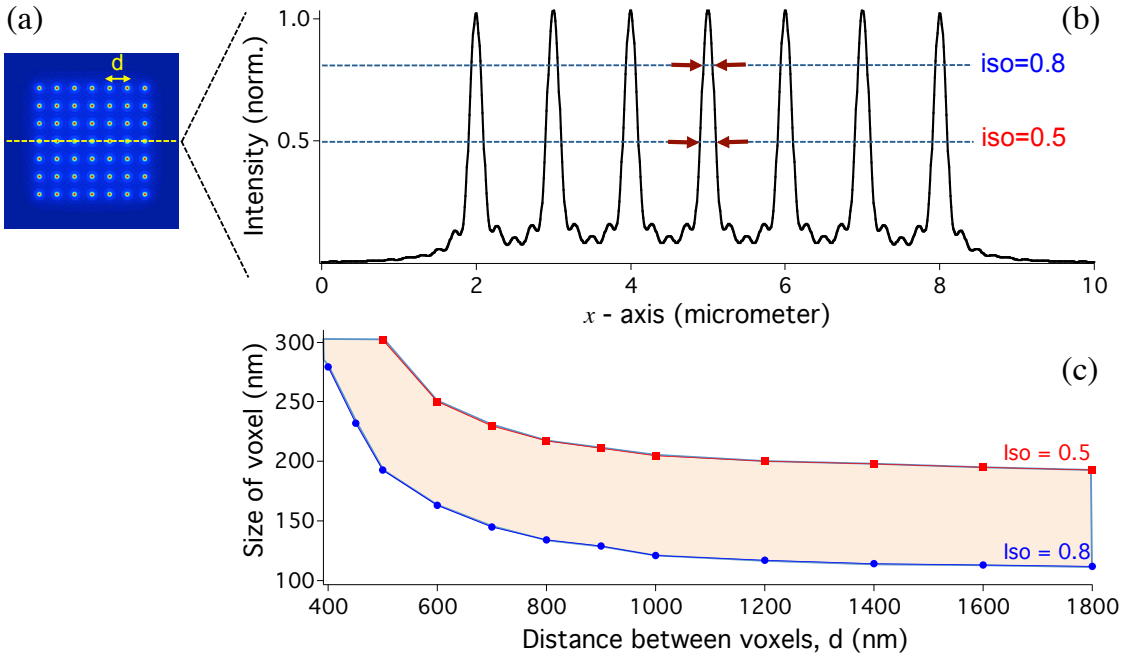

Figure 5.3: Theoretical calculation of the dependence of voxels sizes on the separation distance d between voxels, showing the influence of energy accumulation from this focusing spot to others. (a) Simulation image of a square pattern (7×7) with d = 1 μm. (b) Intensity distribution along x–axis, corresponding to the dashed line shown in (a). (c) Size of the voxel located at the center of the structure, calculated at different iso-intensities, as indicated in (b). The voxel size, theoretically estimated to be in the range represented by "yellow" color, increases when the distance between voxels decreases, in particular when d approaches the diffraction limit distance.

simulation and results are shown in Fig. 5.3. The dose accumulation effect related to the distance of the voxels is made. In this simulation the normalized time-average electric density is calculated, which is supposed to adequate to linear absorption in OPA case. In order to take into account the dose accumulation effect we coherently add all amplitudes contributed by every single-shot to the one of the current position. We derive the full width at half maximum (FWHM) corresponding to each position. This value is assumed to reflect the exposed volume in the photoresist via OPA and thus the shape of the corresponding focus. Instead of using FWHM as the figure of merit in our calculation we can consider any iso-intensity level. In OPA DLW an iso-intensity is supposed to result in an voxel with the corresponding size. For visualizing we draw two such level of $iso = 0.5$ and $iso = 0.8$. Curve fitting gives

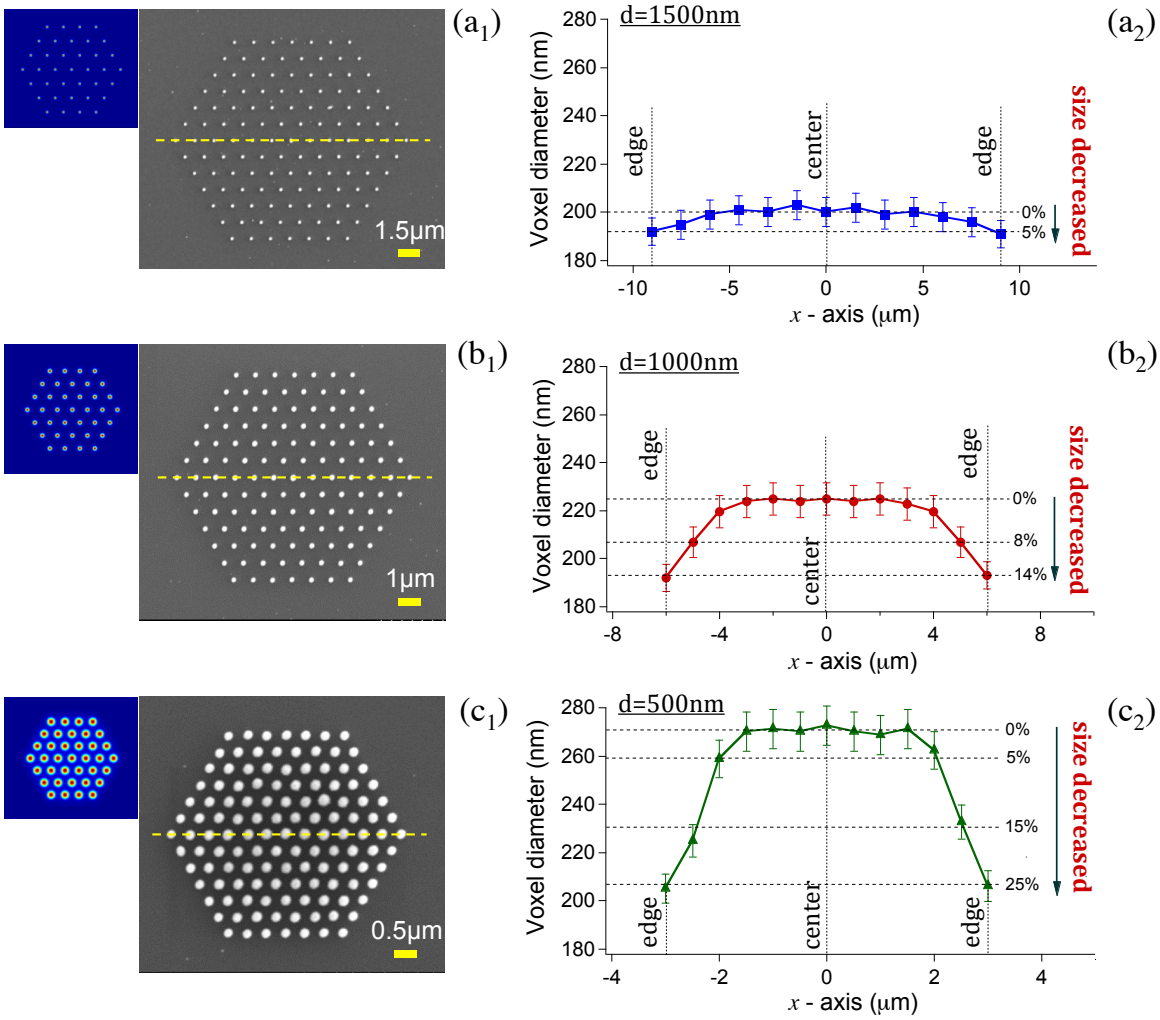

Figure 5.4: Experimental results showing the dependence of the voxels size on the voxels distance. SEM images of structures obtained with $d = 1.5$ μm (a_1) ; $d = 1$ μm (b_1), and $d = 0.5$ μm (c_1). On the left: theoretical images of corresponding structures. On the right [(a_2), (b_2), (c_2)], the diameters of different voxels, aligned on the dashed lines of SEM images, are plotted as a function of their positions along x–axis.

information of the width at each *iso*, we bring it up in the subfigure at the bottom of Fig. 5.3. Clearly, accumulation effect is pronounced when two voxels are separated by a distance shorter that 1 μm, resulting in larger size of the voxels. The FWHM of each voxel increases from 190 nm to 300 nm when the separation reduces from 2 μm to 0.5 μm. Moreover, for a short separation, the voxels array is not uniform from its center to the edge part.

Figure 5.4 shows the experimental evidence of this accumulation effect as a function

of separation distance (d). The voxel size changes up to 25% between voxels at center and at the edge of structure for the case of $d = 500$ nm (see the figure's caption for detail). We believe that small and uniform voxels with very short separation are possible, but a proximity correction, *i. e.*, a control of exposure time or power and a compensation of the doses between different voxels, should be applied.

5.2 Optimization strategy

According to the structures fabricated by LOPA DLW and the theoretical calculation, the dose accumulation effect should be compensated in order to get better uniformity of the structure. The compensation technique idea is based on balance of the exposure doses over the structure. In other words, a certain amount of the exposure dose should be reduced at the region (or a part or a division) where the dose accumulation effect strongly occurs and should be added to the region (or a part or a division) where the dose is lacking. For example, in Fig. 5.5 we depict a 2-D hexagonal pattern of voxels, which presents an accumulation effect at some extent. The exposure dose D_i obtained by voxels gradually decrease from the center to the edge of the pattern, $D_1 < D_2 < D_3 < \ldots$. Here the exposure dose $D_1, D_2, D_3, \ldots$ can be calculated by a

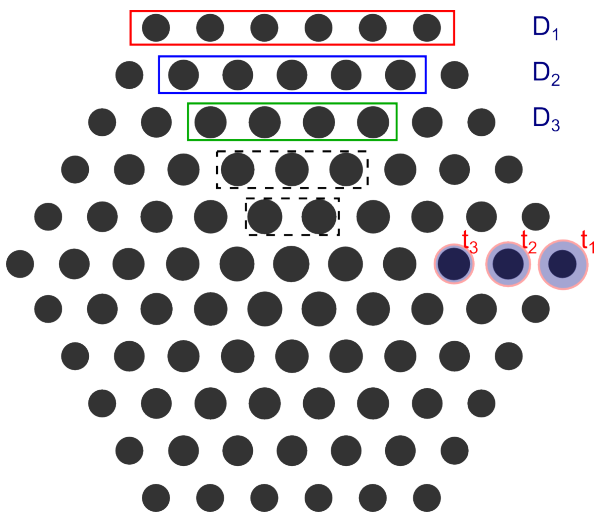

Figure 5.5: Optimization strategy of the structure fabricated by LOPA. The dose D1, D2, D3 are compensated by increasing the exposure time (with fixed power) according to $t_1 > t_2 > t_3$.

simulation as we described above. It is easier to normalize these to the dose at the center voxel $D_{(O)}$ we obtain $\overline{D}_1, \overline{D}_2, \overline{D}_3, \ldots, 1$. Evidently, these normalized dose are proportional to the input power and the exposure time. In experiment the laser power is usually fixed, we can alter the dose by just make the exposure time shorter or longer depending where we want to adjust. In turn, exposure time can be propositionally related to the scanning speed of the PZT movement.

Now we want to compensate the "thinner" part of the pattern at the edge relative to the "thicker" of the pattern, the calculated dataset of exposure time $(t_1, t_2, t_3, \ldots,)$ with $t_1 > t_2 > t_3, \ldots,$ or in scanning speed expression $v_1 > v_2 > v_3 \ldots,$ are applied. By doing this we expect to obtain a uniform compensated pattern since the dose accumulation effect has been compensated over the structure.

The same idea can be applied in fabrication of higher dimension. In fabrication of 3D photonic crystal where a layer-by-layer writing process is usually made the compensation technique is applied for each layer for two first dimension (in (xy)–plane). The compensation can be done for the third dimension (along z–axis) by decreasing a certain amount of writing speed relative to one of the first layer (which is in contact with the substrate) from layer to layer accordingly to the depth of the current layer from the interface. At this step we can also taking into account the other effect such as the shrinkage as well as the focus shift to enlarge (in (x-y) plane) and shrink (along (z)–direction) by an appropriate amount of deviation.

5.3 Experimental demonstration

By changing either the input power or the scanning speed, the micropillars diameter can be adjusted. In most experiments, the input power was kept at 2.5 mW

As demonstrated above, the dose accumulation effect depends on the separation distance, d. In order to demonstrate the dose accumulation effect and the dose compensation technique, we scanned the focusing spot along the z–axis to fabricate 2D micropillars array, instead of 2D voxels array. We have systematically investigated the variation of the micropillars size as a function of separation d, from $d = 0.3$ μm to $d = 3$ μm. According to the micropillars size variation, from the center to the edge of the structure, we proposed to compensate the size difference by increasing

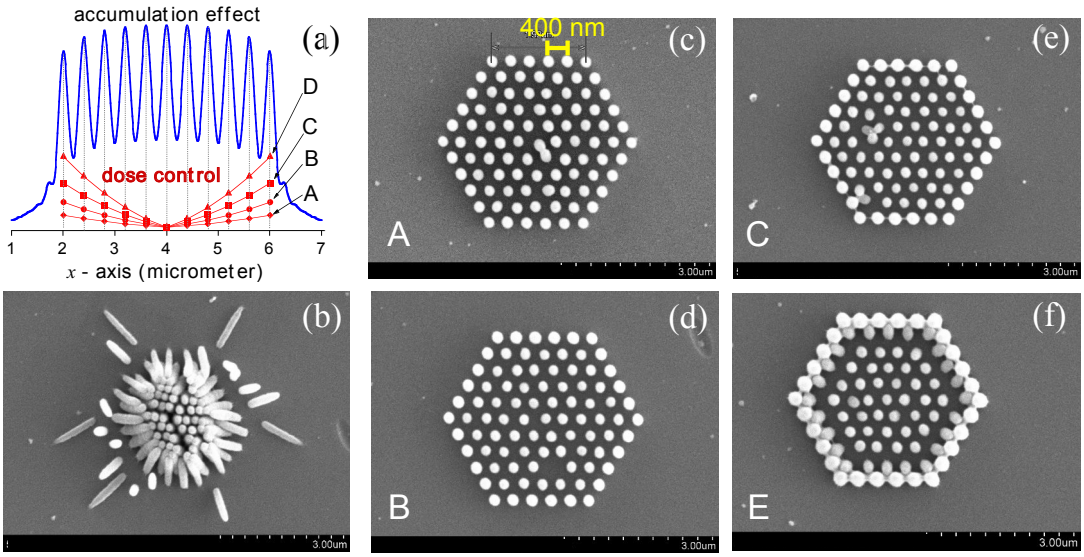

Figure 5.6: Demonstration of dose compensation technique for $d = 0.4$ μm. (a) Theoretical calculation of the intensity distribution as a function of x–position (blue color), and control of doses with different ratios, indicated by A, B, C, and D (red color) to compensate the dose accumulation effect. (b)-(f) SEM images of 2D hexagonal structures realized without compensation (b), and with compensation with different dose controls: A (c); B (d); C (e) and D (f). The excitation power was fixed at 2.5 mW and the dose was adjusted by changing the scanning speed of focusing spot.

gradually the exposure doses for outer micropillars. Figure 5.6–(a) shows the intensity distribution of a micropillar array and the dose compensation strategy. Different dose compensation ratios, indicated by letters A, B, C, and D, have been experimentally applied. Two sets of structures have been side-by-side fabricated on the same sample in order to maintain the same experimental conditions: the ones without compensation and the others with dose compensation. Figure 5.6–(b) shows the dose accumulation effect in the case of $d = 0.4$ μm, obtained without compensation. The structure is not uniform, and the outermost voxels are too small and are washed out or collapsed into micropillars in the center. With dose compensation, *i. e.* increasing the dose for outer micropillars, 2D micropillars arrays become uniform and stand up correctly. Figures 5.6–(c)-(f) show the structures realized with different dose ratios, corresponding to A, B, C, and D schemes, shown in Fig. 5.6–(a). With high dose compensation amplitude, the size of outermost micropillars even becomes larger than for those in the center, as shown Fig. 5.6–(f). By using an appropriate dose compensation amplitude,

perfect uniform 2D micropillars array is obtained, as shown in Fig. 5.6–(c). The structure period is only 400 nm, the height of micropillars is about 1.250 μm, and micropillars diameter is about 260 nm. Structures with period as small as 300 nm, and with diameter approaching 100 nm were also fabricated, but most micropillars were collapsed or washed out because of the poor contact between structures and glass substrate. These structures with periods of several hundred nanometers are very suitable for photonic applications in visible range.

We note that this technique was also applied for the fabrication of other 2D structures with a submicrometer period containing an arbitrary defect, such as a microcavity or a waveguide of arbitrary shape (for example, a Y – conjunction). In such case, the dose was controlled for individual voxel (or pillar) as a function of its position with respect to the defect and to the center or the edge of structure. The dose compensation is controlled for different structures, and many attempts have been tried to find out the optimized parameters. We believe that this dose compensation technique could be also applied for the fabrication of 3D structures with submicrometer period. However, for such structures, we should take into account the shrinkage effect, which is quite strong in case of SU8 photoresist and difficult to control.

5.4 Discussions and conclusions

We have theoretically and experimentally investigated the dose accumulation effect raised in this LOPA DLW technique. It is evidenced that when the lattice constant of structures is reduced and approaches the diffraction limit (several hundreds nanometers), the fabricated structure becomes non-uniform. We have then implemented a proximity correction technique, *i. e.*, a compensation of the dose between different voxels located at center or edge areas of the structure, which allowed to create uniform submicroscopic structures with a lattice constant as small as 400 nm. This strategy could be also applied for the fabrication of 3D structures with a small period, showing a great advantage of LOPA technique comparing with the commonly used two-photon absorption method.

Chapter 6

Coupling of single fluorescent nanoparticle into polymeric microstructures

In this chapter we investigated the coupling of a single fluorescent nanoparticle (NP) into a polymer-based photonic structure (PS). The coupling is accomplished through a double step of the low one-photon absorption microscopy. We will demonstrate theoretically and experimentally how this coupling allows to enhance the fluorescence signal of single NP.

6.1 Introduction

Recently, the concept of PCs containing active molecules or fluorescence nano-ojects has drawn a great interest due to their wide range of applications. Many kinds of NPs have been investigated in coupling to host PCs. For instance, self-assembled quantum dots embedded in a distributed Bragg reflector cavity structure, or in a micropillar for realizing a solid-state single photon source [35, 37]; a nitrogen-vacancy color center embedded in integrated devices towards room temperature quantum cryptography, quantum information processing, and cavity quantum electrodynamic [27, 114]; a gold NP coupled with a cavity system [36, 115] for plasmonic applications. Although the NP/PS coupling has been intensively investigated in both theory and experiment,

the fabrication of such kind of functionalized microsystem still remains a significant challenge. Actually, most NP coupled structures have been created in inorganic or semiconductor materials requiring complicated and quite expensive techniques.

LOPA microscopy with single laser-multitasking feature enable the NP/PS coupling to advance in an easier way. Below, through an demonstrative example we emphasize how single laser-multitasking feature can be done for any kind of emitter being to couple to an arbitrary polymer-based PC.

6.2 Coupling of single nanoparticle into microstructures

As a demonstrative example, we use Au NPs as an nano-emitter to couple to a polymeric microsphere. The description is as follows. The experimental set-up that has been shown in Fig. 3.1 of the chapter 3 is employed in this demonstration. In the setup, a continuous wave laser operates at wavelength of 532 nm was used for either mapping and fabrication (single laser). A microscope objective lens (OL) (Fluar 100x/Oil/1.3NA, Zeiss) placed beneath the glass coverslip is used to focus laser beam. The photoluminescence (PL) signal is collected by the same objective, filtered by long-pass filter before reaching a avalanche photodiode, and spectrally analyzed by spectrometer (Ocean Optics).

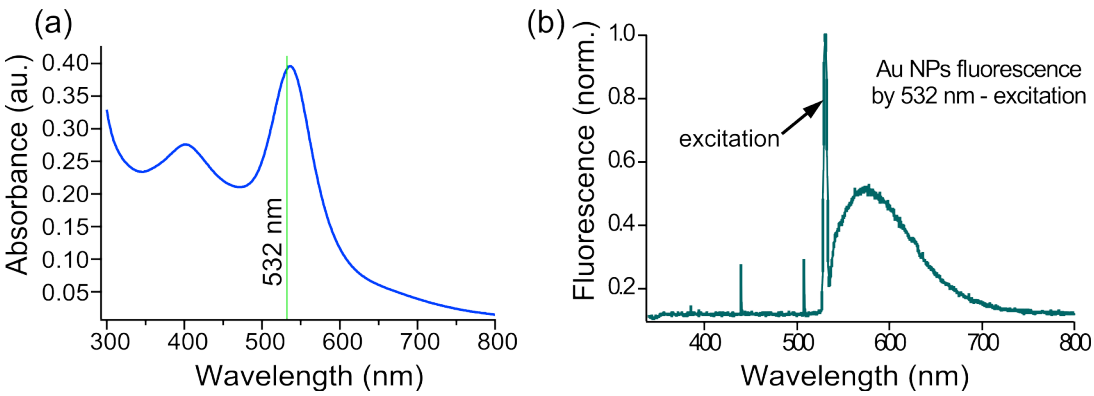

Figure 6.1: Absorbance spectrum of 50 nm gold nanopartice in water. The plasmon resonance peak achieved at wavelength of $\sim$ 539 nm. (b) fluorescence spectrum of Au NPs, excited by a CW laser at 532 nm

6.2.1 Characterization of gold nanoparticles

The 50 nm-diameter Au NPs used in this chapter are brought from Sigma-Aldrich Corp. The absorption spectrum of Au NPs in water is measured and shown in Fig. 6.1–(a). The plasmon resonance peak appears at 539 nm. In our investigation, a green laser of 532 nm is ideal to excite the localized plasmon resonance of Au NP, promising a large of interesting phenomena of Au NP/microsphere structure. Figure 6.1–(b) shows the fluorescence of Au NPs in water by an excitation light at 532 nm. By using a 580 nm long-pass filter, all the photons with wavelength larger than 580 nm are supposed to be collected by the OL of the DLW setup.

6.2.2 Au/SU-8 sample preparation

The sample used in this experiment consists of a thin layer of Au NPs sandwiched between two SU-8 phororesist layers. Figure 6.2 shows our procedure for preparation. First, we spin-coat the first SU-8 2000,5 photoresist layer on a cleaned cover glass. Then a Au NPs layer is spin-coated on the first SU-8 layer. Last, a second layer of SU-8 is spin-coated on the top of the Au NPs layer so that all Au NPs are immobilized in SU-8 photoresist. In order to achieving a desired film thickness, SU-8 2000,5 and SU-8 2002 were mixed together at appropriate ratio. Sample after each step is suffered a soft-baking process on the hot plates (65°C for 3 min. and 95°C for 5 min.). The film thickness between $1.0-2.0$ μm and good surface profile confirmation were subsequently examined by a profilometer. All steps were done in the clean room.

6.2.3 Mapping single gold NP embedded in SU-8

The first step consists of localizing the Au NP structure embedded between two SU-8 layers. The fluorescence images of Au NP were obtained by raster scanning the sample through the focusing spot. According to the absorption spectrum measurement of Au NP structure shown in Fig. 6.1, a very low excitation power (less than 0.1 mW) was employed. This power is weak enough not to induce any polymerization of SU-8 photoresist, i.e., no structure is formed during the mapping process.

First, a large area (100×100 μm^2) of the sample was scanned and many individual

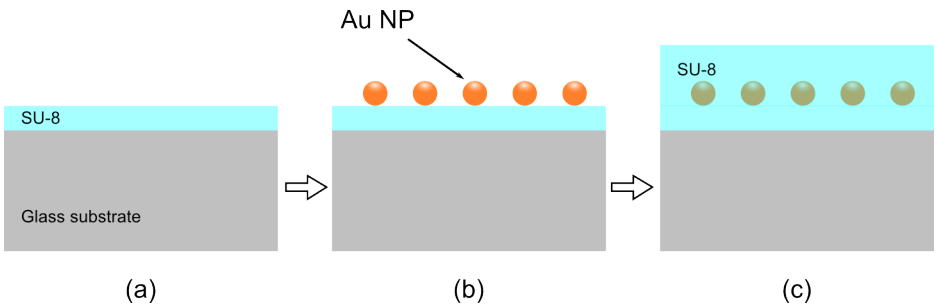

Figure 6.2: Sample preparation procedure for experiment of coupling a single plasmonic particle into a polymeric microsphere. (a) 500 nm thick film of SU-8 is spin-coated on a clean glass coverslip, (b) 50 nm diameter gold nanosphere particles is dropped on the top of the SU-8 film, followed by spreading at the spin speed of 1000rpm and 2000 rpm consecutively. (c) the last layer (on top) of SU-8 with thickness within $500 - 1000$ nm is deposited to cover the gold NP layer using the same technique.

Au NP were found. We then pointed out the position of each NP by scanning in a small area of 2×2 μm^2 around the NP, in (xy)–plane and in (xz)–plane, respectively, as shown in Fig. 6.3–(a). We achieved a axial resolution of 730 nm (Fig. 6.3–(b)), and a lateral resolution of about 243 nm (Fig. 6.3–(c)), which actually correspond to the diffraction limit of the used OL. The curve plotted in Fig. 6.3–(d) is an extract of data corresponding to the dot line passing by the center of the NP (Fig. 6.3–(c)), showing the fluorescence intensity as a function of position. The sharp peak reveals a precision $<$ 20nm for the position determination.

6.2.4 Embedding single NPs into PCs

Once the position of a single NP is determined, the fabrication of PC containing this NP will be realized. For the fabrication step, the excitation power was increased due to the ultra-low absorption of SU-8 photoresist at 532 nm excitation wavelength. In this experiment, we have chosen a power of 3.8 mW for all fabrications. A set of micropillars whose geometry is a hexagonal 2D PC was designed to fabricate so as the NP is located at the central pillar of the fabricated structure. Figure 6.4 shows a sketch of the fabrication process. In this process, the fabrication of each pillar was realized by scanning the focusing spot along the vertical direction (z-axis) and through the total SU-8 film thickness (total moving distance of 2 μm). We note that, we

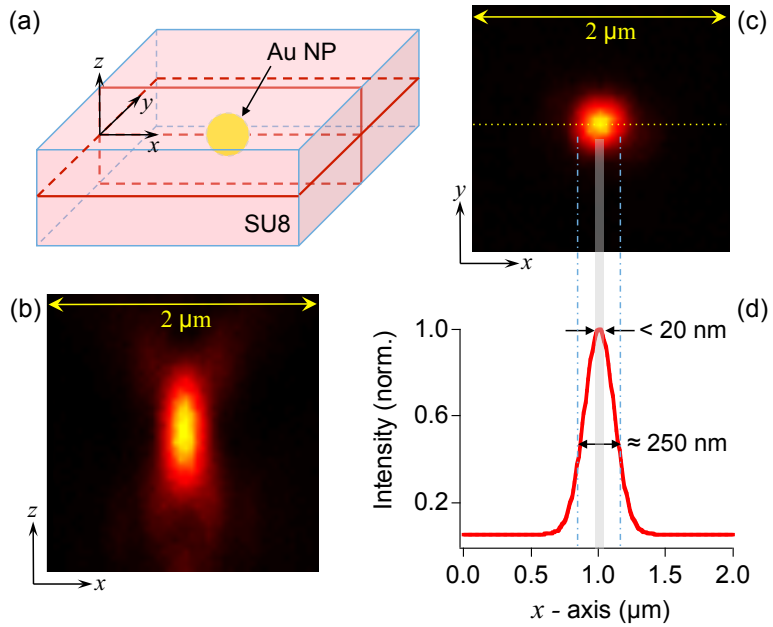

Figure 6.3: (a) Illustration of a sample area in which a gold NP is sandwiched in between SU-8 films. The fluorescence scanning is realized in the (xy)– and (xz)–planes, indicated by the red border rectangles. (b) and (c) Fluorescence images obtained by scanning along the (xz)– and (xy)–planes, respectively. (d) Extract of data corresponds to the dotted line shown in (c) showing the fluorescence intensity as a function of position of the NP and the precision of its position determination.

did not focus on investigating the effect of periodic microstructure, so the geometric parameters of the micropillars pattern were chosen so that the photonic bandgap (if any) of the micropillars hexagonal structure must stay far from the emission band of the Au NP embedded inside the structure. The micropillars pattern is only for easily identify such small structures under microscopies (optical, SEM), and is also to facilitate the identification of which pillar does contain the single Au NP among many else, which is for later presentation. After the exposure step, the sample was post-baked on a hot plate at 65° (3 mins) and 95° (5 mins) to finalize the cross-linking process, followed by the development step. The patterned sample was then put back on the PZT stage, at the same position of previous localizing step, for optical analysis and characterization. The morphology and surface topography of each structure was subsequently examined by optical microscope and scanning electron microscope.

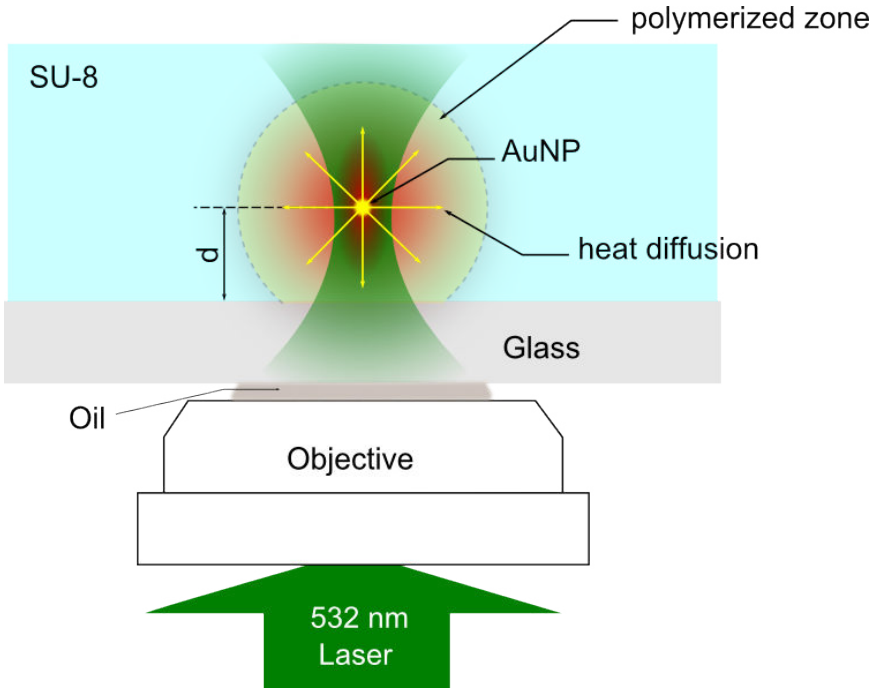

Figure 6.4: Sketch of exposure process and thermodynamic model used for explanation of thermal accumulation effect, which induce the polymerization within a spherical-shape volume.

6.2.5 Results

Figure 6.5–(a) shows a SEM image of a totally 11 structures on a glass substrate, each contains a single Au NP at its center. In this image, while all micropillar patterns have the same parameters (center-to-center distance of 1.50 μm; the diameter and the high of each pillars is about 0.32 μm and $\approx$ 1.00 μm, respectively), the microspheres at the center have different diameters varying from 0.76 to 1.40 μm. Figure 6.5–(b) shows a SEM micrograph of the structure outlined by red rectangular in Fig. 6.5–(a). The fabricated structure has a perfect spherical shape with the diameter of $D = 1.12$ μm.

The mechanism in which the spherical shape is formed is quite evident. It is explained by a thermodynamic modal (see Fig. 6.4), such that: during being continuously irradiated by focused laser beam, the Au NP within the laser spot absorbs strongly the green light resulting in strongly localized surface plasmon resonance (LSPR). The excitation energy decays mainly nonradiatively via electron-phonon collisions followed by phonon-phonon relaxation. As the result the particle is continuously

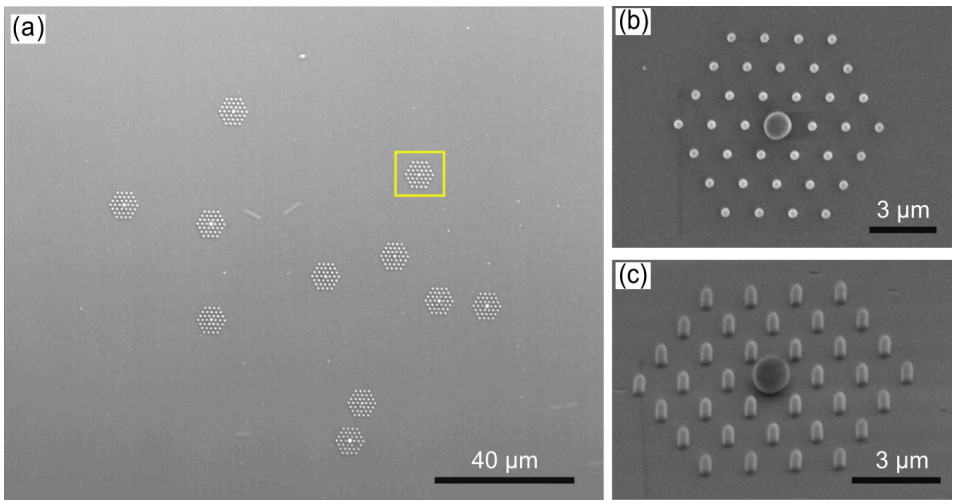

Figure 6.5: A series of structures are successfully fabricated by LOPA DLW technique. Structures containing a single gold NP appears to be spherical shape, which is always located at the center of the pattern.

heated and radially diffuse heat beyond the particle surface into the surrounding medium [116, 117]. Meanwhile, photoinitiators within focal spot absorb one-photon energies from the incident light to generate a certain number of strong acids (Lewis acid). The Au NP at that time plays a role as a "hot plate" which provides an amount of necessary heat for catalyzing the cross-linking reactions to take place. In turn, these reactions regenerate an adequate number of another acids. As long as the temperature is sufficiently high ($> 75°C$) at reaching these acids, the polymer chains is continuously formed [118]. As the result a spatially spherical volume which confines a high density of strong acid forms the spherical building block after development processes. The amount of heat generated by plasmonic NP can be controlled by the particle size, shape as well as the illumination strength, wavelength and irradiation duration. Hence interplay of Au NP with laser light allows spatial temporal heat management leading to controllable fabrication processes. With the given experimental setup, there are two ways preferable for handling the spherical size: either by intensity of the excitation light or by exposure time. It is worth to be borne in mind that the former could be out of control if the intensity is too high, temperature at focal volume if exceeding either the deformation point of Au NP (such as melting point, fragmentation threshold) or boiling point of the host SU-8 material. In such a case the convolution of the heat

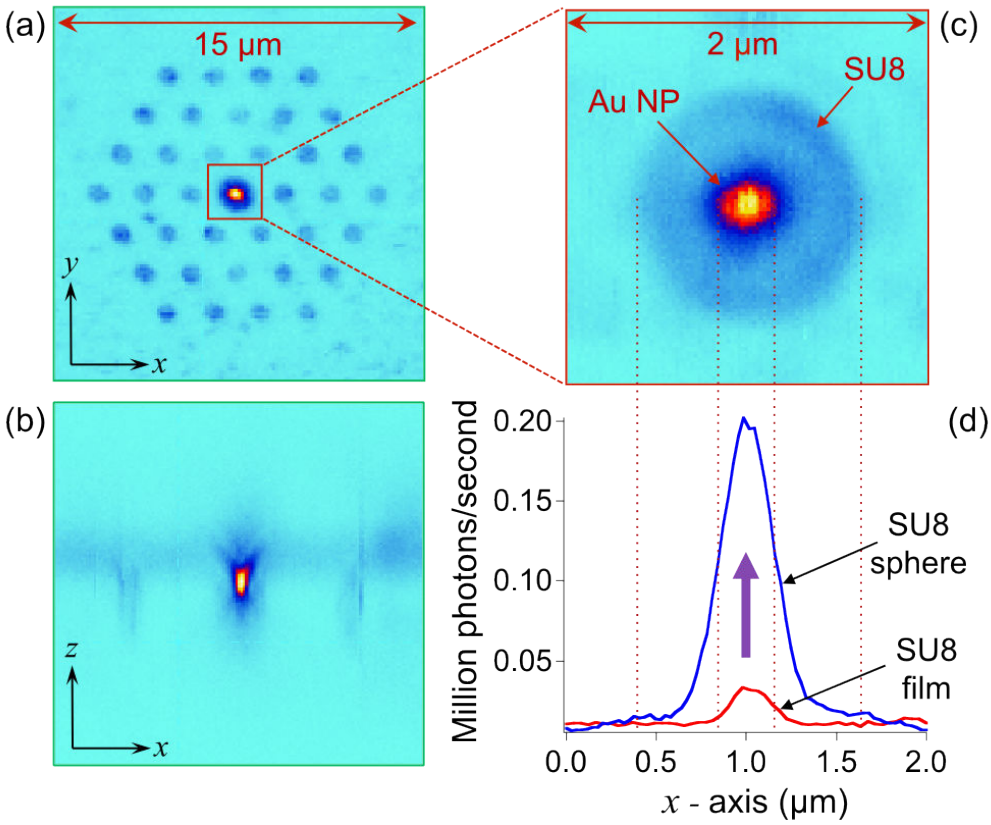

Figure 6.6: Fluorescence images of fabricated structures obtained in (a) (xy)– and (b) (xz)–planes. (c) Image of the microsphere containing a single Au NP. The single Au NP is locked at the center offers the very high intensity counts with respect to those of nearby SU-8 host medium surrounded by air. (d) Comparison of fluorescence signals in two cases, Au NP in microsphere (blue curve) and in unpatterned SU-8 photoresist film (red curve).

flux is unanticipated resulting in a micro-explosion or a laser-induced damage.

Figure 6.6 shows the fluorescence images in (a) (xy)– and (b) (xz)–planes of the fabricated structures, using the same excitation power as in the mapping step. It is obvious that the emission spot at the structure center is very bright comparing to the weak emission of the surrounding micropillars. Note that the SU-8 micropillars also fluorescence, but with very weak rate. Figure 6.6-(c) shows a zoomed fluorescence image of the structure containing single NP, which is located at the center (bright) and the shaded circle zone denote the weak fluorescence due to cured SU-8 photoresist. This strongly confirms the existence of a single Au NP inside the microsphere. Furthermore, by comparing the fluorescence signal obtained before fabrication (Au NP

embedded in uncured SU-8 films) and after fabrication (Au NP embedded in cured SU-8 microsphere), we found a strong enhancement. The red and blue curves in Fig 6.6-(d) represent the fluorescence intensity of the same Au NP, obtained before and after fabrication, respectively. In this case, we estimated a 6-fold enhancement in collected fluorescence rate. For all other structures, the enhancement factor varied in between 3.0-fold and 6.0-fold, due the difference of the microspheres sizes.

The origins of the fluorescence enhancement can be attributed to: i) geometric modification of the emitted light thanks to the microstructure and ii) the change of fluorescence emission rate when the surrounding medium of Au NP varies (SU-8 changes from unpolymerized to polymerized states). We expected that the first reason plays a dominant role, since the optical property of SU-8 does not change much in between two states. In order to understand the fluorescence enhancement in the case of NP/PS coupling, we performed a FDTD simulation using a commercial "Lumerical" software.

6.2.6 Numerical simulation

Simplifying our system with a view of optimizing the collection efficiency, we simply restrict ourself following considerations: 1) The gold NP is generalized as an emitter and being placed at the center of the microsphere. 2) uncured SU-8, cured SU-8 and glass are assumed to be all dielectric materials with refractive indices are 1.6, 1.58 and 1.51, respectively. 3) the amount of power radiated into the farfield is normalized with respect to the source power in a homogeneous medium. In addition, the oil and the glass coverslip have the same refractive index, this scheme does not take into account any refraction index mismatch so that we avoid of using the Fresnel correction when calculation the transmission in the farfield. In practice, an emitter is usually considered to be an electric dipole polarized either perpendicular or parallel to the glass-air interface. For many case of interest the dipole orientation is isotropic, by which we mean a dipole whose moment rotates and samples all directions in space in a time. This case may be described by a combination of vertical and horizontal emitters, weighted by a factor of 1/3 and 2/3 respectively.

We considered two particular configurations: a single Au NP embedded in SU-8

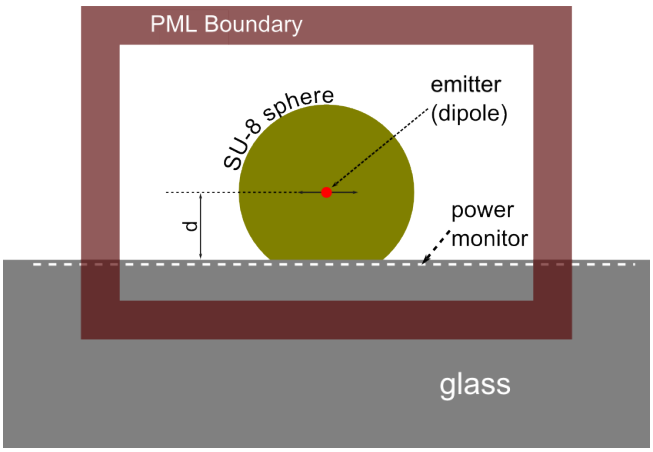

Figure 6.7: FDTD simulation setup for a single gold NP coupled into a polymeric microsphere: Perfect Matched Layers are used for simulation boundaries; SU-8 and glass media are supposed to be dielectric materials with refractive index of 1.58 and 1.51, respectively; 50 nm diameter spherical Au NP is assumed a horizontally polarized (parallel to the glass-photoresist interface). The power monitor placed underneath the interface is used to collect the emission power.

film ((***F***) configuration) and a single Au NP embedded in a SU-8 microsphere ((***S***) configuration). For both cases, we assumed that the oscillating dipole is located in SU-8 photoresist at $d = 500$ nm from the interface between SU-8 and glass substrate and the detector is located at the OL position (see Fig. 6.7). There are different important parameters representing optical properties of such NP/microsphere coupling system, but we focused only on the "extraction efficiency", which is defined as the ratio of the collected power to the total power radiated by the electric dipole. In order to evaluate how much the power of the source could be collected by a microscope objective we evaluate the power as the function of the acceptance angle θ. The acceptance angle is expressed as $\theta = \arcsin(\mathrm{NA/n})$, n is refractive index of oil, NA is the numerical aperture of the lens.

Figure 6.8–(a) shows the simulation result. It can be seen that, with the case of (***S***) configuration, almost 63% of the source power can be collected at the angle of $\theta \geqslant 59.81°$ or NA$\geqslant$1.3 microscope objective. Meanwhile, with the case of (***P***) configuration, the maximum power collected is as high as 23% by using the same aperture lens. Hence, an extraction efficiency enhancement of 2.75-fold is evident.

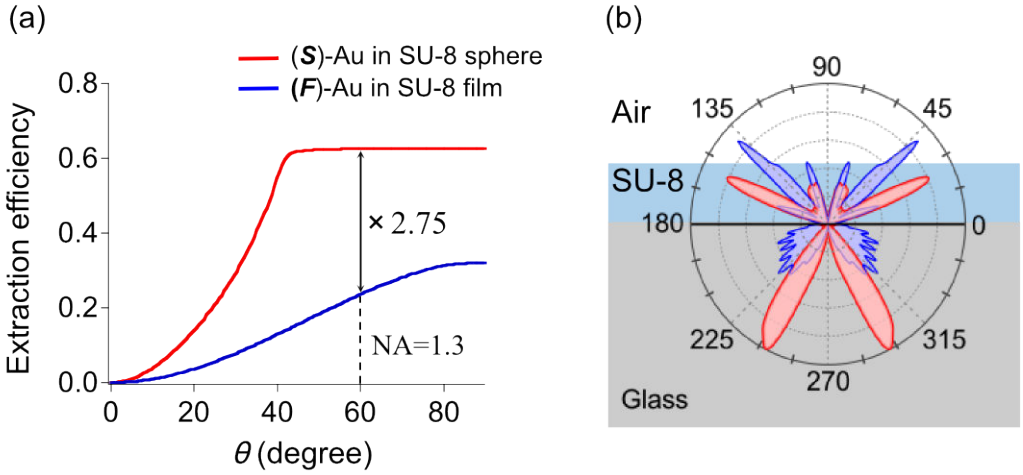

Figure 6.8: Calculation of fluorescence extraction efficiency in two situations: a single Au NP in a photoresist microsphere (red curves) and a single Au NP in unpatterned SU-8 photoresist film (blue curves). Simulations are based on FDTD method, with (see Fig. 6.7): $d = 503$ nm, $r = 553$ nm, emitted wavelength $\lambda = 650$ nm. We also assumed that a single NP corresponds to an absorption/emission dipole oriented parallel to the air/glass interface. (a) Extraction efficiency versus half–angle θ. (b) Polar diagrams of normalized electric field intensity in (xz)–plane shows the spatial distribution of the emitted light (radiation pattern).

6.3 Discussions, conclusions and prospects

To explain this simulation result, we note that for small particles behaving like dipoles close to a dielectric interface, the radiated power is principally emitted towards the denser medium at the critical angle [119]. Because SU-8 film possesses a high refractive index with respect to that of glass substrate, the emission from the Au NP suffered a total internal reflection (TIR), so that all the emitted light at angles larger than the critical angle are completely reflected. In contrast, in case of Au NP embedded in SU-8 microsphere, the Au NP is bounded by a small SU-8 volume, surrounding by air, resulting in a low effective refractive index, as compared to that of glass substrate. Therefore there is no limitation caused by TIR effect and the radiated light is transmitted into glass substrate and is mostly collected by the objective. This is confirmed by the radiation pattern, i.e. the electric field intensity distribution in (xz)–plane, shown in Fig. 6.8–(b). A single dipole, oriented parallelly to the dielectric interface, emits light mainly in the direction close to the critical angle, represented

by two lobes. We can see that in the case of ($\boldsymbol{S}$) configuration (red), a significant portion of emitted light is located in the vicinity of $\theta_c = \arcsin(1/n_{glass}) = 41.2°$, which belongs to the solid cone of the microscope objective, and can be detected. Whereas the radiation pattern of ($\boldsymbol{F}$) configuration oriented at larger angle and the radiation intensity is approximately three times weaker, leading to a loss of photons because they are out of the solid cone of the microscope objective.

Certainly, we can not directly compare the experimental result with the numerical simulation result because of our oversimplification in treating the 50 nm gold nanopartricle as an oscillating electric dipole. Although such modeling allows us verify the emission pattern, it does not valid to evaluate the total enhancement in collection efficiency. Such an oversimplification of the system does not take into account many aspects of the Au NP interacting with light. In such a case, when irradiation to the CW laser beam for along time the Au NP could be reshaped or suffered a fragmentation, a Au nanocluster can not be resolved by optical microscope could give rise strongly photoluminescence enhancement [120, 121]. In contrast to the ($\boldsymbol{F}$) configuration, in ($\boldsymbol{S}$), the changes in the local refractive index associated with increasing rapidly temperature in the infinite volume also be a origin of the red–shift in plasmon resonance band as well as the angular distribution pattern [122], giving rise the lager amount of emitted photon could pass in to the detection window (> 580 nm), enhancing the photon collected efficiency. So, a complete model and full mathematical calculation for the case is needed, open up for the future investigation.

In conclusion, we have demonstrated a simple and low-cost technique to precisely reposition and embed a single nano-emitter, a single plasmonic Au NP used in this chapter was an demonstrative example, into a photonic microstructure. The coupled NP/photonic microstructure was realized by a confocal system working in very low linear absorption regime, and with a double-step technique: ultra-low excitation power for determination of nano-emitter position, and low excitation power for fabrication of desired microstructures. The coupling of single nano-emitter into PC allowed a great enhancement of extraction efficiency of, as compared to the case without coupling. This LOPA-based direct laser writing with a double-step technique is very simple but powerful comparing with other complicated and expensive techniques that we have mentioned before. It is also very promising to embed other non-fluorescent nano-object

into PC, such as diamond NP containing a single emitter, into desired polymer-based PCs, thus allowing the manipulation of the single photon emission.

Conclusion and outlook

We have introduced a new technique, which bases on an already-well-known mechanism, namely one-photon absorption direct laser writing (DLW) for fabrication of low-cost, high-quality 3D PCs. We demonstrated the new technique through both theory and experiment on the ultra-low absorption regime (LOPA) of photosensitive material. We pointed out that DLW based on LOPA microscopy enables 3D fabrication in any kind of photoresist material with flexible defect engineering.

The course of the thesis is described as follows:

To obtain deeper insight in the physics of optical lithography based on optical microscope, we performed an investigation on the structure of electromagnetic wave focusing and propagating in an absorbing medium. We developed our model by extending the theory of focused electromagnetic wave in homogeneous, transparent, single medium, which was firstly accomplished by Debye and Wolf. The development of the theory was made by using the same approach proposed by Torök and the theory of the electromagnetic wave propagating in an absorbing medium. Thanks to this theory we obtained a rigorous solution of Maxwell' equation for our DLW technique.

Basing on the developed formulation we proceeded numerical calculations for most important parameters in DLW, which are the structure of diffraction pattern, the intensity distribution of the focal region, the maxima intensity at the focus, the lateral and the axial size of the focusing spot, *etc.* In most cases, the calculations are made for different focus depth and different NAs of the used objective lens. The important results obtained from this theory can be divided into two general cases.

The first case deals with mismatched refractive index (MRI). In this case, the spherical aberration plays a predominant role in the attenuation of intensity at the focus. Indeed, the intensity at the focus varies linearly and nonlinearly as a function of

both NA and focus depth. On going from the interface towards the absorbing material, maxima intensity decreases and the energy distribution becomes less concentrated. The trend of attenuation depends on the absorption strength of material. For a given focus depth and given absorption strength, the nonlinearity behavior makes the intensity at the focus difficult to be dictated. Sometimes, a high NA gives less intensity at the focus then the low one. These results well agreed with those obtained by Torök and co-workers for lossless case. However, the absorption effect always performs its duty, that, the intensity at the focus decreases as a function of the focus depth in parallel with the attenuation due to MRI. The stronger absorption is, the smaller the intensity at the focus is, no matter how the aberration be. The second case, the case of refractive index accordance. The behavior of the intensity at the focus become linear. This means the intensity at the focus varies linearly as the function of the focus depth and NA. It is evident that, a higher NA give higher intensity, it is even true for every focus depth as well as the absorption strength. In the case of very weak absorption (as the case we investigated for SU-8 and a green laser) the convolution of the intensity at the focus is almost the same to that of without absorption case. The light travels in the absorbing medium freely as if it does in a transparent medium. Light intensity at the focus is very high, about seven order of magnitude compared to that at the entrance pupil of the objective lens.

The low absorption, strong focusing and the MRI-free become three crucial key points in experiments with DLW. The OPA polymerization mechanism in the case of ultra-low absorption is similar to TPA one: the polymerization reactions take place significantly only at the focus, then decrease quickly from very high to almost ten millions time weaker at distance of about 2 μm from the focus origin. We applied LOPA microscopy for a regular DLW for fabrication of 2D and 3D PCs. A series of 2D CPCs and 3D PCs that we have shown strongly confirm the capability of LOPA for 3D submicrometer fabrication. Furthermore, we also have demonstrated that our technique can apply not only for fabrication of defect-free submicometer structures but also for freely design a defect within the body of fabricated PCs. Indeed, in our experiment, a “L”-shape waveguide is successfully engineered on the top and at the bottom facet of a 3D fcc spiral structure. In addition, we also demonstrate LOPA DLW through the fabrication of arbitrary volumetric 3D photonic structure,

the "LPQM" letter structure is an example. From the experiment results in fabrication of 2D and 3D PCs (2D micropillars-based CPC, woodpile, chiral twisted, spiral, defect engineering and arbitrary volumetric structure) we have validated the correctness of LOPA idea and demonstrate its flexibility for fabrication of any kind of photonic structure at wavelength scale.

However, LOPA has a native drawback, that is common feature in any linear system, that is dose accumulation effect. We were aware that this kind of effect can not be eliminated but can be improved. Experimentally and theoretically we demonstrated that the deformed structure due to linear absorption can be minimized by applying our compensation technique. The idea is that, we attentively compensate an amount of dosage by increasing the exposure dose at the thinner part and reducing the dose at the thicker part of the fabricated structure. Of course, the compensation is on-fabrication process, which means that we predict the degree of distortion (even the shrinkage effect is also counted in) based on both experiments and theoretical calculation to calculate an amount of dose which must be compensated, different dose for different parts. By applying this technique, we have obtained better quality of the fabricated structures.

On the way of demonstration of the LOPA DLW technique, we have demonstrated the capability to coupling a single nano-emitter to the photonic structure. In this demonstration we chose to work with a gold nanoparticle as an active material and a 2D hexagonal micropillars PC structure as a host medium. We have shown that by applying the double-step fabrication technique we can precisely couple a single Au NP into a spherical-shape microstructure. Our measurements have shown an accuracy of about 20 nm for addressing a single Au NP on the unpatterned material and embedding into the microstructure. An application of a single plasmonic-photonic device system is to investigate the coupling of plasmon resonance field to the photonic mode of the photonic device. The investigation of this application beyonds the frame of the thesis. Here we focused only on the enhancement of collection efficiency of spontaneous emission. This is very important aspect in quantum information processing application. In our experiment, the embedded single Au NP in a microsphere structure gives an enhancement up to 6-fold of photon collection efficiency if the detector is placed at appropriate position in comparison with the case in which a single Au NP is embedded

in an unpatterned host material. Our theory and experiment have shown that the enhancement is due to the different refractive index between SU-8 and air, in addition with the modification of the geometry of the microsphere structure.

For conclusion, we have theoretically and experimentally investigated the LOPA microscopy applying to DLW for successful fabrication of 2D and 3D PCs with or without defects. We investigated the theory of compensation technique to improve quality of the structures fabricated by LOPA DLW. We demonstrated the capability of LOPA microscopy for precisely coupling a single fluorescent emitter to the polymeric microstructure. The investigation will pave a way for facilitating, simplifying and reducing the cost of submicrometer 3D fabrication.

For outlook, we emphasize some remarkable applications of LOPA microscopy as follows.

- Fabrication of 3D Micro-resonators (MRs): In MRs, the coupling light into resonant mode of the photonic structure requires a small gap between resonator and excitation devices, such as integrated waveguides, tapered fiber optics or prisms [123–125]. In polymer 2D microring resonators or 3D microresonator, the gap, which support the best coupling between devices requires well controlling gap size and the surface roughness must be as smooth as possible. Enter into among many current lithography techniques, which are associated to polymers materials, LOPA DLW can be a simple and low-cost technique for fabrication of such polymer-based 3D microresonator because of capability in well control size gap as well as reducing the roughness using the compensation technique. So far, the smallest gap can reach by LOPA is as narrow as hundred nanometers.

- Coupling an arbitrary single nano-emitter to the photonic device: Three kinds of wide-used emitters in literature for coupling problem are QDs, N-V centers and plasmonic NPs. All of them can be the targets on LOPA fabrication technique. Indeed, since the technique is the polymer-based, and LOPA uses just a single wavelength for both mapping and fabrication, a single fluorecent nano-emitter embedded in polymer can be imaging then precisely addressing. The subsequent fabrication step can be done easily to confine the emitter on/in polymeric photonic device.

Appendices

Appendix A

Inhomogeneous waves at the interface of lossy isotropic media

Consider a plane monochromatic wave propagating in a lossy isotropic medium characterized by complex permittivity $\epsilon = \epsilon' - i\epsilon''$ and permeability $\mu = \mu' - i\mu''$. The electric, $\mathbf{E}$, and magnetic, $\mathbf{H}$, field vectors of such a wave are given by

$$\mathbf{E} = \mathbf{e}e^{i(\omega t - \mathbf{k}\cdot\mathbf{r})}, \quad \mathbf{H} = \mathbf{h}e^{i(\omega t - \mathbf{k}\cdot\mathbf{r})}, \tag{A.1}$$

where $\mathbf{e}$ and $\mathbf{h}$ are complex amplitude vectors, $\mathbf{k}$ and $\mathbf{r}$ are the wavevector and a position vector, respectively, with ω and t being the frequency and time. In a lossy medium the wavevector $\mathbf{k}$ is complex, that is, $\mathbf{k} = \mathbf{k}' - i\mathbf{k}''$, where $\mathbf{k}'$ and $\mathbf{k}''$ are real phase and attenuation vectors, respectively. If the vectors $\mathbf{k}'$ and $\mathbf{k}''$ are not parallel, the planes of constant phase and constant amplitude (defined as $\mathbf{k}' \cdot \mathbf{r}$ =const and $\mathbf{k}'' \cdot \mathbf{r}$ =const, respectively) are not parallel either, and the corresponding wave is inhomogeneous.

Now we define the refractive index m' and attenuation coefficient m'' of an inhomogeneous wave. In Fig. A.1 we depict the orientation of the phase and attenuation vectors at the interface (white plane) of two lossy isotropic media- the blue and red planes are the incidence planes for the phase and attenuation vectors, respectively. The lengths of $\mathbf{k}'$ and $\mathbf{k}''$ as $|\mathbf{k}'| = \frac{\omega}{c_0}m'$ and $|\mathbf{k}''| = \frac{\omega}{c_0}m''$, where c_0 is the speed of light in vacuum. Such a definition retains the physical meaning of the refractive index and attenuation coefficient; namely, m' equals the ratio of c_0 to the phase velocity and m''

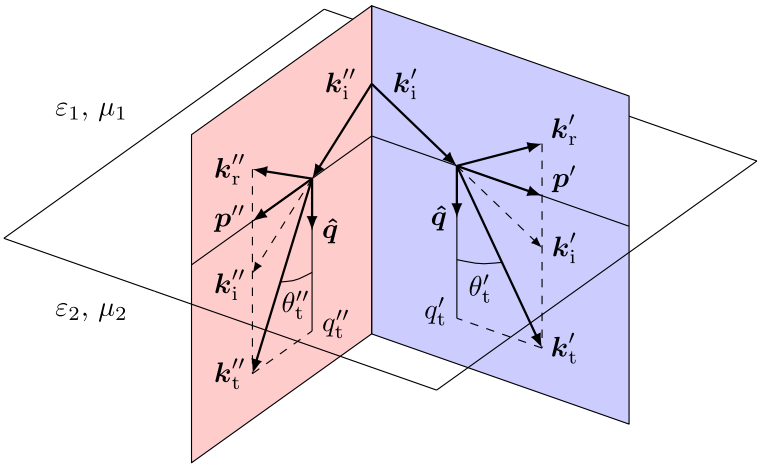

Figure A.1: Orientation of the phase and attenuation vectors at the interface (white plane) of two lossy isotropic media. The blue and red planes are the incidence planes for the phase and attenuation vectors, respectively.

determines the distance at which the amplitude is reduced to $1/e$ times. Note that both m' and m'' are real and positive by definition, since we determine them through the length of a real vector.

By separately equating the real and imaginary parts in the dispersion equation $\mathbf{k}^2 = \epsilon\mu\omega^2/c_0^2 = n^2\omega^2/c_0^2$, where the complex value $n = n' - in''$ is defined as $n^2 = \epsilon\mu$, we find

$$m'^2 - m''^2 = \epsilon'\mu' - \epsilon''\mu'' = n'^2 - n''^2, \tag{A.2a}$$

$$m'm''\cos\vartheta = \frac{1}{2}(\epsilon'\mu' + \epsilon''\mu'') = n'n'', \tag{A.2b}$$

in which ϑ is the angle between $\mathbf{k}'$ and $\mathbf{k}''$. Note that inhomogeneous waves with $m'' \neq 0$ can exist in lossless media($\epsilon'' = \mu'' = 0$) if $\vartheta = 90°$ in Eq. (A.2b); that is, if $\mathbf{k}' \perp \mathbf{k}''$. For example, such a kind of inhomogeneous wave describes total internal reflection, where a wave at the boundary of two lossless media propagates along the boundary and attenuates in the direction perpendicular to the interface. Additionally, Eqs. (A.2a) and (A.2b) indicate that $n' = m'$ and $n'' = m''$ only if $\vartheta = 0$; that is, if $\mathbf{k}' \parallel \mathbf{k}''$ (homogeneous damped waves). Thus the complex quantity n loses its traditional meaning of refractive index for inhomogeneous waves ($\vartheta \neq 0$).

A.1 General law of reflection and refraction

We examine the formation of inhomogeneous waves at the interface of two lossy isotropic media: the first medium is characterized by a complex permittivity $\epsilon_1 = \epsilon_1' - i\epsilon_1''$ and permeability $\mu_1 = \mu_1' - i\mu_1''$, and the second medium by $\epsilon_2 = \epsilon_2' - i\epsilon_2''$ and permeability $\mu_2 = \mu_2' - i\mu_2''$. The incident wave comes from the first medium, and a unit interface normal $\hat{\mathbf{q}}$ points to the second medium (see Fig. A.2). The wavevectors $\mathbf{k_i}$, $\mathbf{k_r}$ and

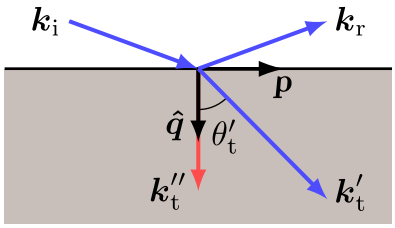

Figure A.2: Orientations of the phase and attenuation vectors at the interface between a lossless dielectric and a lossy isotropic medium.

$\mathbf{k_t}$ of the incident, reflected and transmitted waves can be written as the sum of two vectors that are parallel and perpendicular to the interface

$$\mathbf{k_i} = \mathbf{p} + q_i\hat{\mathbf{q}}, \quad \mathbf{k_r} = \mathbf{p} + q_r\hat{\mathbf{q}}, \quad \mathbf{k_t} = \mathbf{p} + q_t\hat{\mathbf{q}}, \tag{A.3}$$

The parallel components $\mathbf{p}$ are continuous across the interface:

$$\mathbf{p} = [\hat{\mathbf{q}} \times [\mathbf{k_i} \times \hat{\mathbf{q}}]] = [\hat{\mathbf{q}} \times [\mathbf{k_r} \times \hat{\mathbf{q}}]] = [\hat{\mathbf{q}} \times [\mathbf{k_t} \times \hat{\mathbf{q}}]], \tag{A.4}$$

The normal components have magnitudes $q_i = (\mathbf{k_i} \cdot \hat{\mathbf{q}})$, $q_r = (\mathbf{k_r} \cdot \hat{\mathbf{q}})$ and $q_t = (\mathbf{k_t} \cdot \hat{\mathbf{q}})$, where

$$q_r = q_i, \quad q_t^2 = \epsilon_2\mu_2\omega^2/c_0^2, \tag{A.5}$$

For the most general case, all three wavevectors $\mathbf{k}_\alpha$ (with $\alpha \equiv i, r$, and t) are complex, that is, $\mathbf{k}_\alpha = \mathbf{k}_\alpha' - i\mathbf{k}_\alpha''$. Therefore, $\mathbf{p} = \mathbf{p}' - i\mathbf{p}''$ and $q_\alpha = q_\alpha' - iq_\alpha''$, where

$$\mathbf{p}' = [\hat{\mathbf{q}} \times [\mathbf{k}_i' \times \hat{\mathbf{q}}]], \quad \mathbf{p}'' = [\hat{\mathbf{q}} \times [\mathbf{k_i}'' \times \hat{\mathbf{q}}]], \tag{A.6a}$$

$$q_\alpha' = (\mathbf{k}_\alpha' \cdot \hat{\mathbf{q}}), \quad q_\alpha'' = (\mathbf{k}_\alpha'' \cdot \hat{\mathbf{q}}), \tag{A.6b}$$

By separately equating the real and imaginary parts in Eq. (A.3), we obtain two sets of equations for the phase vectors $\mathbf{k}'_\alpha$ and attenuation vectors $\mathbf{k}''_\alpha$:

$$\mathbf{k}'_\mathbf{i} = \mathbf{p}' + iq'_i\hat{\mathbf{q}}, \qquad \mathbf{k}''_\mathbf{i} = \mathbf{p}'' + iq''_i\hat{\mathbf{q}}, \tag{A.7a}$$

$$\mathbf{k}'_\mathbf{r} = \mathbf{p}' + iq'_r\hat{\mathbf{q}}, \qquad \mathbf{k}''_\mathbf{r} = \mathbf{p}'' + iq''_r\hat{\mathbf{q}}, \tag{A.7b}$$

$$\mathbf{k}'_\mathbf{t} = \mathbf{p}' + iq'_t\hat{\mathbf{q}}, \qquad \mathbf{k}''_\mathbf{t} = \mathbf{p}'' + iq''_t\hat{\mathbf{q}}. \tag{A.7c}$$

According to Eqs. (A.7a)-(A.7c) the phase vectors $\mathbf{k}'_\alpha$ and attenuation vectors $\mathbf{k}''_\alpha$, in general, lie in two different planes (see Fig. A.2). In other words, at the plane interface of two lossy isotropic media, there are, in general, two incidence planes: the incidence plane for the phase vectors (spanned by $\mathbf{k}'_i$ and $\hat{\mathbf{q}}$ with the normal $\mathbf{s}' = [\mathbf{k}'_i \times \hat{\mathbf{q}}]$) and the incidence plane for the attenuation vectors (spanned by $\mathbf{k}''_i$ and $\hat{\mathbf{q}}$ with the normal $\mathbf{s}'' = [\mathbf{k}''_i \times \hat{\mathbf{q}}]$).

Two incidence planes result in two sets of equalities for Snell's law, for the phase and attenuation vectors, respectively. We find them by equating the magnitudes of the real and imaginary parts in Eq. (A.4) and using the definitions of m' and m'':

$$m'_i \sin\theta'_i = m'_r \sin\theta'_r = m'_t \sin\theta'_t \tag{A.8a}$$

$$m''_i \sin\theta''_i = m''_r \sin\theta''_r = m''_t \sin\theta''_t. \tag{A.8b}$$

where θ'_α and θ'_α are the angles between the unit normal $\hat{\mathbf{q}}$ and the associated phase vectors $\mathbf{k}'_\alpha$ and attenuation vectors $\mathbf{k}''_\alpha$, respectively.

Before we focus on the transmitted wave, we make a simple remark on the reflected wave. The reflected wave has the same inhomogeneity as that of the incident wave, so that $m'_r = m'_i$ and $m''_r = m''_i$ (the reflection angles are $\theta'_r = \pi - \theta'_i$ and $\theta''_r = \pi - \theta''_i$). This implies that if the first medium is lossless and the incident wave is homogeneous, then the reflectedwave is also homogeneous, even if the second medium is lossy [126–128].

Now we examine the transmitted wave whose phase and attenuation vectors are given by Eq. (A.7c). In Eq. (A.7c) we need to determine the projections q'_t and q''_t , which are the real and imaginary parts of the complex projection $q_t = q'_t - iq''_t$. Note that we cannot uniquely determine q_t using Eq. (A.5), since q_t is in the quadratic form. Many textbooks choose a positive sign for q_t, or equivalently $q'_t = (\mathbf{k}'_\mathbf{t} \cdot \hat{\mathbf{q}}) > 0$

and $q_t'' = (\mathbf{k_t''} \cdot \hat{\mathbf{q}}) > 0$, because the phase vector, and consequently the phase velocity, are outgoing from the interface only for this choice of sign. We now know, however, that the phase velocity can be incoming towards the interface if negative refraction takes place. Thus a careful study is necessary to unambiguously determine the sign of q_t. For this purpose we introduce a complex dimensionless parameter $\xi = \xi' - i\xi''$, defined as

$$\xi = q_t^2 \frac{c_0^2}{\omega^2}. \tag{A.9}$$

For its real and imaginary parts, we find $\xi' = (q_t'^2 - q_t''^2)c_0^2/\omega^2$ and $\xi'' = 2q_t'q_t''c_0^2/\omega^2$. Therefore, taking into account that q_t' and q_t'' are real by definition, we obtain $q_t'^2 = (|\xi|^2 + \xi')\omega^2/c_0^2$, and $q_t''^2 = (|\xi|^2 - \xi')\omega^2/c_0^2$, where $|\xi| = \sqrt{\xi'^2 + \xi''^2}$. To find the signs of q_t' and q_t'' we express them as

$$q_t' = s' \frac{\omega}{c_0}\sqrt{\frac{(|\xi| + \xi')}{2}}, \quad , \quad q_t'' = s'' \frac{\omega}{c_0}\sqrt{\frac{(|\xi| - \xi')}{2}}, \tag{A.10}$$

where $s' = \pm 1$ and $s'' = \pm 1$ are their signs. Then, since $\xi'' = 2q_t'q_t''c_0^2/\omega^2 = s's''[(|\xi| + \xi')(|\xi| - \xi')]^{1/2}$, we find that

$$s's'' = sgn\{\xi''\}. \tag{A.11}$$

Thus the signs s' and s'' are the same if $\xi'' > 0$, and opposite if $\xi'' < 0$. Specific values of s' and s'' can be selected only by applying an additional constraint: that the energy flux in the second medium must be directed away from the interface. Mathematically we write this constraint as $\mathbf{P}_t \cdot \hat{\mathbf{q}} \geq 0$, meaning that the projection of the time-averaged Poynting vector $\mathbf{P}_t$ of the transmitted wave on the interface normal must be nonnegative.

To calculate q_t' and q_t'' by Eq. (A.10), we need to express ξ' and ξ'' through some known values such as permittivities, permeabilities, incidence angles, *etc.* To do so we substitute Eq. (A.5) into Eq. (A.9) and then separate the real and imaginary parts. As a result we obtain

$$\xi' = (\epsilon_2'\mu_2' - \epsilon_2''\mu_2'') - (\mathbf{p}'^2 - \mathbf{p}''^2)\frac{c_0^2}{\omega^2}, \tag{A.12a}$$

$$\xi'' = (\epsilon_2'\mu_2'' + \epsilon_2''\mu_2'') - 2(\mathbf{p}'\mathbf{p}'')\frac{c_0^2}{\omega^2}. \tag{A.12b}$$

Using Eq. (A.6a), we express the terms with $\mathbf{p}'$ and $\mathbf{p}''$ in Eq. (A.12a) and Eq. (A.12b) through the parameters of the incident wave:

$$\mathbf{p}'^2 = m_i'^2 \frac{\omega^2}{c_0^2} \sin\theta_i'^2, \qquad \mathbf{p}''^2 = m_i''^2 \frac{\omega^2}{c_0^2} \sin\theta_i''^2, \tag{A.13a}$$

$$\mathbf{p}' \cdot \mathbf{p}'' = m_i' m_i'' (\cos\vartheta - \cos\theta_i' \cos\theta_i''). \tag{A.13b}$$

where the angle ϑ between $\mathbf{k}'$ and $\mathbf{k}$" can be found from (A.2b) for the incident wave. Then we obtain

$$\xi' = (\epsilon_2' \mu_2' - \epsilon_2'' \mu_2'') - (m_i'^2 \sin\theta_i'^2 - m_i''^2 \sin\theta_i''^2), \tag{A.14a}$$

$$\xi'' = (\epsilon_2' \mu_2'' + \epsilon_2'' \mu_2'') - 2m' m'' (\cos\vartheta - \cos\theta' \cos\theta''). \tag{A.14b}$$

Having clarified the sign issue of the complex projection q_t, we now turn to the refractive index m_t' and attenuation coefficient m_t'' . From Eq. (A.7c) and Eq. (A.10) we have $k_t'^2 = p'^2 + q_t'^2 = \frac{1}{2}(|\xi| + \xi' + 2\mathbf{p}'^2 c_0^2/\omega^2)\omega^2/c_0^2$, which is equal to $k_t'^2 = m_t'^2 \omega^2/c_0^2$. Therefore, we obtain $m_t' = [(|\xi| + \xi' + 2\mathbf{p}'^2 c_0^2/\omega^2)/2]^{1/2}$, where we have chosen the " + " sign since m_t' is positive by definition. Similarly, we obtain $m_t'' = [(|\xi| - \xi' + 2\mathbf{p}''^2 c_0^2/\omega^2)/2]^{1/2}$. With the help of Eq. (A.13a), we find that m_t' and m_t'' can be written as

$$m_t' = \sqrt{(|\xi| + \xi' + 2m_i'^2 \sin\theta_i^2)/2}, \tag{A.15a}$$

$$m_t'' = \sqrt{(|\xi| - \xi' + 2m_i''^2 \sin\theta_i^2)/2}. \tag{A.15b}$$

Equations Eq. (A.15a) and Eq. (A.15b) clearly show that the refractive index m_t' and attenuation coefficient m_t'' depend not only on the material properties of the second medium, but also on the incidence angles θ_i' and θ_i'' .

To summarize the results of this section, we describe how one can find the parameters of the transmitted wave if the corresponding parameters of the incident wave are known: (*i*) calculate ξ' and ξ'' from (A.14a) and (A.14b) (ϑ can be found from (2b)); (*ii*) find the refractive index m_t' and attenuation coefficient m_t'' from Eq. (A.15a) and Eq. (A.15b); (*iii*) with the obtained m_t' and m_t'' calculate the transmission angles θ_t' and θ_t'' using Eq. (A.8a) and Eq. (A.8b); (*iv*) find the signs of q_t' and q_t'' in Eq. (A.10), utilizing Eq. (A.11) with the additional constraint $\mathbf{P}_t \cdot \hat{\mathbf{q}} \geq 0$, where the time-averaged Poynting vector of the transmitted wave, $\mathbf{P}_t$, should be calculated separately.

A.2 Particular cases

As a particular example, we consider a single interface where the first medium is a lossless dielectric ($\epsilon'' = \mu'' = 0$) and the second medium is lossy and isotropic (see figure A.2). We further assume that the incident wave is a homogeneous plane wave, which is characterized by the real wavevector $k_i = k_i'$ ($k_i'' = 0$ and $\mu_i'' = 0$), refractive index $m_i' = \sqrt{\epsilon_1 \mu_1} = n_1$, and incidence angle $\theta_i' = \theta_i$. According to Eq. (A.6a) and Eq. (A.7c), the condition $\mathbf{k_i''} = 0$ means that $\mathbf{p}'' = 0$ and $\mathbf{k_t''} = \mathbf{q_t''}\hat{\mathbf{q}}$. As a consequence the transmission angle $\theta_t'' = 0$. Thus the attenuation vector $\mathbf{k_t''}$ of the transmitted wave is normal to the interface for any incidence angle. In other words, equiamplitude planes of the transmitted wave are always parallel to the interface[126, 127].

For the case of a single interface Eq. (A.14a) and Eq. (A.14b) can be simplified as

$$\xi' = (\epsilon_2' \mu_2' - \epsilon_2'' \mu_2'') - ({n_1}^2 \sin\theta_i'), \qquad \xi'' = (\epsilon_2' \mu_2'' + \epsilon_2'' \mu_2'').$$

With these ξ' and ξ'' we can calculate the refractive index m_t' and attenuation coefficient m_t'' of the transmitted wave using (A.15a) and (A.15b), and then the transmission angle $\theta - t$ using (A.8a).

To find the orientation of $\mathbf{k'}_t$ and $\mathbf{k''}_t$, we need to determine the signs of their projections q_t' and q_t'' in (A.7c). In any lossy medium, the projection of an attenuation vector onto a time-averaged Poynting vector is always positive, so that $\mathbf{k_t''} \cdot \mathbf{P_t} > 0$, where $\mathbf{P}_t$ is the time-averaged Poynting vector of the transmitted wave. By substituting $\mathbf{k_t''}$ from (A.7c) into (A.4) and taking into account that $\mathbf{p}'' = 0$, we find $q_t''(\mathbf{P}_t \cdot \hat{\mathbf{q}}) > 0$. Since the condition for the energy flux to be directed away from the interface is $\mathbf{P}_t \cdot \hat{\mathbf{q}} \geq 0$, we eventually find that q_t'' must be positive. That is, the attenuation vector $\mathbf{k_t''}$ of the transmitted wave is outgoing from the interface.

For conclusion of this section, we have derived a general law for inhomogeneous wave at the interface of lossy isotropic media. We obtained explicit expressions for the parameters of a wave transmitted through the interface between two lossy media which are characterized by complex permittivity and permeability. We shown that, in any lossy medium, the projection of an attenuation vector onto a time-averaged Poynting vector is always positive and most important result which is being applied in the next section is that, in particular case, where the first medium is a lossless

dielectric (such as a glass or oil medium) and the second medium is lossy and isotropic (such as a photoresist) the attenuation vector $\mathbf{k}_\mathbf{t}''$ of the transmitted wave is always normal to the interface for any incidence angle from the first medium. The result of this section also can be extended for further investigations in negative refraction of a inhomogeneous waves at the interface.

Appendix B

Matlab codes for simulations

Matlab codes for calculation of maxima intensity at the focusing spot.

```
% Calculation of time-averaged electric field at near focal plane
global n1 n2 e21prime e22prime

NA=1.3;
n1=1.58;
n2=1.58; k2=0.0000306;
wl=532*1e-9;
fo=1e-3; % laser power
lo=0.32*1e-3;
theta=0;
%%%%
e0=8.854187821e-12;
c=3.0e+8
scale=0.5*n2*c*e0;
%%%%%%%%
e21prime=n2^2-k2^2;
e22prime=2*n2*k2;
a=asin(NA/n1);
k0=2*pi/wl;
k1=k0*n1;
%%%%%%%
K=fo*lo/2*k1;
```

```
%%%%%%%
numpoints=150;
d=25e-6;
% coordinate preparation
    grid=zeros(numpoints,numpoints,8);
    x=1.0e-6*linspace(-1.2,1.2,numpoints);
    y=1.0e-6*linspace(-1.2,1.2,numpoints);
    [X,Y]=meshgrid(x,y);
% z-position at maximum
    z=zatmax(NA,k2,d,wl,numpoints);
for m=1:numpoints
    for n=1:numpoints
      grid(m,n,1)=x(m);
      grid(m,n,2)=y(n);
      grid(m,n,3)=quadgk(@(p1)IeroXY(grid(m,n,1),...
         grid(m,n,2),z,p1,d,k0,a),0,a);
      grid(m,n,4)=quadgk(@(p1)IoneXY(grid(m,n,1),...
         grid(m,n,2),z,p1,d,k0,a),0,a);
      grid(m,n,5)=quadgk(@(p1)ItwoXY(grid(m,n,1),...
         grid(m,n,2),z,p1,d,k0,a),0,a);
      grid(m,n,6)=-1i*K*(grid(m,n,3)+grid(m,n,5)*cos(2*theta));
      grid(m,n,7)=-1i*K*grid(m,n,5)*sin(2*theta);
      grid(m,n,8)=-2*K*grid(m,n,4)*cos(theta);
    end
end
    I2x=conj(grid(:,:,6)).*(grid(:,:,6));
    I2y=conj(grid(:,:,7)).*(grid(:,:,7));
    I2z=conj(grid(:,:,8)).*(grid(:,:,8));
    I=scale*(I2x+I2y+I2z); % maximum intensity
    figure
    plot(X,Y,I);
 %%%%%I0,I1,I2 intergral%%%%%%%%%%%
function out1=IeroXY(x,y,z,p1,d,k0,a)
function out2=IoneXY(x,y,z,p1,d,k0,a)
function out3=IwoXY(x,y,z,p1,d,k0,a)
global n1 e21prime e22prime
    xi1prime=e21prime-n1^2*sin(p1).^2;
    xi2prime=e22prime;
```

```
    modulXi=sqrt(xi1prime.^2+xi2prime.^2);
    mt1prime=sqrt((modulXi+xi1prime+2*n1^2*(sin(p1)).^2)/2);
    mt2prime=sqrt((modulXi-xi1prime)/2);
    kt1prime=mt1prime*k0;
    kt2prime=mt2prime*k0;
    v=k0*n1*sqrt((x.^2+y.^2))*sin(a); % v
    u=kt1prime*z*sin(a)^2; % u
    p2=asin(n1*sin(p1)./mt1prime);
    abbr=-d*(n1*cos(p1)-mt1prime.*cos(p2));
    ts=2*sin(p2).*cos(p1)./sin(p1+p2);
    tp=2*sin(p2).*cos(p1)./(sin(p1+p2).*cos(p1-p2));
I0=besselj(2,v*sin(p1)/sin(a)).*sqrt(cos(p1)).*sin(p1)...
    *exp(1i*k0*abbr).*(ts-tp.*cos(p2)).*exp(1i*u.*cos(p2)/sin(a)^2)...
    *exp(-kt2prime*(z+d)).*kt1prime.^2;
I1=besselj(1,v*sin(p1)/sin(a)).*sqrt(cos(p1)).*sin(p1)...
    *exp(1i*k0*abbr).*tp.*sin(p2).*exp(1i*u.*cos(p2)/sin(a)^2)...
    *exp(-kt2prime*(z+d)).*kt1prime.^2;
I2==besselj(2,v*sin(p1)/sin(a)).*sqrt(cos(p1)).*sin(p1)...
    *exp(1i*k0*abbr).*(ts-tp.*cos(p2)).*exp(1i*u.*cos(p2)/sin(a)^2)...
    *exp(-kt2prime*(z+d)).*kt1prime.^2;
```

Bibliography

[1] A. R. Parker, R. C. McPhedran, D. R. McKenzie, L. C. Botten, and N.-A. P. Nicorovici, "Photonic engineering: Aphrodite's iridescence," *Nature*, vol. 409, pp. 36–37, 2001.

[2] A. W. Eckert, *The World of Opals.* John Wiley & Sons Ltd, 1997.

[3] S. Kinoshita and S. Yoshioka, "Structural colors in nature: The role of regularity and irregularity in the structure," *ChemPhysChem*, vol. 6, no. 8, pp. 1442–1459, 2005.

[4] B. Rondeau, E. Fritsch, F. Mazzero, J.-P. Gauthier, B. Cenki-Tok, E. Bekele, and E. Gaillou, "Play-of-color opal from wegel tena, wollo province, ethiopia.," *Gems Gemol.*, vol. 46, No 2, pp. 90–105, 2010.

[5] H. Fudouzi, "Tunable structural color in organisms and photonic materials for design of bioinspired materials," *Sci. Technol. Adv. Mater.*, vol. 12, no. 6, p. 064704, 2011.

[6] C. P. Royall, M. E. Leunissen, and A. van Blaaderen, "A new colloidal model system to study long-range interactions quantitatively in real space," *J. Phys.: Condens. Matter*, vol. 15, no. 48, pp. S3581–S3596, 2003.

[7] C. I. Aguirre, E. Reguera, and A. Stein, "Tunable colors in opals and inverse opal photonic crystals," *Adv. Funct. Mater.*, vol. 20, no. 16, pp. 2565–2578, 2010.

[8] C. Alberdi, S. Alfonso, J. M. Diñeiro, B. Hernández, and C. Sáenz, "Interface between transparent isotropic and uniaxial absorbing dielectric media: equations

for ray tracing and for the direction of propagation.," *J Opt Soc Am A Opt Image Sci Vis*, vol. 25, no. 10, pp. 2476–88, 2008.

[9] H. Ghiradella, "Light and color on the wing: structural colors in butterflies and moths," *Appl. Opt.*, vol. 30, no. 24, pp. 3492–3500, 1991.

[10] S. John, "Strong localization of photons in certain disordered dielectric superlattices," *Phys. Rev. Lett.*, vol. 58, pp. 2486–2489, 1987.

[11] E. Yablonovitch, "Inhibited spontaneous emission in solid-state physics and electronics," *Phys. Rev. Lett.*, vol. 58, pp. 2059–2062, 1987.

[12] L. Rayleigh, "On the remarkable phenomenon of crystalline reflexion described by prof. stokes," *Philos. Mag.*, vol. 26, no. 160, pp. 256–265, 1888.

[13] F. Bloch, "Über die quantenmechanik der elektronen in kristallgittern," *Zeitschrift für Physik*, vol. 52, no. 7-8, pp. 555–600, 1929.

[14] G. Floquet, "Sur les équations différentielles linéaires à coefficients périodiques," *Annales scientifiques de l'É.N.S*, vol. 2, pp. 47–88, 1883.

[15] S. G. Johnson and J. D. Joannopoulos, "Three-dimensionally periodic dielectric layered structure with omnidirectional photonic band gap," *Appl. Phys. Lett.*, vol. 77, no. 22, pp. 3490–3492, 2000.

[16] J. N. W. John D. Joannopoulos, Steven G. Johnson and R. D. Meade, *Photonic Crystals: Molding the Flow of Light (Second Edition).* Princeton University Press, Princeton, New Jersey 08540 USA, 2008.

[17] S. G. Johnson and J. D. Joannopoulos, "Photonic crystals: The road from theory to practice," 2002.

[18] K. Schmidt and R. Kappeler, "Efficient computation of photonic crystal waveguide modes with dispersive material," *Opt. Express*, vol. 18, no. 7, pp. 7307–7322, 2010.

[19] R. Watahiki, T. Shimada, P. Zhao, S. Chiashi, S. Iwamoto, Y. Arakawa, S. Maruyama, and Y. K. Kato, "Enhancement of carbon nanotube photoluminescence by photonic crystal nanocavities," *Appl. Phys. Lett.*, vol. 101, no. 14, pp. 141124–3, 2012.

[20] A. M. Cubillas, S. Unterkofler, T. G. Euser, B. J. M. Etzold, A. C. Jones, P. J. Sadler, P. Wasserscheid, and P. S. Russell, "Photonic crystal fibres for chemical sensing and photochemistry," *Chem. Soc. Rev.*, vol. 42, pp. 8629–8648, 2013.

[21] J. M. Dudley and J. R. Taylor, "Ten years of nonlinear optics in photonic crystal fibre," *Nat. Photon.*, vol. 3, no. 2, pp. 85–90, 2009.

[22] M. E. Fermann and I. Hartl, "Ultrafast fibre lasers," *Nat. Photon.*, vol. 7, no. 11, pp. 868–874, 2013.

[23] O. Painter, R. K. Lee, A. Scherer, A. Yariv, J. D. O'Brien, P. D. Dapkus, and I. Kim, "Two-dimensional photonic band-gap defect mode laser," *Science*, vol. 284, no. 5421, pp. 1819–1821, 1999.

[24] J. M. Raimond, M. Brune, and S. Haroche, "Manipulating quantum entanglement with atoms and photons in a cavity," *Rev. Mod. Phys.*, vol. 73, pp. 565–582, 2001.

[25] H. Mabuchi and A. C. Doherty, "Cavity quantum electrodynamics: Coherence in context," *Science*, vol. 298, no. 5597, pp. 1372–1377, 2002.

[26] T. Yoshie, A. Scherer, J. Hendrickson, G. Khitrova, H. M. Gibbs, G. Rupper, C. Ell, O. B. Shchekin, and D. G. Deppe, "Vacuum rabi splitting with a single quantum dot in a photonic crystal nanocavity," *Nature*, vol. 432, pp. 200–203, Nov. 2004.

[27] J. P. Reithmaier, G. Sek, A. Loffler, C. Hofmann, S. Kuhn, S. Reitzenstein, L. V. Keldysh, V. D. Kulakovskii, T. L. Reinecke, and A. Forchel, "Strong coupling in a single quantum dot-semiconductor microcavity system," *Nature*, vol. 432, no. 7014, pp. 197–200, 2004.

[28] A. Loffler, C. Hofmann, S. Reitzenstein, M. Kamp, J. P. Reithmaier, and A. Forchel, "Semiconductor quantum dot micropillar cavities for quantum electrodynamic experiments," in *Lasers and Electro-Optics Society, 2005. LEOS 2005. The 18th Annual Meeting of the IEEE*, pp. 545–546, Oct 2005.

[29] E. Peter, P. Senellart, D. Martrou, A. Lemaitre, J. Hours, J. Gerard, and J. Bloch, "Exciton-photon strong-coupling regime for a single quantum dot embedded in a microcavity," *Phys. Rev. Lett.*, vol. 95, p. 067401, 2005.

[30] A. Faraon, I. Fushman, D. Englund, N. Stoltz, P. Petroff, and J. Vuckovic, "Coherent generation of non-classical light on a chip via photon-induced tunnelling and blockade," *Nat. Phys.*, vol. 4, no. 11, pp. 859–863, 2008.

[31] W. Ahn, S. V. Boriskina, Y. Hong, and B. M. Reinhard, "Photonic-plasmonic mode coupling in on-chip integrated optoplasmonic molecules," *ACS Nano*, vol. 6, no. 1, pp. 951–960, 2012. PMID: 22148502.

[32] R. Ameling and H. Giessen, "Microcavity plasmonics: strong coupling of photonic cavities and plasmons," *Laser & Photon. Rev*, vol. 7, no. 2, pp. 141–169, 2013.

[33] A. Faraon, C. Santori, Z. Huang, K.-M. C. Fu, V. M. Acosta, D. Fattal, and R. G. Beausoleil, "Quantum photonic devices in single-crystal diamond," *New J. Phys.*, vol. 15, no. 2, p. 025010, 2013.

[34] F. Albert, K. Sivalertporn, J. Kasprzak, M. Strauß, C. Schneider, S. Höfling, M. Kamp, A. Forchel, S. Reitzenstein, E. Muljarov, and W. Langbein, "Microcavity controlled coupling of excitonic qubits," *Nat Commun*, vol. 4, pp. 1747–, 2013.

[35] J. Kasprzak, S. Reitzenstein, E. A. Muljarov, C. Kistner, C. Schneider, M. Strauss, S. Hofling, A. Forchel, and W. Langbein, "Up on the jaynes-cummings ladder of a quantum-dot/microcavity system," *Nat Mater*, vol. 9, no. 4, pp. 304–308, 2010.

[36] M. Barth, S. Schietinger, S. Fischer, J. Becker, N. Nuisse, T. Aichele, B. Loichel, C. Soinnichsen, and O. Benson, "Nanoassembled plasmonic-photonic hybrid

cavity for tailored light-matter coupling," *Nano Letters*, vol. 10, no. 3, pp. 891–895, 2010. PMID: 20141157.

[37] AtesS., U. M., UlhaqA., ReitzensteinS., LofflerA., HoflingS., ForchelA., and MichlerP., "Non-resonant dot-cavity coupling and its potential for resonant single-quantum-dot spectroscopy," *Nat Photon*, vol. 3, no. 12, pp. 724–728, 2009.

[38] L. C. Bassett, F. J. Heremans, D. J. Christle, C. G. Yale, G. Burkard, B. B. Buckley, and D. D. Awschalom, "Ultrafast optical control of orbital and spin dynamics in a solid-state defect," *Science*, vol. 345, no. 6202, pp. 1333–1337, 2014.

[39] Y. Dumeige, M. Chipaux, V. Jacques, F. Treussart, J.-F. Roch, T. Debuisschert, V. M. Acosta, A. Jarmola, K. Jensen, P. Kehayias, and D. Budker, "Magnetometry with nitrogen-vacancy ensembles in diamond based on infrared absorption in a doubly resonant optical cavity," *Phys. Rev. B, PRB*, vol. 87, no. 15, 2013.

[40] J. Orwa, A. Greentree, I. Aharonovich, A. Alves, J. V. Donkelaar, A. Stacey, and S. Prawer, "Fabrication of single optical centres in diamond: a review," *J. Lumin.*, vol. 130, no. 9, pp. 1646 –1654, 2010. Special Issue based on the Proceedings of the Tenth International Meeting on Hole Burning, Single Molecule, and Related Spectroscopies: Science and Applications (HBSM 2009) - Issue dedicated to Ivan Lorgere and Oliver Guillot-Noel.

[41] M. Maldovan and E. L. Thomas, "Diamond-structured photonic crystals," *Nat Mater.*, vol. 3, no. 9, pp. 593–600, 2004.

[42] Y. Chen, *Fabrication and characterization of three dimensional photonic crystals generated by multibeam Interfence lithography.* PhD thesis, National Tsing Hua University, 2002.

[43] D. Shir, E. C. Nelson, Y. C. Chen, A. Brzezinski, H. Liao, P. V. Braun, P. Wiltzius, K. H. A. Bogart, and J. A. Rogers, "Three dimensional silicon photonic crystals fabricated by two photon phase mask lithography," *Appl. Phys. Lett.*, vol. 94, no. 1, pp. 011101–3, 2009.

[44] S. Y. Lin, J. G. Fleming, D. L. Hetherington, B. K. Smith, R. Biswas, K. M. Ho, M. M. Sigalas, W. Zubrzycki, S. R. Kurtz, and J. Bur, "A three-dimensional photonic crystal operating at infrared wavelengths," *Nature*, vol. 394, no. 6690, pp. 251–253, 1998.

[45] S. Noda, K. Tomoda, N. Yamamoto, and A. Chutinan, "Full three-dimensional photonic bandgap crystals at near-infrared wavelengths," *Science*, vol. 289, no. 5479, pp. 604–606, 2000.

[46] G. I. Waterhouse and M. R. Waterland, "Opal and inverse opal photonic crystals: Fabrication and characterization," *Polyhedron*, vol. 26, no. 2, pp. 356 –368, 2007. Modern Inorganic Chemistry in Australia and New Zealand.

[47] J. Zhang, Y. Li, X. Zhang, and B. Yang, "Colloidal self-assembly meets nanofabrication: From two-dimensional colloidal crystals to nanostructure arrays," *Adv. Mater.*, vol. 22, no. 38, pp. 4249–4269, 2010.

[48] M. Campbell, D. N. Sharp, M. T. Harrison, R. G. Denning, and A. J. Turberfield, "Fabrication of photonic crystals for the visible spectrum by holographic lithography," *Nature*, vol. 404, no. 6773, pp. 53–56, 2000.

[49] T. Nguyen, Q. Nguyen, J. Zyss, I. Ledoux-Rak, and N. Lai, "Optimization of thickness and uniformity of photonic structures fabricated by interference lithography," *Appl Phys A*, vol. 111, no. 1, pp. 297–302, 2013.

[50] N. D. Lai, W. Liang, J. Lin, and C. Hsu, "Rapid fabrication of large-area periodic structures containing well-defined defects by combining holography and mask techniques," *Opt. Express*, vol. 13, no. 14, pp. 5331–5337, 2005.

[51] K. K. Seet, V. Mizeikis, S. Juodkazis, and H. Misawa, "Three-dimensional horizontal circular spiral photonic crystals with stop gaps below 1 μm," *Appl. Phys. Lett.*, vol. 88, no. 22, pp. 221101–3, 2006.

[52] M. Vaezi, H. Seitz, and S. Yang, "A review on 3d micro-additive manufacturing technologies," *Int J Adv Manuf Technol*, vol. 67, no. 5-8, pp. 1957–1957, 2013.

[53] P. Debye, "Das verhalten von lichtwellen in der nähe eines brennpunktes oder einer brennlinie," *Ann. Phys. (Berlin)*, vol. 335, no. 14, pp. 755–776, 1909.

[54] E. Wolf, "Electromagnetic diffraction in optical systems. i. an integral representation of the image field," *Proc. R. Soc. A*, vol. 253, no. 1274, pp. 349–357, 1959.

[55] M. Herzberger and R. v. Mises, "Review: R. k. luneberg, mathematical theory of optics," *Bull. Amer. Math. Soc.*, vol. 51, no. 11, pp. 865–867, 1945.

[56] J. Gasper, G. C. Sherman, and J. J. Stamnes, "Reflection and refraction of an arbitrary electromagnetic wave at a plane interface," *J. Opt. Soc. Am.*, vol. 66, no. 9, pp. 955–961, 1976.

[57] J. J. Stamnes and G. C. Sherman, "Radiation of electromagnetic fields in uniaxially anisotropic media," *J. Opt. Soc. Am.*, vol. 66, no. 8, pp. 780–788, 1976.

[58] E. Wolf and Y. Li, "Conditions for the validity of the debye integral representation of focused fields," *Opt Commun*, vol. 39, no. 4, pp. 205 –210, 1981.

[59] H. Ling and S.-W. Lee, "Focusing of electromagnetic waves through a dielectric interface," *J. Opt. Soc. Am. A*, vol. 1, no. 9, pp. 965–973, 1984.

[60] Y. Ji and K. Hongo, "Analysis of electromagnetic waves refracted by a spherical dielectric interface," *J. Opt. Soc. Am. A*, vol. 8, no. 3, pp. 541–548, 1991.

[61] R. KanT, "An analical solusion of vector diffraction for focufocus optical-system with seidel abberation. 1. spherical-abberation, curvature of field, and distorsion," *J. Mod. Opt.*, vol. 40, no. 11, pp. 2293–2310, 1993.

[62] J. J. Stamnes and G. S. Sithambaranathan, "Reflection and refraction of an arbitrary electromagnetic wave at a plane interface separating an isotropic and a biaxial medium," *J. Opt. Soc. Am. A*, vol. 18, no. 12, pp. 3119–3129, 2001.

[63] J. Stamnes, *Waves in Focal Regions: Propagation, Diffraction and Focusing of Light, Sound and Water Waves.* Adam Hilger, Bristol, UK, 1986.

[64] S. Hell, G. Reiner, C. Cremer, and E. H. K. Stelzer, "Aberrations in confocal fluorescence microscopy induced by mismatches in refractive index," *J. Microsc.*, vol. 169, no. 3, pp. 391–405, 1993.

[65] P. Török, P. Varga, Z. Laczik, and G. Booker, "Electromagnetic diffraction of light focused through a planar interface between materials of mismatched refractive indices: an integral representation," *JOSA A*, vol. 12, no. 2, pp. 325–332, 1995.

[66] S. H. Wiersma and T. D. Visser, "Defocusing of a converging electromagnetic wave by a plane dielectric interface," *J. Opt. Soc. Am. A*, vol. 13, no. 2, pp. 320–325, 1996.

[67] M. Leutenegger, R. Rao, R. A. Leitgeb, and T. Lasser, "Fast focus field calculations," *Opt. Express*, vol. 14, no. 23, pp. 11277–11291, 2006.

[68] J. Lin, O. G. Rodríguez-Herrera, F. Kenny, D. Lara, and J. C. Dainty, "Fast vectorial calculation of the volumetric focused field distribution by using a three-dimensional fourier transform," *Opt. Express*, vol. 20, no. 2, pp. 1060–1069, 2012.

[69] S. Chang, J. H. Jo, and S. S. Lee, "Theoretical calculations of optical force exerted on a dielectric sphere in the evanescent field generated with a totally-reflected focused gaussian beam," *Opt Commun*, vol. 108, no. 1-3, pp. 133–143, 1994.

[70] D. Censor, "Fermat's principle and real space-time rays in absorbing media," *J. Phys. A*, vol. 10, no. 10, pp. 1781–1790, 1977.

[71] S. J. Chapman, J. M. H. Lawry, J. R. Ockendon, and R. H. Tew, "On the theory of complex rays," *SIAM Review*, vol. 41, no. 3, pp. 417–509, 1999.

[72] R. Egorchenkov and Y. Kravtsov, "Complex ray-tracing algorithms with application to optical problems," *JOSA A*, vol. 18, no. 3, pp. 650–656, 2001.

[73] P. C. Chang, J. Walker, and K. Hopcraft, "Ray tracing in absorbing media," *J. Quant. Spectrosc. Radiat. Transfer*, vol. 96, no. 3-4, pp. 327–341, 2005.

[74] J. M. Diñeiro, M. Berrogui, S. Alfonso, C. Alberdi, B. Hernández, and C. Sáenz, "Complex unitary vectors for the direction of propagation and for the polarization of electromagnetic waves in uniaxial and absorbing dielectric media.," *J Opt Soc Am A Opt Image Sci Vis*, vol. 24, no. 6, pp. 1767–75, 2007.

[75] L. G. Guimarães and E. E. Sampaio, "A note on snell laws for electromagnetic plane waves in lossy media," *J. Quant. Spectrosc. Radiat. Transfer*, vol. 109, no. 11, pp. 2124–2140, 2008.

[76] Y. Wang, P. Shi, H. Xin, and L. Wu, "Complex ray tracing in biaxial anisotropic absorbing media," *J. Opt. Soc. Am. A*, vol. 10, no. 7, p. 075009, 2008.

[77] Y. Wang, L. Liang, H. Xin, and L. Wu, "Complex ray tracing in uniaxial absorbing media," *J. Opt. Soc. Am. A*, vol. 25, no. 3, pp. 653–7, 2008b.

[78] S. Alfonso, J. M. D. neiro, C. Alberdi, B. Hernández, and C. Sáenz, "Influence of absorption on the anomalous negative refraction in right-handed uniaxial absorbing dielectric media," *J. Opt. Soc. Am. A*, vol. 27, no. 9, pp. 1938–1945, 2010.

[79] M. Sluijter, *Ray-optics analysis of inhomogeneous optically anisotropic media.* Dissertation, TNW Optics Research Group, Delft University of Technology, January 2010.

[80] B. Davis, P. Carney, and R. Bhargava, "Theory of midinfrared absorption microspectroscopy: I. homogeneous samples," *Anal. Chem.*, vol. 82, no. 9, pp. 3474–3486, 2010.

[81] J. M. Diñeiro, C. Alberdi, B. Hernández, and C. Sáenz, "Uniaxial absorbing media: conditions for refraction in the direction of the optical axis.," *J Opt Soc Am A Opt Image Sci Vis*, vol. 30, no. 3, pp. 385–91, 2013.

[82] L. G. Guimarães and E. E. Sampaio, "Debye analysis applied to multiple reflections and attenuation of electromagnetic plane waves in a stratified sea substratum," *J. Quant. Spectrosc. Radiat. Transfer*, vol. 109, no. 5, pp. 811–821, 2008.

[83] I. Besieris, “Comment on the “corrected fresnel coefficients for lossy materials",” *IEEE Antennas Propag. Mag.*, vol. 53, no. 4, pp. 1–4, 2011.

[84] F. X. Canning, “Corrected fresnel coefficients for lossy materials,” in *APSURSI*, pp. 2123–2126, APSURSI, IEEE, July 2011.

[85] M. Dupertuis, M. Proctor, and B. Acklin, “Generalization of complex snell-descartes and fresnel laws,” *JOSA A*, vol. 11, no. 3, 1994.

[86] H. Weber, “The fresnel equations for lossy dielectrics and conservation of energy,” *J. Mod. Opt.*, vol. 61, no. 15, pp. 1219–1224, 2014.

[87] V. Y. Fedorov and T. Nakajima, “Negative refraction of inhomogeneous waves in lossy isotropic media,” *J. Opt.*, vol. 16, no. 3, p. 035103, 2014.

[88] R. K. Luneburg, *Mathematical theory of optics.* University of California Press, Berkeley, Calif., 1966.

[89] P. Török, P. Varga, A. Konkol, and G. R. Booker, “Electromagnetic diffraction of light focused through a planar interface between materialsof mismatched refractive indices: structure of the electromagnetic field. ii,” *J. Opt. Soc. Am. A*, vol. 13, no. 11, pp. 2232–2238, 1996.

[90] D. Schroder, *Semiconductor Material and Device Characterization, 3rd Edition.* No. 978-0-471-73906-7, Wiley-IEEE Press, 2006.

[91] E. L. Dereniak and T. D. Dereniak, *Geometrical and Trigonometric Optics.* Cambridge University Press, 2008.

[92] C. HSU, J. Lin, T. Chang, H. Lin, T. Chou, and J. Tsai, “Circular photonic crystal structure, light emitting diode device and photoelectric conversion device,” oct 2012. US Patent App. 13/150,275.

[93] W. Denk, J. Strickler, and W. Webb, “Two-photon laser scanning fluorescence microscopy,” *Science*, vol. 248, no. 4951, pp. 73–76, 1990.

[94] M. Farsari and B. N. Chichkov, “Materials processing: Two-photon fabrication,” *Nat. Photon.*, vol. 3, no. 8, pp. 450–452, 2009.

[95] G. Lemercier, J.-C. Mulatier, C. Martineau, R. Anémian, C. Andraud, I. Wang, O. Stéphan, N. Amari, and P. Baldeck, "Two-photon absorption: from optical power limiting to 3d microfabrication," *C.R. Acad. Sci., Ser. IIb: Mec., Phys., Chim., Astron.*, vol. 8, no. 8, pp. 1308–1316, 2005. Matériaux moléculaires Molecular materials.

[96] S. Wu, J. Serbin, and M. Gu, "Two-photon polymerisation for three-dimensional micro-fabrication," *J. Photochem. Photobiol., A*, vol. 181, no. 1, pp. 1–11, 2006.

[97] L. Li and J. T. Fourkas, "Multiphoton polymerization," *Mater. Today*, vol. 10, no. 6, pp. 30 –37, 2007.

[98] K.-S. Lee, R. H. Kim, D.-Y. Yang, and S. H. Park, "Advances in 3d nano/microfabrication using two-photon initiated polymerization," *Prog. Polym. Sci.*, vol. 33, no. 6, pp. 631 – 681, 2008.

[99] T. T. N. Nguyen, M. H. Luong, M. T. Do, D. M. Kieu, Q. Li, D. T. T. Nguyen, Q. C. Tong, I. Ledoux-Rak, and N. D. Lai, "Micro and nanostructuration of polymer materials and applications," *Proc. SPIE*, vol. 9171, pp. 91710O–91710O–7, 2014.

[100] M. Deubel, M. Wegener, S. Linden, G. von Freymann, and S. John, "3d-2d-3d photonic crystal heterostructures fabricated by direct laser writing," *Opt. Lett.*, vol. 31, no. 6, pp. 805–807, 2006.

[101] G. von Freymann, A. Ledermann, M. Thiel, I. Staude, S. Essig, K. Busch, and M. Wegener, "Three-dimensional nanostructures for photonics," *Adv. Funct. Mater.*, vol. 20, no. 7, pp. 1038–1052, 2010.

[102] M. Thiel, G. von Freymann, and M. Wegener, "Layer-by-layer three-dimensional chiral photonic crystals," *Opt. Lett.*, vol. 32, no. 17, pp. 2547–2549, 2007.

[103] T. F. Scott, C. J. Kloxin, D. L. Forman, R. R. McLeod, and C. N. Bowman, "Principles of voxel refinement in optical direct write lithography," *J. Mater. Chem.*, vol. 21, pp. 14150–14155, 2011.

[104] K.-S. Chen, I.-K. Lin, and F.-H. Ko, "Fabrication of 3d polymer microstructures using electron beam lithography and nanoimprinting technologies," *J. Micromech. Microeng.*, vol. 15, no. 10, p. 1894, 2005.

[105] B. Di Bartolo and O. Forte, eds., *Advances in Spectroscopy for Lasers and Sensing*, vol. 231 of *Nato Science Series II*, (Erice, Sicily, Italy), Proceedings of the NATO Advanced Study Institute on New Developments in Optics and Related Fields, SpringerLink, june 2005.

[106] D. S. Correa, L. D. Boni, A. J. G. Otuka, V. Tribuzi, and C. R. Mendonça, "Two-photon polymerization fabrication of doped microstructures," pp. 445–447, 2012.

[107] X. Yin, N. Fang, X. Zhang, I. B. Martini, and B. J. Schwartz, "Near-field two-photon nanolithography using an apertureless optical probe," *Appl. Phys. Lett.*, vol. 81, no. 19, pp. 3663–3665, 2002.

[108] L. Li, R. R. Gattass, E. Gershgoren, H. Hwang, and J. T. Fourkas, "Achieving $\lambda/20$ resolution by one-color initiation and deactivation of polymerization," *Science*, vol. 324, no. 5929, pp. 910–913, 2009.

[109] B. Kramer, ed., *Advances in Solid State Physics, Vol. 44*. No. 1438-4329, Springer Berlin Heidelberg, 2004, XX, 566 p.

[110] M. T. Do, T. T. N. Nguyen, Q. Li, H. Benisty, I. Ledoux-Rak, and N. D. Lai, "Submicrometer 3d structures fabrication enabled by one-photon absorption direct laser writing," *Opt. Express*, vol. 21, no. 18, pp. 20964–20973, 2013.

[111] C. J. Niu, W. D. Foltz, M. Velec, J. L. Moseley, A. Al-Mayah, and K. K. Brock, "A novel technique to enable experimental validation of deformable dose accumulation," *Med. Phys.*, vol. 39, no. 2, pp. 765–776, 2011.

[112] M. T. Do, Q. Li, I. Ledoux-Rak, and N. D. Lai, "Optimization of lopa-based direct laser writing technique for fabrication of submicrometric polymer two- and three-dimensional structures," 2014.

[113] J. A. Matta and J. O. Outwater, "The nature, origin and effects of internal stresses in reinforced plastic laminates," *Polymer. Eng. Science.*, vol. 2, no. 4, pp. 314–319, 1962.

[114] I. Friedler, C. Sauvan, J. P. Hugonin, P. Lalanne, J. Claudon, and J. M. Gérard, "Solid-state single photon sources: the nanowire antenna," *Opt. Express*, vol. 17, no. 4, pp. 2095–2110, 2009.

[115] M. Barth, S. Schietinger, T. Schroder, T. Aichele, and O. Benson, "Controlled coupling of {NV} defect centers to plasmonic and photonic nanostructures," *J. Lumin.*, vol. 130, no. 9, pp. 1628 – 1634, 2010. Special Issue based on the Proceedings of the Tenth International Meeting on Hole Burning, Single Molecule, and Related Spectroscopies: Science and Applications (HBSM 2009) - Issue dedicated to Ivan Lorgere and Oliver Guillot-Noel.

[116] S. Merabia, S. Shenogin, L. Joly, P. Keblinski, and J.-L. Barrat, "Heat transfer from nanoparticles: A corresponding state analysis," *Proc. Natl. Acad. Sci. U.S.A.*, vol. 106, no. 36, pp. 15113–15118, 2009.

[117] S. Hashimoto, D. Werner, and T. Uwada, "Studies on the interaction of pulsed lasers with plasmonic gold nanoparticles toward light manipulation, heat management, and nanofabrication," *J. Photochem. Photobiol.*, vol. 13, no. 1, pp. 28 – 54, 2012.

[118] C. Mack, *Fundamental Principles of Optical Lithography.* No. 978-0-470-01893-4, John Wiley & Sons Ltd, 2008.

[119] W. Lukosz and R. E. Kunz, "Light emission by magnetic and electric dipoles close to a plane interface. i. total radiated power," *J. Opt. Soc. Am.*, vol. 67, no. 12, pp. 1607–1615, 1977.

[120] E. Fort and S. Grésillon, "Surface enhanced fluorescence," *J. Phys. D: Appl. Phys.*, vol. 41, no. 1, p. 013001, 2008.

[121] J. P. Wilcoxon, J. E. Martin, F. Parsapour, B. Wiedenman, and D. F. Kelley,

"Photoluminescence from nanosize gold clusters," *J. Chem. Phys.*, vol. 108, no. 21, pp. 9137–9143, 1998.

[122] T. Zhang, G. Lu, H. Shen, K. Shi, Y. Jiang, D. Xu, and Q. Gong, "Photoluminescence of a single complex plasmonic nanoparticle," *Sci. Rep.*, vol. 4, 2014.

[123] C.-Y. Chao and L. J. Guo, "Thermal-flow technique for reducing surface roughness and controlling gap size in polymer microring resonators," *Appl. Phys. Lett.*, vol. 84, no. 14, pp. 2479–2481, 2004.

[124] B. Bêche, A. Potel, J. Barbe, V. Vié, J. Zyss, C. Godet, N. Huby, D. Pluchon, and E. Gaviot, "Resonant coupling into hybrid 3d micro-resonator devices on organic/biomolecular film/glass photonic structures," *Opt Commun*, vol. 283, no. 1, pp. 164 – 168, 2010.

[125] D. Pluchon, N. Huby, L. Frein, A. Moréac, P. Panizza, and B. Bêche, "Flexible beam-waist technique for whispering gallery modes excitation in polymeric 3d micro-resonators," *Optik*, vol. 124, no. 15, pp. 2085 –2088, 2013.

[126] J. Chen, W. He, W. Wang, Z. Tao, and G. Xie, "Effects of losses on energy flow propagation direction of transmitted waves at a lossy interface," *J. Mod. Opt.*, vol. 60, no. 6, pp. 488–495, 2013.

[127] F. V. Ignaovich and V. K. Ignatovich, "Optics of anisotropic media," *Physics-Uspekhi*, vol. 55, no. 7, pp. 709–720, 2012.

[128] J. A. Stratton and L. J. Chu, "Diffraction theory of electromagnetic waves," *Phys. Rev.*, vol. 56, pp. 99–107, 1939.

[129] B. Richards and E. Wolf, "Electromagnetic diffraction in optical systems. ii. structure of the image field in an aplanatic system," *Proc. R. Soc. A*, vol. 253, no. 1274, pp. 358–379, 1959.